VYSOKÉ UČENÍ TECHNICKÉ V BRNĚ
BRNO UNIVERSITY OF TECHNOLOGY

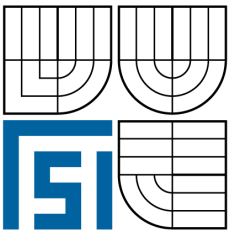

FAKULTA STROJNÍHO INŽENÝRSTVÍ
ÚSTAV FYZIKÁLNÍHO INŽENÝRSTVÍ
FACULTY OF MECHANICAL ENGINEERING
INSTITUTE OF PHYSICAL ENGINEERING

APLIKACE PLAZMONOVÝCH POLARITONŮ V NANOFOTONICE

APPLICATION OF PLASMON POLARITONS IN NANOPHOTONICS

DIZERTAČNÍ PRÁCE
DOCTORAL THESIS

AUTOR PRÁCE
AUTHOR
ING. LUKÁŠ BŘÍNEK

VEDOUCÍ PRÁCE
SUPERVISOR
Prof. RNDr. PETR DUB, CSc.

BRNO 2015

Abstrakt
Práce pojednává o vlastnostech plazmonických antén v infračervené a viditelné oblasti. Práce zahrnuje výrobu, měření a numerické modelování optických vlastností antén. Infračervené plazmonické antény na absorbujícím substrátu (SRON) jsou studovány pro jejich rezonanční a absorpční vlastnosti. Byla nalezena geometrie antény, která poskytuje maximální účinnost absorpce ve SRON vrstvě. Dále je studována možnost zesílení daného vibračního módu substrátu (obsahujícího 3-4 materiálové rezonance) pomocí plazmonické rezonance antény. Nakonec jsou prezentována měření katodoluminiscenčních spekter antén ve viditelném spektru.

Summary
The work deals with plasmonic antennas for infrared and visible wavelengths. This work involves fabrication, measurements and numerical modelling of optical properties of these structures. First, infrared plasmonic antennas deposited on the SRON layer with a significant absorption are studied both for their resonant and absorption properties. The antenna geometry providing maximal enhancement of the absorption efficiency in the SRON layer is found. Subsequently, the ability of a plasmonic antenna resonance to enhance a given vibrational mode of its substrate (called SEIRS) possessing 3-4 material resonances is studied and confirmed on antennas on SRON. In the end, the measured cathodoluminescence spectra of visible antennas are presented to show different types of antenna excitation.

Klíčová slova
Plazmonické rezonanční antény, plazmonika, lokalizované plazmonové polaritony, SEIRS, FDTD simulace.

Keywords
Plasmonic resonant antennas, plasmonics, localized plasmon polaritons, SEIRS, FDTD simulations.

BŘíNEK, L.:*Aplikace plazmonových polaritonů v nanofotonice*. Brno: Vysoké učení technické v Brně, Fakulta strojnÍho inženýrstvÍ, 2015. 75 s. Dizertační práce. Vedoucí práce Prof. RNDr. Petr Dub, CSc.

Poděkování

Děkuji vedoucímu své práce Prof. RNDr. Petru Dubovi, CSc. a Prof. RNDr. Tomáši Šikolovi, CSc. za konzultace a připomínky během práce. Dále děkuji Doc. Ing. Radku Kalouskovi, PhD., Ing. Petru Dvořákovi, Ing. Zoltánu Édesi, Ing. Tomáši Neumanovi, Doc. Ing. Jakubu Zlámalovi, PhD., Ing. Ondřejovi Tomancovi a Ing. Tomáši Matlochovi za cenné připomínky během diskusí. Především děkuji své rodině za podporu během studia a v životě.

Contents

1. Introduction

Nowadays, we are witnessing a rapid development of the information technology that puts ever-increasing demands on the information transfer and its processing. The signal processing is commonly carried out by technologies related to the electron transport that slowly reach their physical limits. Therefore, new technologies allowing faster signal processing are in focus of the scientific community.

Contrary to electrons, photons having no charge disregard electric and magnetic fields; moreover, their matter-interactions have been extensively studied and are well-known. For this reason, technologies exploiting photons may represent a useful supplement to the modern communication technology. One of perspective branches of optics is plasmonics that deals with the interaction between the electromagnetic field and electrons in metals at a metal-dielectric interface. The solution of the electromagnetic field at the conductive surface in the form of surface-waves was firstly found by Zenneck [1] and Sommerfeld [2].

The solutions of the Maxwell equations at the metal-dielectric interface are of the form of electromagnetic surface waves coupled to longitudinal collective oscillations of free-electron gas in a metal at metal-dielectric interfaces [3], [4], [5], [6], [7]. These surface waves propagate in the direction of the interface while the field exponentially decreases in the direction normal to the surface. The corresponding quasiparticles are called surface plasmon polaritons (SPPs) [5].

The existence of surface plasmon polaritons was firstly observed in a diffraction experiment on a metallic grating by R. W. Wood [8]. Later, a decrease in energy of electrons passing through thin metal foils in transmission electron microscopy was observed in 1950s [9], [10]. As the dispersion relation of SPPs exists below the light line in the given medium, the electromagnetic field is tied to the space smaller than the Rayleigh diffraction condition states [1]. For the same reason, SPPs cannot be excited or observed via the conventional way in the far-field unless the interface possesses some inhomogeneities. Consequently, experiments with the optical excitation of SPPs were performed by E. Kretschmann [11] and A. Otto [12] whose principles are commonly used till now. Even though the first studies of surface plasmon polaritons had been done at the beginning of the 20th century, fabrication of real plasmonic structures [13] started about 20 years ago when research in the field of nanotechnology expanded [14], [15].

The two-dimensional nature of SPPs promises the engineering of plasmonic optical-circuits still partially missing in optical communication systems, nano/photonic and optoelectronic devices in high-speed low-power telecommunications industry [13], [16], [17], [18], [19]. Moreover, the response of plasmonic structures exhibits a high sensitivity to presence of materials in their vicinity. This behaviour may be exploited in sensing methods [20], [21], [22].

Surface plasmon polaritons may not only propagate along the surface but also they can be tied to metallic objects of subwavelength dimensions which implies the crucial enhancement of the electromagnetic field. Such a structure represents an insula-

[1] Thus, plasmonics enables the optics beyond the diffraction limit and a light-concentration in the space considerably tinier than the Rayleigh criterion.

tor/metal/insulator truncated waveguide [3], [6] that converts free-propagating optical radiation to a localized energy and vice versa [23]. These structures are usually called resonant plasmonic antennas/structures. Plasmon polaritons resonating at these metallic structures are called Localized Plasmon Polaritons (LPPs).

Numbers of reviews have been published on plasmonic antennas in last four years [23], [24], [25], [26], [27]. Plasmonic antennas are utilized both for their scattering and absorption properties in the far-field or for high intensities in the near-field [18] at the resonance. Consequently, these structures are essential for many sensing applications [28] such as a high-resolution single-molecular microscopy and spectroscopy [29], surface-enhanced Raman spectroscopy [30], tip-enhanced Raman spectroscopy [31] and biosensing [21]. Moreover, a strong enhancement of the electromagnetic field via plasmonic resonances may be used in the photovoltaics [32], [33], [34], the enhanced photoluminescence [35], [36] and for trapping [37], [38], [39]. Last but not least, there are absorption-related applications [32] where a temperature enhancement occurs both in antennas and their surroundings [40], [41], [42]. This topic is studied also in this work (see Section 3.3). Temperature increase at resonance found a possible application also in a cancer-treatment in the medicine [22], [43]. To summarize, a majority of plasmonics applications is related to resonant structures.

Plasmonic antennas represent the main topic of the presented work. The work involves both theoretical and experimental study of these structures. The electromagnetic field of antennas and its near- and far-field properties have been modelled via numerical simulations. These simulations were then exploited to propose a geometry of antennas having the given resonant properties. Afterwards, antennas (of geometry) proposed by simulations were fabricated. Subsequently, the optical properties of fabricated antennas have been measured and compared with the simulated ones.

The physical background is described in Chapter 2 where the basics of the electromagnetic field and its interaction with matter are discussed. Electromagnetic field simulations providing worthwhile information about properties of plasmonic antennas are described in Sections 2.5 and 3.3. Then, antenna fabrication technologies as the Electron Beam Lithography (EBL) and the Focused Ion Beam (FIB) are presented in Sections 3.1.1 and 3.1.2, respectively. Nowadays, the development of plasmonics is focused on sensing applications; therefore, the resonance properties of antennas in the vicinity of a material possessing vibrational modes and thus having pronounced dispersion of its refractive index are studied in this work. First, a numerical study of absorption properties of this antenna-substrate system is done in Section 3.3. Subsequently, measured reflection spectra of IR antennas fabricated by EBL (Section 3.1.1) on not-annealed and annealed silicon-rich oxinitride (SRON) substrate are compared in Sections 3.3 and 3.4, respectively. Moreover, these antennas exhibit an ability to enhance the vibrational modes from the substrate discussed in Sections 3.4 and 3.4.1. In the end, to show a non-volumetric type of the antenna excitation, measured cathodoluminescence spectra of optical plasmonic antennas fabricated by FIB are presented in Section 3.5.

2. Fundamentals

This chapter provides a basic physical background of the interaction of the electromagnetic field with plasmonic structures. In particular, it is focused on the Maxwell equations (Section 2.1) with emphasis on surface plasmon polaritons (Section 2.2) and on basic models of optical properties of a matter (Section 2.4).

The first quantitative approach in the field of the electricity was published in 1785 by Ch. A. Coulomb. Time-varying currents and magnetic fields were studied by M. Faraday and his article about the electromagnetic induction was published in 1831. The previous knowledge was summarized and supplemented by J. C. Maxwell [44], [45] in 1865 and 1873. Afterwards, H. R. Hertz published his work [46] on transverse electromagnetic waves propagating with the speed of light in 1894. Thus, the equations that govern the light propagation have been found.

2.1 Maxwell equations

The Maxwell equations [47], [48], [49] are two scalar and two vector linear partial differential equations which together with the Lorentz force $\mathbf{F} = q(\mathbf{E} + \mathbf{v} \times \mathbf{B})$ represent a basis of the classical electrodynamics. In particular, the equations are

- the Gauss law for the electric field

$$\nabla \cdot \mathbf{E} = \frac{\varrho}{\varepsilon_0} \ , \tag{2.1}$$

- the Gauss law for the magnetic induction

$$\nabla \cdot \mathbf{B} = 0 \ , \tag{2.2}$$

- the Faraday law

$$\nabla \times \mathbf{E} = -\frac{\partial \mathbf{B}}{\partial t} \ , \tag{2.3}$$

- the Ampere-Maxwell law

$$\nabla \times \mathbf{B} = \mu_0 \mathbf{j} + \mu_0 \varepsilon_0 \frac{\partial \mathbf{E}}{\partial t} \ , \tag{2.4}$$

where ε_0 and μ_0 are the permittivity and permeability of vacuum, ϱ is the density of the electric charge and $\mathbf{j}$ is the current density. Consequently, the continuity equation $\nabla \cdot \mathbf{j} = -\frac{\partial \varrho}{\partial t}$ is found by performing the divergence of the Ampere-Maxwell law.

2.1.1 Maxwell equations in matter

In matter, the Maxwell equations become a modified form [47], [48]. In particular, a bound charge density ϱ_b is related to an electric polarization $\mathbf{P}$ via

$$\varrho_\mathrm{b} = -\nabla \cdot \mathbf{P} \tag{2.5}$$

and a bound current $\mathbf{j}_\mathrm{b}$ is related to a magnetisation $\mathbf{M}$ via

$$\mathbf{j}_\mathrm{b} = \nabla \times \mathbf{M} \ . \tag{2.6}$$

Additionally, the polarization current $\mathbf{j}_\mathrm{p}$ is related to the polarization $\mathbf{P}$ by the equation

$$\mathbf{j}_\mathrm{p} = \frac{\partial \mathbf{P}}{\partial t} \ . \tag{2.7}$$

Summarising, the total charge density ϱ consists of free and bound charge,

$$\varrho = \varrho_\mathrm{f} + \varrho_\mathrm{b} = \varrho_\mathrm{f} - \nabla \cdot \mathbf{P} \ . \tag{2.8}$$

The total current density $\mathbf{j}$ can be separated into free, bound and polarization currents [48],

$$\mathbf{j} = \mathbf{j}_\mathrm{f} + \mathbf{j}_\mathrm{b} + \mathbf{j}_\mathrm{p} = \mathbf{j}_\mathrm{f} + \nabla \times \mathbf{M} + \frac{\partial \mathbf{P}}{\partial t} \ . \tag{2.9}$$

Therefore, the Maxwell equations in matter obtain a different form when Equations 2.7, 2.8 and 2.9 are considered. In particular, the Gauss law modifies to

$$\nabla \cdot \mathbf{D} = \varrho_\mathrm{f} \ , \tag{2.10}$$

where

$$\mathbf{D} = \varepsilon_0 \mathbf{E} + \mathbf{P} \tag{2.11}$$

represents the relation between the dielectric displacement $\mathbf{D}$, the electric field $\mathbf{E}$ and the electric polarization $\mathbf{P}$. Similarly, the Ampere-Maxwell law reads

$$\nabla \times \mathbf{H} = \mathbf{j}_\mathrm{f} + \frac{\partial \mathbf{D}}{\partial t} \ , \tag{2.12}$$

where

$$\mathbf{H} = \frac{1}{\mu_0}\mathbf{B} - \mathbf{M} \tag{2.13}$$

represents the relation between the magnetic field $\mathbf{H}$, the magnetic induction $\mathbf{B}$ and the magnetization $\mathbf{M}$.

In linear and isotropic media, polarization and magnetization vectors are proportional to the external fields

$$\mathbf{P} = \varepsilon_0 \chi_\mathrm{e} \mathbf{E} \ , \tag{2.14}$$

$$\mathbf{M} = \chi_\mathrm{m} \mathbf{H} \ , \tag{2.15}$$

where χ_e and χ_m are electric and magnetic susceptibilities, respectively.

Furthermore, the relative permittivity ε_r and permeability μ_r are defined as

$$\varepsilon_\mathrm{r} = \frac{D}{\varepsilon_0 E} = 1 + \frac{P}{\varepsilon_0 E} \ , \tag{2.16}$$

and

$$\mu_\mathrm{r} = \frac{B}{\mu_0 H} = 1 + \frac{M}{H} \ . \tag{2.17}$$

Considering Equations 2.14 and 2.15, the relations between $\mathbf{E}$, $\mathbf{D}$ and $\mathbf{B}$, $\mathbf{H}$ for linear homogeneous and isotropic media read

$$\mathbf{D} = \varepsilon_0 \varepsilon_\mathrm{r} \mathbf{E} \ , \tag{2.18}$$

$$\mathbf{B} = \mu_0 \mu_\mathrm{r} \mathbf{H} \ , \tag{2.19}$$

where $\varepsilon_\mathrm{r} = 1 + \chi_\mathrm{e}$, $\mu_\mathrm{r} = 1 + \chi_\mathrm{m}$ hold. The frequency dependent relative permittivity $\varepsilon_\mathrm{r} = \varepsilon(\omega)$ is often called a dielectric function.

Some models of the relative permittivity for metals and materials possessing the Lorentzian resonance are referred in Section 2.4.

2.1.2 Boundary conditions

The integral forms of the Maxwell equations provide the conditions at interfaces that are used in the solution of SPPs. Therefore, they are discussed in the following.

The Maxwell equations may be expressed in the integral form by applying the Gauss-Ostrogradsky divergence theorem and the Stokes theorem [48]. In particular,

$$\oint\limits_{\sum} \mathbf{D} \cdot \mathrm{d}\mathbf{S} = Q_\mathrm{f} \ , \tag{2.20}$$

$$\oint\limits_{\sum} \mathbf{B} \cdot \mathrm{d}\mathbf{S} = 0 \ , \tag{2.21}$$

are the Gauss laws where the integrals are considered over any closed surface $\sum$; and

$$\oint\limits_{\partial\Omega} \mathbf{E} \cdot \mathrm{d}\mathbf{s} = -\frac{\mathrm{d}}{\mathrm{d}t} \int\limits_{\Omega} \mathbf{B} \cdot \mathrm{d}\mathbf{S} \ , \tag{2.22}$$

$$\oint\limits_{\partial\Omega} \mathbf{H} \cdot \mathrm{d}\mathbf{s} = I_\mathrm{f} + \frac{\mathrm{d}}{\mathrm{d}t} \int\limits_{\Omega} \mathbf{D} \cdot \mathrm{d}\mathbf{S} \ , \tag{2.23}$$

are the Faraday and the Ampere-Maxwell laws, respectively, that hold for any surface Ω bound by closed loop $\partial\Omega$.

Integrating the electric displacement and the magnetic induction (Equations 2.20 and 2.22) over a block extending only slightly into both materials gives

$$(\mathbf{D}_1 - \mathbf{D}_2) \cdot \mathbf{n} = \sigma_\mathrm{f} \ , \tag{2.24}$$

$$(\mathbf{B}_1 - \mathbf{B}_2) \cdot \mathbf{n} = 0 \tag{2.25}$$

where $\mathbf{n}$ is a normal vector pointing outwards the boundary area and σ_f is a free surface charge density.

Similarly, the further boundary conditions

$$\mathbf{n} \times (\mathbf{E}_1 - \mathbf{E}_2) = \mathbf{0} \ , \tag{2.26}$$

$$\mathbf{n} \times (\mathbf{H}_1 - \mathbf{H}_2) = \mathbf{K}_\mathrm{f} \tag{2.27}$$

are obtained by evaluating the circulation of electric and magnetic intensities (Equations 2.22 and 2.23) over the loop bounding an area ($S \to 0$) that is perpendicular to the interface. Note, that $\mathbf{K}_\mathrm{f}$ is the free surface current density. Equations 2.24, 2.25, 2.26 and 2.27 represent the general boundary conditions in electrodynamics which will be used also in our calculations in Section 2.5.

2.2 Surface plasmon polaritons

Surface plasmon polaritons (SPPs) represent one of the essential terms discussed in this work. SPPs represent the quanta of surface charge-density oscillations coupled to electromagnetic waves propagating along the metal-dielectric interface [3], [4], [5], [6]. SPPs are solutions to the Maxwell equations where fields $\mathbf{E}$ and $\mathbf{H}$ decay exponentially from the interface into dielectric and metal,

$$E_i(x,z),\ H_j(x,z) \propto \mathrm{e}^{\mathrm{i}\beta x - k|z|} \tag{2.28}$$

where β is the propagation constant and k is the decay constant in a material.

Figure 2.1 illustrates single interface geometry. The interface defined as x-y plane at $z = 0$ separates a space into two regions. A dielectric with a relative permittivity ε_2 and a metal with a relative permittivity $\varepsilon_1(\omega)$ are situated in regions for $z > 0$ and $z < 0$, respectively.

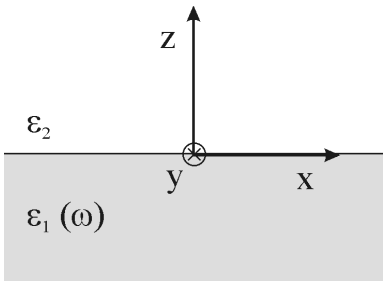

Figure 2.1: The schematic of a metal-dielectric interface. The x-y plane at $z = 0$ separates a space into a region with $z > 0$ occupied by a dielectric with ε_2 and a region with $z < 0$ occupied by a metal with $\varepsilon_1(\omega)$ being frequency dependent.

Considering both mediums are isotropic it is possible to handle p- and s-polarizations separately. The boundary conditions (see Section 2.1.2) for p-polarization (TM) yields

$$\frac{k_1}{\varepsilon_1} = -\frac{k_2}{\varepsilon_2} \ . \tag{2.29}$$

As decay constants k_1 and k_2 in metal and dielectric (respectively) are positive the Equation 2.29 is fulfilled only if $\mathrm{Re}(\varepsilon_1) < 0$ (see Fig. 2.5). Inserting formulas

$$k_1^2 = \beta^2 - \frac{\omega^2}{c^2}\varepsilon_1(\omega) \ , \tag{2.30}$$

$$k_2^2 = \beta^2 - \frac{\omega^2}{c^2}\varepsilon_2 \ , \tag{2.31}$$

yielded by the wave equation in metal and dielectric, respectively, relating the frequency of the wave ω, propagation constant β, decay constants k_1, k_2 and permittivities ε_1, ε_2 into the condition 2.29 we get the dispersion relation of SPPs

$$\beta(\omega) = \frac{\omega}{c}\sqrt{\frac{\varepsilon_1(\omega)\varepsilon_2}{\varepsilon_1(\omega)+\varepsilon_2}} \ . \tag{2.32}$$

Considering $\varepsilon_1(\omega) = \varepsilon_1'(\omega) + \mathrm{i}\varepsilon_1''(\omega)$ complex, $\beta = \beta' + \mathrm{i}\beta''$ holds where

$$\beta'(\omega) = \frac{\omega}{c}\sqrt{\frac{\varepsilon_1'(\omega)\varepsilon_2}{\varepsilon_1'(\omega)+\varepsilon_2}} \ , \tag{2.33}$$

$$\beta''(\omega) = \frac{\omega}{c}\sqrt{\left(\frac{\varepsilon_1'(\omega)\varepsilon_2}{\varepsilon_1'(\omega)+\varepsilon_2}\right)^3}\frac{\varepsilon_1''(\omega)}{2\varepsilon_1'^2(\omega)} \ . \tag{2.34}$$

Imaginary part of β determines the propagation length

$$L = \frac{1}{2\beta''} \tag{2.35}$$

in which the surface wave loses its intensity relatively by the value 1/e. This length reaches tens of micrometers for metals possessing high free-electron concentration in the visible range. In infrared, this distance reaches hundreds of micrometers.

The reciprocal values of real parts of decay constants (Equations 2.30)

$$\hat{z}_1 = \frac{1}{\mathrm{Re}(k_1)} = \frac{c}{\omega}\sqrt{\frac{\varepsilon_1'(\omega)+\varepsilon_2}{\varepsilon_1'^2(\omega)}} \ , \tag{2.36}$$

$$\hat{z}_2 = \frac{1}{\mathrm{Re}(k_2)} = \frac{c}{\omega}\sqrt{\frac{\varepsilon_1'(\omega)+\varepsilon_2}{\varepsilon_2^2}} \ , \tag{2.37}$$

determine distances at which the field falls relatively by 1/e in a metal and dielectric, respectively.

The boundary condition for s-polarized (TE) wave yields

$$k_1 = -k_2 \tag{2.38}$$

which cannot be fulfilled for any frequency. Thus, s-polarized (TE) wave does not exist.

As an example, the dispersion relation of SPPs for the gold-vacuum interface described by the Drude model (see Section 2.4.1) is shown in Fig. 2.2. The dispersion relation

consists of two branches: the Brewster branch and the SPPs branch for frequencies above and below the plasma frequency ω_p, respectively. The Brewster branch represents the solution where the field is not confined to the interface. On the other hand, the branch of lower frequencies represents a mode of propagating wave confined to the interface. The dispersion relation of SPPs is situated below the light line. For $\beta \to 0$, when the dispersion relation approaches the light line, the waves are called the Sommerfeld-Zenneck waves. For higher frequencies, the dispersion relation begins to bend and reaches its maximum

$$\omega_s = \frac{\omega_p}{\sqrt{1+\varepsilon_2}} \tag{2.39}$$

called the surface plasmon frequency.

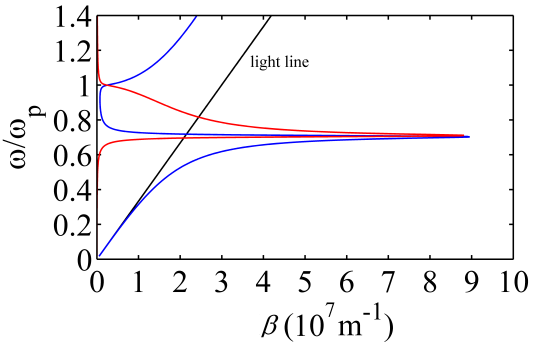

Figure 2.2: The dispersion relations of SPPs on the surface of silver with the plasma frequency $\omega_p = 0.9 \cdot 10^{16} s^{-1}$ and the damping coefficient $\gamma = 4.353\ 10^{12} s^{-1}$ [50]. Its real and imaginary parts are depicted by blue and red curves, respectively.

The propagation constant of SPPs remains larger than that for light at a given frequency. Thus, SPPs have a shorter wavelength than light. In consequence, SPPs cannot be transferred into light spontaneously and cannot be excited via a simple illumination of a flat metallic surface.

Double interface SPPs

When the metal-dielectric interfaces are close enough to each other, the SPPs propagating along upper and lower interfaces begin to interact. The interaction gives rise to the coupled modes of SPPs [51]. In particular, for insulator-metal-insulator or metal-insulator-metal multi-layers the following p-polarized modes exist [1]

- the odd mode where E_x is odd and H_y, E_z are even functions; and
- the even mode where E_x is even and H_y, H_z are odd functions.

The dispersion relations of SPPs for an air-silver-air multilayer with the thickness of the metallic layer of 100 nm and 50 nm are shown in Fig. 2.4. The upper and lower branches denote dispersion relations of the odd and even modes, respectively.

[1] The terminology is not consistent (see [6]).

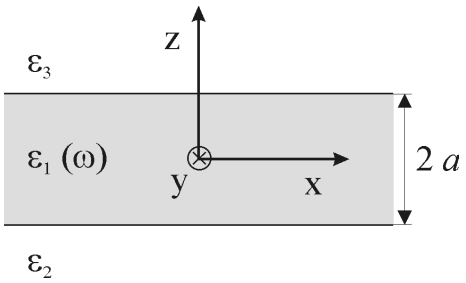

Figure 2.3: The insulator – metal – insulator structure. Only ε_1 is dependent on ω. The layers are spread to infinity along x- and y- directions.

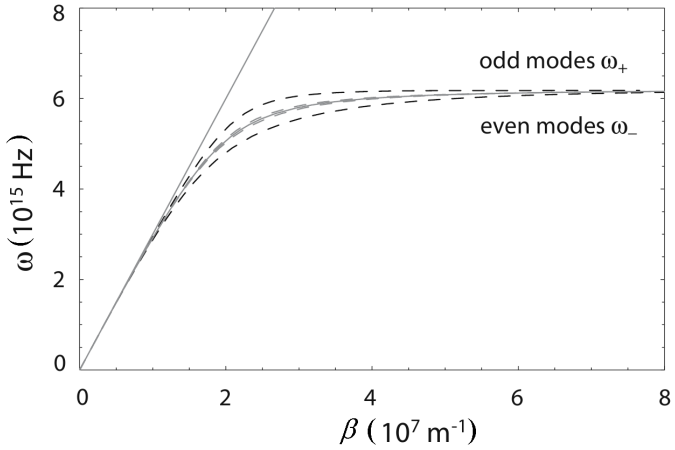

Figure 2.4: The dispersion relation of SPPs at an air-silver-air multilayer with a metal core of the thickness of 100 nm (dashed gray curves) and 50 nm (dashed black curves). SPPs at a single layer possess dispersion relation denoted by the gray curve. Silver dielectric function was modelled by the Drude with negligible damping. The figure is taken from [7].

2.2.1 Excitation and near-field detection of SPPs

SPPs should be excited by different ways which are thoroughly discussed in [5]. The most often used methods take advantage of the attenuated total reflection (ATR). In particular, there are the Kretschmann [11] and the Otto configurations [12], where the evanescent behaviour of SPPs is used. Another way of the excitation is based on scattering of the electromagnetic field on grooves (or other scatterers, roughness, etc.) [4], [52].

The scattering of SPPs can be seen in the far-field; on the other hand, SPPs itself can be observed by scanning near-field optical microscopy (SNOM) where the evanescent behaviour of SPPs is used. Owing to low sampling frequencies of detectors (compared to frequencies of light) near field techniques are able to collect only mean-time signals. Therefore, only interference of SPPs may be observed by this method. The SPPs interference may be exploited in 2D optics [53] as diffraction and interference of light in 3D.

The interference of SPPs was verified in the near-field by the experiment similar to the interference of light passing through the screen with two slits [54]. Another interference experiment was the realization of the Mach-Zehnder interferometer in the near-field [55]. Furthermore, the change of the dielectric function of cobalt by an external magnetic field

was interferometrically observed via SPPs [56]. In addition, experiments with inhomogeneous excitations on four perpendicular grooves forming a square at the metallic surface were performed at IPE BUT [57], [58], [59], [60].

2.3 Localized plasmon polaritons

The solutions of Maxwell equations yielded SPPs propagating along single- and multi-interfaces of infinite dimensions in a plane were shortly discussed in the previous Section 2.2. In this Section, metallic objects of dimensions smaller than wavelengths of incident light are discussed. Such truncated structures are called resonant plasmonic structures or plasmonic antennas.

Properties of resonant plasmonic structures represent the main task of this work studied in Chapter 3.

Resonant structures excited by the electromagnetic field [14] exhibit interesting phenomena. The significant enhancement of the electromagnetic field intensity by up to 4 orders of magnitude occurs at the resonance frequency of structures in their vicinity [2]. Moreover, resonance wavelengths of antennas are dependent significantly on the refractive index of their environment [61], [62], [63]. Further applications of plasmonic antennas are discussed in the introduction of Chapter 3.

Analytical solutions of scattering of the electromagnetic waves are available only for metallic spheres or ellipsoids [49], [64], [65]. Any further structures (e.g. metallic blocks) are computable only numerically, except some approximative analytical solutions [66], [67], [68], solutions based on discrete dipole approximation [69] and solutions exploiting the conformal transformation [70], [71].

2.4 Optical properties of materials

In this work, the significant attention is paid to studying a response of metallic resonant antennas to the electromagnetic field with a dielectric in their vicinity (Section 3.2). Especially, interesting phenomena occur when this dielectric possesses the pronounced dispersion of its refractive index (Sections 3.3 and 3.4). Therefore, models describing optical properties of metals and dielectrics (possessing vibration modes) are referred in Sections 2.4.1 and 2.4.2, respectively.

2.4.1 Drude model

Optical properties of metals are usually described by the Drude model. The Drude model considers a metal as a free electron gas moving in response to the applied electromagnetic field. The equation of motion of a free electron (of the mass m_e) forced by the electric field reads

$$m_{\mathrm{e}}\ddot{\mathbf{x}} + m_{\mathrm{e}}\gamma\dot{\mathbf{x}} = -e\mathbf{E}(t) \ , \tag{2.40}$$

where $\gamma = 1/\tau$ is the damping coefficient (or collision frequency) with τ denoting the mean time between electron collisions. For the time-harmonic dependence $\mathrm{e}^{-\mathrm{i}\omega t}$ of the elec-

[2] The field enhancement is given by the quality factor of given structures [14].

tric field the steady-state solution reads

$$\mathbf{x}(t) = \frac{e}{m_{\mathrm{e}}(\omega^2 + \mathrm{i}\gamma\omega)}\mathbf{E}(t) \ . \tag{2.41}$$

The electric polarization reads

$$\mathbf{P}(t) = -ne\mathbf{x}(t) = -\frac{ne^2}{m_{\mathrm{e}}(\omega^2 + \mathrm{i}\gamma\omega)}\mathbf{E}(t) \ , \tag{2.42}$$

where n is the density of electrons. When inserting Equation 2.42 into Equation 2.16 the dielectric function of the free electron gas reads

$$\varepsilon(\omega) = 1 - \frac{\omega_{\mathrm{p}}^2}{\omega^2 + \mathrm{i}\gamma\omega} \ , \tag{2.43}$$

where

$$\omega_{\mathrm{p}} = \sqrt{\frac{ne^2}{m_{\mathrm{e}}\varepsilon_0}} \tag{2.44}$$

is the plasma frequency. The real and imaginary parts of the dielectric function read

$$\varepsilon'(\omega) = 1 - \frac{\omega_{\mathrm{p}}^2}{\omega^2 + \gamma^2} \ , \tag{2.45}$$

$$\varepsilon''(\omega) = \frac{\omega_{\mathrm{p}}^2\gamma}{\omega(\omega^2 + \gamma^2)} \ . \tag{2.46}$$

As an example, the dielectric function of gold obtained from the Drude model and from sampled data in [50] involving interband transitions is shown in Fig. 2.5.

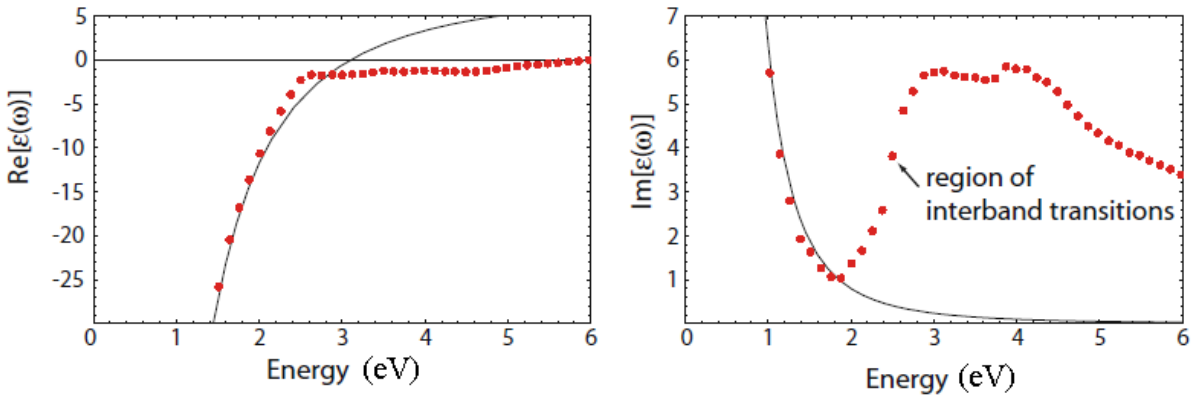

Figure 2.5: The dielectric function of gold taken from the Drude model and from sampled data [50] involving the interband transitions. The image is taken from [7].

2.4.2 Lorentz model

Optical properties of dielectrics in infrared originates from lattice vibrations and vibration and rotation modes of molecules. Here, dielectric functions are described by a model of forced harmonic oscillators [65] called The Lorentz model. The equation of motion reads

$$m\ddot{\mathbf{x}} + m\gamma\dot{\mathbf{x}} + K\mathbf{x} = -e\mathbf{E}(t) \ . \tag{2.47}$$

where K is the restoring constant and $\gamma = b/m$ is the damping coefficient. For the time-harmonic dependence $\mathrm{e}^{-\mathrm{i}\omega t}$ of the electric field the steady-state solution reads

$$\mathbf{x}(t) = -\frac{e/m}{\omega_0^2 - \omega^2 - \mathrm{i}\gamma\omega}\mathbf{E}(t) \ , \tag{2.48}$$

where $\omega_0^2 = K/m$ is the eigenfrequency of the oscillator.

Consequently, the dielectric function reads

$$\varepsilon(\omega) = \varepsilon_\infty + \frac{G\Omega^2}{\omega_0^2 - \omega^2 - \mathrm{i}\gamma\omega} \ , \tag{2.49}$$

where ε_∞ represents the permittivity at high frequencies, G is the oscillator strength, Ω is so-called plasma frequency of the ion lattice.

The dielectric function of a real matter is usually fitted by a sum of oscillators described by Equation 2.49. As an example, Fig. 2.6 shows dielectric functions of amorphous SiO_2 [72], exhibiting one infrared resonance, and silicon-rich oxinitride (SRON) fitted by a sum of four oscillators (see Section 3.1).

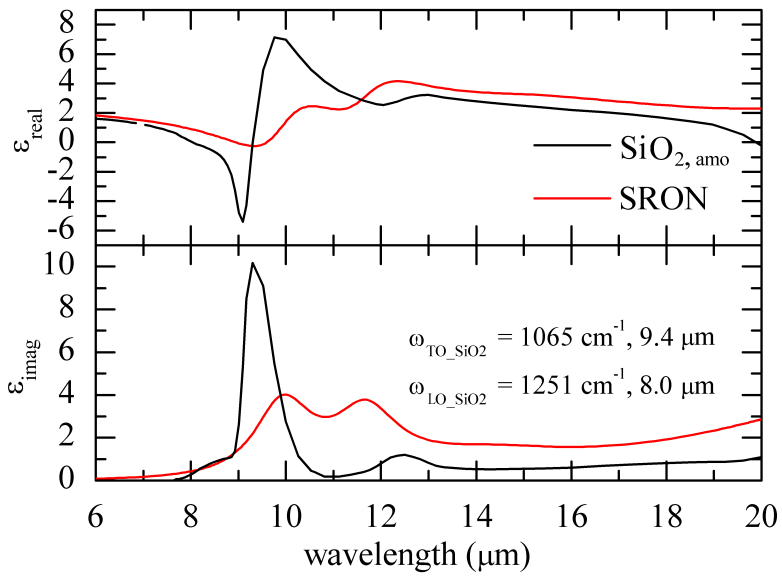

Figure 2.6: The comparison of the dielectric functions of SRON and SiO_2.

2.5 Computation of electromagnetic field

A computation of the electromagnetic field provides useful information about properties of plasmonic antennas discussed in Sections 3.3 and 3.4. Electromagnetic fields can be calculated analytically or numerically. Analytical methods represent mathematically exact solutions providing the physical background, on the other hand, they exist only for few geometry configurations.

Related to plasmonics, analytical solutions of SPPs have been found for infinite metal-dielectric interface/s [1], [2], [3]. Consequently, solutions of SPPs scattered by various defects such as grooves, a roughness or impurities were studied in [4], [73]. Analytically solvable resonant plasmonic structures are only the spheres and ellipsoids [64], [65], [74]. Besides that, nanorod-like structures were studied analytically for example in [66] where the theory of waveguides was applied. In [68], the response of a free-electron gas within a metallic nanorod to the electromagnetic field was studied. Semi-analytical solution of spectral properties based on reflections of SPPs at antenna edges was presented in [75].

Numerical computations are able to provide the electromagnetic response to structures of different shapes and dimensions but the physical interpretation is often not straightforward. The Maxwell equations can be numerically solved by widely spread finite-difference methods and finite-elements methods in time- or frequency-domains.

The finite-difference method is based on an approximation that permits replacing differential equations by finite difference equations. The finite-difference method is often used in time-domain methods. On the other hand, the finite-elements method is based on eliminating time derivatives [76].

The advantage of the finite-elements method compared to the finite-difference method lies in the use of meshing elements of arbitrary shape. However, the triangulation is the most widely used discretization by the FEM method. On the other hand, the finite-difference methods can be relatively easily implemented [77]. For instance, there exist also implementations into spreadsheet software [75].

There exist two modes of treating the simulations in the electrodynamics. The time-domain method provides the electromagnetic field at (semi-)continuous time. It involves the causality so it treats also the transient response [76]. Therefore, it handles pulse evolution including the behaviour of precursors. In cases when a wave packet is used as the source of the electromagnetic field one simulation-run provides the spectral response [3]. In contrast, the frequency-domain method allows calculating steady state modes. It is based on the solution of the Maxwell equations in the form of the vector Helmholtz equation for the electric/magnetic field.

The finite-difference time-domain method (FDTD) is probably the most popular numerical simulation technique providing spectral responses in the electrodynamics. Also, a majority of simulations performed in this work has been done via FDTD (e.g. Section 3.3). The name "FDTD" originates from [78] and it was firstly introduced by Kane. S. Yee's [79] algorithm. In this algorithm different components of the electromagnetic field are computed for different positions or time [4]. The space is divided into rectangles

[3] To obtain the spectral response raw simulation data must be treated by the Fourier transform.

[4] It is a disadvantage because the full-field (electric and magnetic) is not evaluated at the same position. Therefore, some interpolations of the field should be done.

or block-like elements in 2D or 3D, respectively. Then, the space is described by the Cartesian rectangular coordinate system.

As mentioned above, the FDTD method approximates spatial and temporal derivatives appeared in the Maxwell equations by corresponding finite differences. In particular, the differences are expressed by the first-order Taylor expansion $\frac{\mathrm{d}f(x)}{\mathrm{d}x}|_{x=x_0} \approx \frac{f(x_0+\mathrm{d}x/2)-f(x_0-\mathrm{d}x/2)}{\mathrm{d}x}$ [5]. Thus, the FDTD method is the central-difference approximation that relates the function in the point x_0 where the space is not sampled with neighbouring (sampled) points $x_0 - \Delta x/2$ and $x_0 + \Delta x/2$ [6]. The Kane Yee algorithm [79] for FDTD is the most widespread for FDTD. The algorithm procedure contains following steps.

- Replace all derivatives by finite differences.
- Divide space and time in order to alternate the electric and magnetic fields in time and space. For instance of 1D space in axis x, the space and time are divided by $\Delta x/2$ (half spatial-step) and $\Delta t/2$ (half time-step), respectively. Then, the Courant number (Courant-Friedrichs-Lewy) defined as the ratio $c' = \Delta t/\Delta x$ determines the simulation stability [7] and it must be smaller or equalled to 1 everywhere and every time.
- Express update-difference-equations determining future fields in terms of past fields.
- Evaluate the magnetic fields one step into the future so they become past and known.
- Evaluate the electric fields one step into the future so they become past and known.
- Repeat previous two steps until the required duration time of the simulation.

One example should be demonstrated for the isotropic medium without charges. For the field E_z propagating in x direction the Maxwell equations reduce to

$$\mu \frac{\partial H_y}{\partial t} = \frac{\partial E_z}{\partial x} \,, \tag{2.50}$$

$$\varepsilon \frac{\partial E_z}{\partial t} = \frac{\partial H_y}{\partial x} \tag{2.51}$$

with H_y being the only non-zero magnetic component.

The computation steps are shown in Figure 2.7 where all fields below the dashed line are considered known. Note, that fields in the present time possess the superscript ^{q} and $[m]$ denotes an index of the position. It is worth mentioning Figure 2.7 reveals that the electric and magnetic fields are never known for the same position and time. In particular, the electric and magnetic fields are mutually separated by $\Delta x/2$ and by $\Delta t/2$ in space and time, respectively. On the other hand, the same fields (either electric or magnetic) are separated by Δx and Δt in space and time, respectively. The steps are described in more detail below.

[5] Higher-order series of expansion should be used, but it requires more sample points to be reckon on.

[6] FDTD is called the second-order central-difference approximation.

[7] For a given space-discretization, the limit on the time-step is defined and reads $\Delta t < \frac{1}{c'\sqrt{\frac{1}{\Delta x^2}+\frac{1}{\Delta y^2}+\frac{1}{\Delta z^2}}}$.

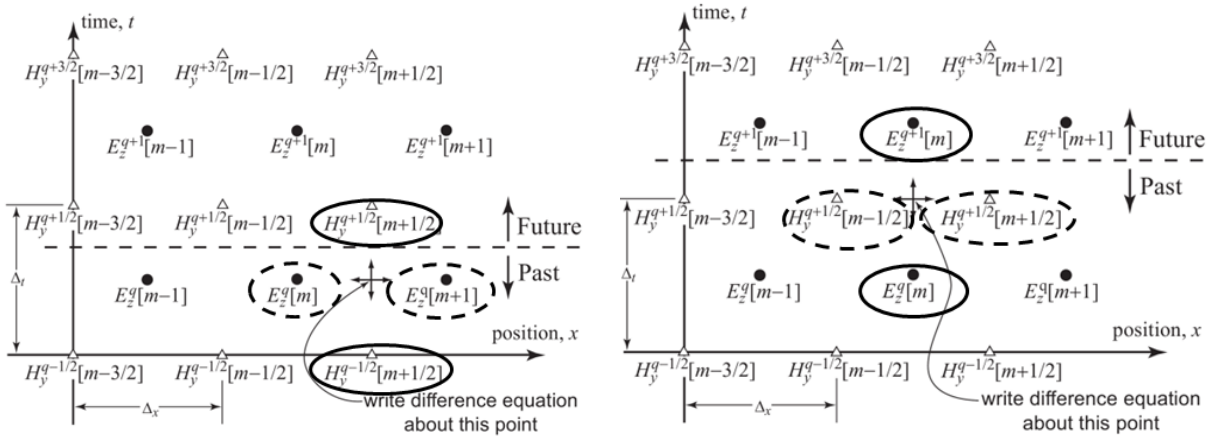

Figure 2.7: The magnetic and electric fields computed for $(t + \Delta t/2,\ x + \Delta x/2)$ and $(t + \Delta t,\ x)$, respectively. Taken from [80].

The magnetic field $H_y(t + \Delta t/2, x + \Delta x/2)$ (see Figure 2.7 a)) should be computed by the Faraday law 2.50 that becomes $\mu\frac{H_y^{q+\frac{1}{2}}[m+\frac{1}{2}]-H_y^{q-\frac{1}{2}}[m+\frac{1}{2}]}{\Delta_t} = \frac{E_z^q[m+1]-E_z^q[m]}{\Delta_x}$. This equation relates the solution to the unknown magnetic field $H_y(t + \frac{\Delta t}{2}, x + \frac{\Delta x}{2})$ in the future denoted by $H_y^{q+\frac{1}{2}}[m + \frac{1}{2}]$ with the known magnetic field at the same position in the past (before $\Delta t \equiv {}^{q}$) and with the electric fields in neighbouring positions in the meantime. In particular,

$$H_y^{q+\frac{1}{2}}[m + \frac{1}{2}] = H_y^{q-\frac{1}{2}}[m + \frac{1}{2}] + \frac{\Delta_t}{\mu\Delta_x}(E_z^q[m + 1] - E_z^q[m]) \tag{2.52}$$

is called the update equation for the magnetic field.

After the fields are known for time $t + \Delta t/2$, the electric field $E(t + \Delta t, x)$ should be computed by the Ampere law as shown in Figure 2.7 b). Then, the electric field reads the Ampere law 2.51: $\varepsilon\frac{E_z^{q+1}[m]-E_z^q[m]}{\Delta_t} = \frac{H_y^{q+\frac{1}{2}}[m+\frac{1}{2}]-H_y^{q+\frac{1}{2}}[m-\frac{1}{2}]}{\Delta_x}$ that relates the future electric field $E_z(t + \Delta t, x)$ with the electric field at the same point in the past (before Δt) and neighbouring known magnetic fields $(t + \Delta t/2)$. In particular,

$$E_z^{q+1}[m] = E_z^q[m] + \frac{\Delta_t}{\varepsilon\Delta_x}(H_y^{q+\frac{1}{2}}[m + \frac{1}{2}] - H_y^{q+\frac{1}{2}}[m - \frac{1}{2}]) \tag{2.53}$$

is called the update equation for the electric field.

In 3D space, the spatial nodes are organized in the Yee cell depicted in Figure 2.8 where magnetic and electric components are computed on cell's faces and in cell's edges, respectively.

The capability of the FDTD method is continually extending. The implementation of boundaries in the simulation was fully sorted out and it was enlarged for treating impulses and non-linear behaviours [76]. Solutions of curved structures were improved by effective permittivity [81], [82], [83]. Accurate simulations of thin structures were allowed in [84],

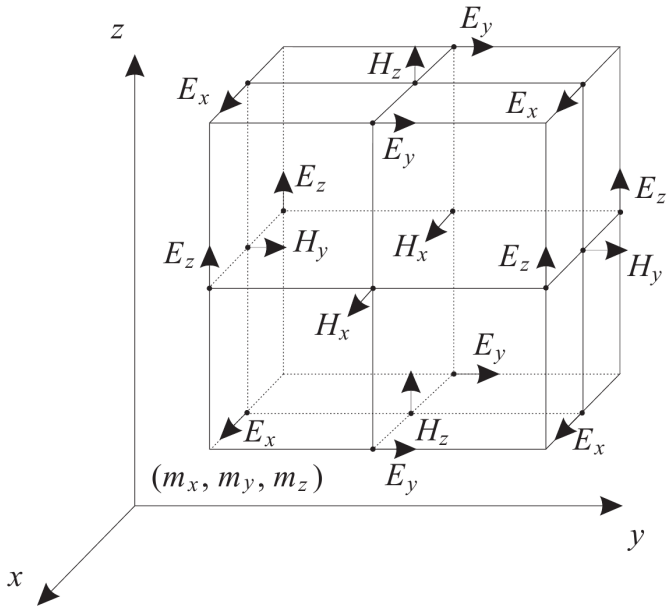

Figure 2.8: The Yee cell in 3D space. The magnetic and electric components are computed on cell's faces and in cell's edges, respectively.

[85]. Improvement of the FDTD via implementing the total-field scattered-field (TFSF) algorithm [86] allows not only the separation of total and scattered fields in the given space, but it even reduces the reflection of the incident field on simulation boundaries. Nowadays, FDTD represents a powerful method utilized in user-friendly software packages possessing the graphical user interface. For instance, the simulations performed in presented work have been done by [87].

3. Plasmonic resonant structures

Plasmonic resonant structures (plasmonic antennas, metallic spheres, etc.) are used in the majority of plasmonics applications [23], [24], [25], [26], [27]. Thus, plasmonic antennas and their properties represent the main tasks of this work where the emphasis is put on an enhancement of the electromagnetic field in the near-field (Section 3.3) and on sensing applications (Sections 3.3, 3.4).

Plasmonic antennas have received a significant attention for their ability to concentrate the light energy into deep-subwavelength dimensions and for their resonance-sensitivity to environments they are embedded in [88]. In consequence, the plasmonic resonance may enhance the absorption of the electromagnetic field energy that can be used in the photoluminescence [35], the excitation of electron-hole pairs in semiconductors [19], in photovoltaics [32] and others [89].

Considering the absorption, much work has been done on plasmonic resonant structures (antennas) with respect to their heating properties. Most of such articles deal with the electromagnetic field absorption (and the corresponding heat development) in metallic parts of resonant structures embedded in transparent, non-absorbing environments [40], [41], [90], [91]. The enhancement of the heat generation via plasmonic resonances and a consequent temperature increase have not been studied only by simulations [40], [41], but also experimentally [42], [92]. The heat power enhanced by this method was utilized for instance in infrared spectrometers, bolometers [93], [94], [95], [96], local growth of nanowires, in the phase transformation of materials in the antenna vicinity [91], [97], [98] and in other applications.

Furthermore, plasmonic structures found useful application in the enhancement of the signal in the Raman spectroscopy. There are two techniques: the Surface-Enhanced Raman Scattering (SERS) and the Tip-Enhanced Raman Spectroscopy (TERS). In SERS, the plasmonic effect occurs on a rough metallic surface. It enables the enhancement of the Raman signal by 4-8 orders of its magnitude [99], [100], [101], [102], [103], [104]. Consequently, even a single-molecule sensitivity has been observed [105]. The second technique called the Tip-Enhanced Raman Spectroscopy (TERS) enables mapping of plasmonically enhanced Raman signal by using a scanning-probe technique. The field is enhanced by the plasmonic resonance of either metallic structures placed at an AFM probe or a metal-coated AFM probe itself [31], [106], [107]. Then, the Raman spectra should be mapped with a resolution below the diffraction limit.

Besides methods for the enhancement of the Raman signal, plasmonic infrared spectroscopic techniques like the Surface Enhanced Infrared Absorption (SEIRA) [108] and the Surface Enhanced Infrared Spectroscopy (SEIRS) are frequently studied nowadays [109], [110], [111], [112], [113]. These techniques may provide information about chemical compositions (vibrational spectroscopy) of specimens. Furthermore, scanning-probe modifications of these plasmonic infrared spectroscopies allow to map the specimens. It has been demonstrated that scattering-type scanning near-field optical microscope is able to map the vibrational spectra with a spatial resolution roughly 1000 times better than conventional methods such as the FTIR [29]. For instance, objects as viruses as small as

18 nm have been observed in [114].

Obviously, the applications presented above require a comprehensive study of plasmonic antennas with purpose to reveal their resonances, electromagnetic field enhancement and distribution, mutual interactions, interactions with surrounding materials, etc. This represents the motivation for a basic research of antenna resonances [27], [24], [115], [116], [117], [118]. For instance, the sharp features (peaks/dips) in spectral responses of plasmonic structure interacting with the environment are compared with the hybridization states in the molecular orbital theory (including Fano resonances) in [117], [119], [120], [121].

The resonant plasmonic antennas represent the main subject of interest of the presented work. This complex work involves numerical modelling of antennas, fabrication of antennas (based on a design proposed by simulations) and optical measurements of these antennas. Therefore, this work represents theoretical and experimental study of plasmonic antennas as well.

In particular, the fabrication of plasmonic antennas via the electron beam lithography and via the focused ion beam is discussed in Section 3.1. The following Section 3.2 deals with resonant properties of antennas in general. Sections 3.3 and 3.4 are focused on resonance properties of antennas placed on a layer with a pronounced dispersion of its dielectric function in mid-infrared [62], [63]. Owing to the fact that the plasmonic resonances can be excited not only by the electromagnetic field in the conventional form (light) but also locally by passing electrons [119], [122] the measurement of the cathodoluminescence on (visible) plasmonic antennas was also performed and it is discussed in Section 3.5.

3.1 Fabrication of antennas

Studying the optical properties of plasmonic antennas is hardly possible without measurements on real plasmonic structures. Plasmonic antennas studied in Sections 3.3, 3.4 and 3.5 were fabricated by techniques discussed below.

The quality of fabricated plasmonic structures is the most critical point that often makes theoretical (simulated) results different to experimental ones. The difference is determined mainly by a distinction between theoretical and real dielectric functions and by the topography of fabricated structures [1].

In the presented work, plasmonic structures were prepared by techniques exploiting accelerated focused beams of electrons or ions. Namely,

- the electron beam was used in the lithography-like technique called the electron beam lithography (EBL) (see Section 3.1.1). During the lithography, the beam modifies the electron-sensitive (positive-tone [2]) resist in the scanned domains. Afterwards, these domains are removed during the development of the resist. The metallic layer is deposited directly on the substrate in the scanned areas. Consequently, the resist is chemically removed, i.e. areas with the resist present below the

[1] The resultant quality of fabricated structures prepared by both techniques is also determined by properties of processed matter.

[2] Note, there exists also a negative-tone resist. Its unmodified part is removed during the development. Consequently, fabricated structures are situated in an unexposed area.

metal are lifted off and only the parts where the metal is connected directly to the substrate remains on the sample.

- the focused ion beam (FIB) of Ga^+ (or Xe) ions is used for etching the material (see Section 3.1.2). The fabrication of plasmonic structures usually lies in etching the (previously deposited) metallic layer. Consequently, the non-etched area of the sample represents the resultant plasmonic structure of required geometry. However, the FIB implants ions of Ga^+ and ions of the etched metallic layer into a substrate. Also, the remaining material can get amorphous [123].

Although EBL and FIB techniques are widespread and well known they are shortly discussed with an emphasis on the fabrication of plasmonic antennas in following Sections 3.1.1 and 3.1.2.

3.1.1 Electron beam lithography

The electron beam lithography is a traditional patterning mask-less technique. The resolution of patterning is proportional to the beam-spot diameter, the size of a scanning step and most significantly to the resolution of the resist. Nevertheless, the EBL is able to fabricate subwavelength structures with dimension well below one hundred nanometers. Furthermore, the two-step lithography enables the fabrication of 3-dimensional structures or structures made of different materials. On the other hand, EBL is more time-consuming than the conventional optical lithography.

In this work, poly-methyl-methacrylate (PMMA) is used as a resist because of its high resolution. The disadvantage of PMMA is that it has a low sensitivity to the exposition dosage and a poor etching durability. The EBL has been performed by microscopes FIB/SEM Tescan Lyra3 XMH, SEM Tescan Mira3 + Raith or SEM Tescan Vega - L04 at the department [124].

The EBL procedure used in this work comprises following steps:

- cleaning of the sample successively in acetone, isopropyl alcohol (IPA) and flowing demineralized water finished by drying by nitrogen [3].

- spin-coating of the resist on the substrate. The thickness of PMMA resist varied in range of 80-280 nm. It was determined by the concentration of PMMA in a solution, by the speed and acceleration of spinning, and by the adhesion between the resist layer and the substrate. To obtain a high homogeneity of the resist layer, the adhesion should be enhanced by the coating of the spacer-layer (Microchem, Primer 80/20) below the resist.

- exposition of the resist by the electron beam. Although the spot diameter of the beam reaches units of nanometers, the presence of backscattered, secondary electrons and scattering of primary electrons is responsible for remarkable broadening of exposed areas [126]. Then, the resultant resolution reaches 20 nm for PMMA resist. The degree of exposition is determined by an exposure dose denoting a number of

[3] Also, the sample should be cleaned in the piranha solution that removes most organic matter [125].

electrons per area [4]. The required dose is proportional to the thickness of PMMA layer and varied between 80-380 μC/cm^2.

- development of the exposed sample in MIBK:IPA (1:3) solution for 90 s followed by dipping in IPA (more than 30 s), cleaning in flowing demineralized water (30-60 s), and drying out by nitrogen.

- deposition of the metallic layer. It was always performed by ion beam assisted deposition (IBAD) technique in the apparatus Kaufman (at IPE department).

- lift-off preceded by dipping the sample in acetone over-night. Lift-off means to keep the sample still in acetone and to spray acetone onto the sample to remove the resist from it. Afterwards, the sample is put into IPA for 30 s and then washed in flowing demineralized water. At the end, the specimen is dried out in blowing nitrogen.

Obviously, the resolution and quality of structures represent the main goals of the fabrication. As an indicator of the resolution should be considered the distance (gap) between two antenna arms. The smallest gap (between 60 nm high arms) of about 20 nm was achieved reproducibly when the resist A4-495 PMMA (190 nm thick) was exposed by the dose of about 330 μC/cm^2. The gap between antenna arms (with length $L = 5.2$ μm) is shown in Fig. 3.1.

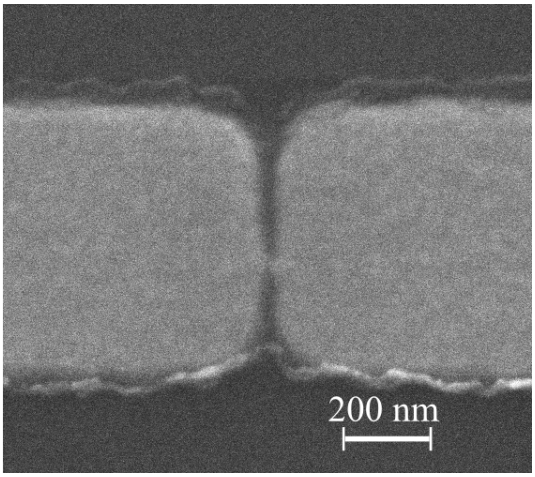

Figure 3.1: The gap of the IR plasmonic antenna (with arm length $L = 5.2$ μm). The layer-feature of the decreased contrast over the metallic parts comes from the unsolicited carbon-contamination during imaging.

To measure plasmonic resonant effects of antennas in the transmission mode by the optical microscope (Nanonics MultiView 4000) in the visible wavelength range, antennas should be fabricated on glass (quartz). Because this substrate is non-conductive, the resist should be coated by the conductive layer (Espacer 300z, Showa Denko) to avoid charging effects of the electron beam. Nevertheless, the fabrication of plasmonic resonant structures for visible wavelength range on non-conductive substrates is still difficult. The optical antennas fabricated on glass are shown in Fig. 3.2.

[4]Generally, the dose is proportional to the product of the probe current and the dwell time. Note, the dwell time denotes a time for which the beam points in the same position of the sample

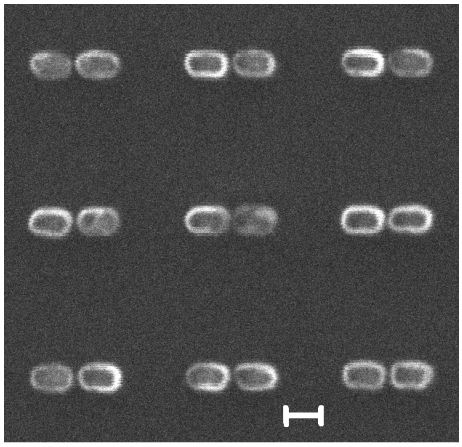

Figure 3.2: The optical antennas fabricated on glass. The antenna arm length, width and gap are about 105 nm, 70 nm and 25 nm, respectively. The bar denotes 100 nm.

Two-step lithography

The response of a plasmonic antenna can be influenced remarkably by the presence of a specific material in its vicinity. Also the study of SEIRS may demand positioning the patches (of a given material) in required positions at the antennas [127]. Therefore, the two-step lithography procedure should be used that is presented below.

The first class of structures together with some recognition features are fabricated in the first step. Afterwards, the resist A2-495 PMMA (of thickness ≈ 100 nm) is coated on fabricated structures. During the second exposition, the main problem lies in imaging and finding structures prepared in the first exposition because they are covered by the resist. To avoid the modification of the resist, the electron beam of lower landing energy (about 5-10 kV) and of a small probe current should be used during adjusting-steps.

The procedure (without any user-friendly software package) comprises following steps (also see Fig. 3.3):

a) finding the required antenna array in the sample with a help of recognition features.

b) rotation correction [5].

c) pre-focusing and positioning with the stage [6].

d) setting the appropriate magnification.

e) fine focusing on the resolution of fabrication [7].

f) defining one-antenna structure in drawing software.

g) defining and positioning a matrix of structures to be exposed.

h) checking the correct position before exposition to avoid the stage/beam drift [8].

i) exposition.

[5] It is especially necessary when finding and the exposition are performed at different landing energies of the electron beam.

[6] Focusing especially on recognition features.

[7] For that reason, extra structures (antennas) should be prepared outside the writefield in the first step.

[8] In this step, the beam-shift should be exploited to align the positions. This step is crucial.

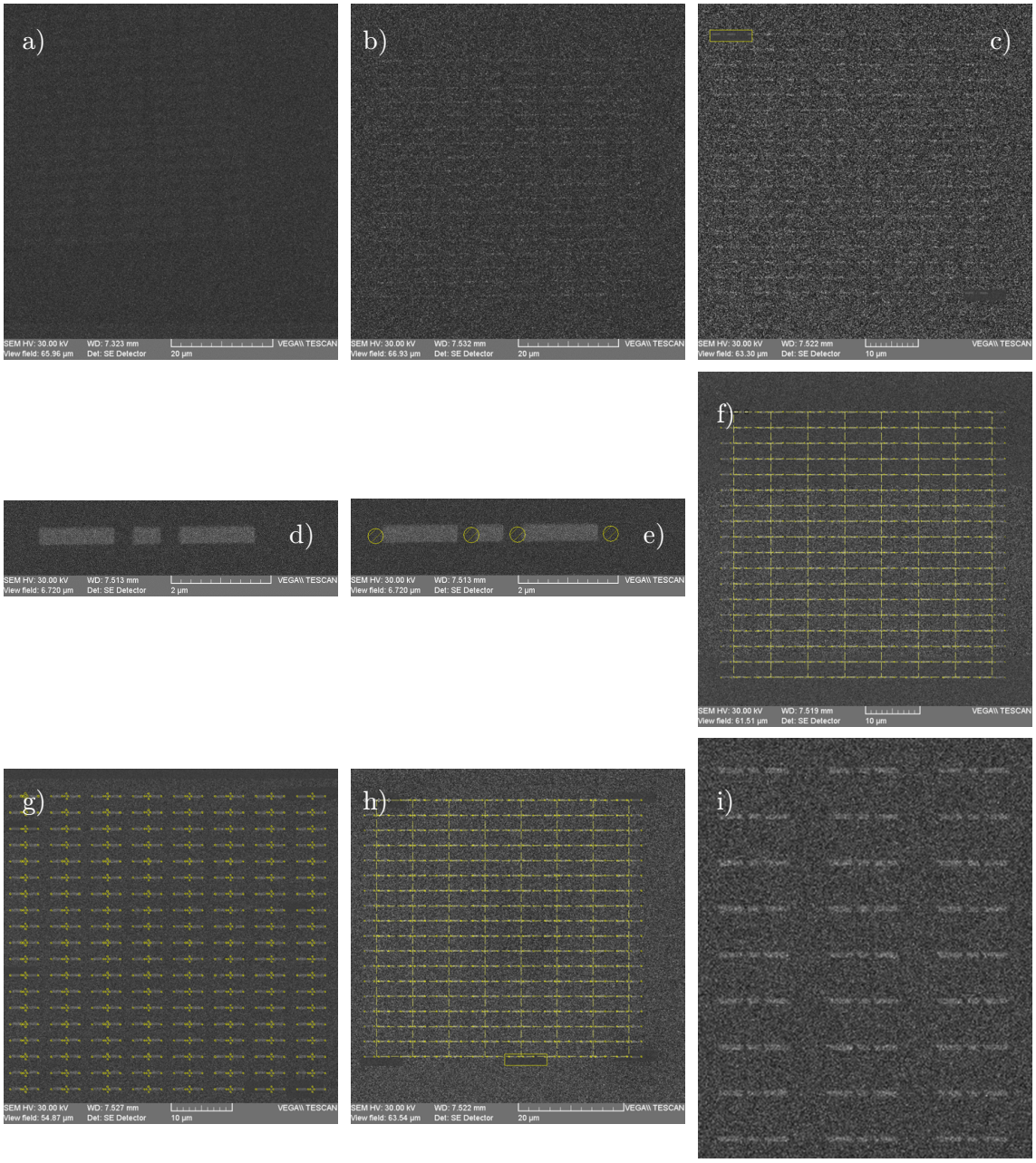

Figure 3.3: Images explaining two-step lithography: a) finding, b) rotation correction, c) pre-focusing and positioning with the stage, d) setting the magnification, e) fine focusing, f) defining a one-antenna structure, g) defining and positioning a matrix of structures, h) checking the correct position, i) exposition.

It is worth mentioning that the exposition dose should be eliminated/minimized during all steps except the exposition. The proposed procedure requires only 2 scans (for adjusting) of the whole writefield.

The resultant structures are shown in Fig. 3.4, where the rectangular and circular structures come from the first and second steps, respectively. These structures were fabricated by the electron microscope Tescan Vega - L04 having only the manual positioning of its stage. The achieved accuracy of positioning was reproducibly well below 50 nm.

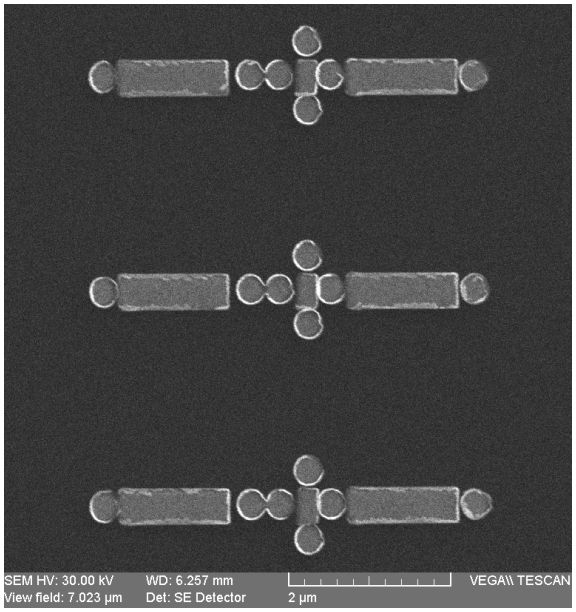

Figure 3.4: Metallic structures fabricated by two-step lithography. The rectangular and circular structures were prepared in the first and second steps, respectively. The demanding positions are evident. The achieved accuracy of positioning was below 50 nm.

3.1.2 Focused ion beam

When the emphasis is put on a resolution of substantially small plasmonic structures they are usually prepared by the focused ion beam (FIB) milling. The beam [9] probes the sample and etches an amount of its material [10]. It is worth noting these microscopes always possess also an electron column to see the prepared structures without a destruction.

In this work, the FIB technique was utilized for preparation of plasmonic antennas with resonance wavelengths below 1400 nm. These structures were prepared for a subsequent investigation by the Electron Energy Loss Spectroscopy (EELS) and Cathodoluminescence (see Section 3.5) [128]. Therefore, Si_3N_4 membrane with the area of 500x500 μm and thickness between 30-50 nm was used as a substrate. Consequently, 30 nm thick Au layer (with 3nm Ti adhesion layer) was deposited onto this membrane. The deposition was performed by the apparatus Kaufman (in IPE lab) where the sample-holder possessed the grooves to avoid a destruction of membranes by the pressure gradient during pumping of the apparatus. The images of such deposited membrane taken by electron beams of energies of 5 kV, 10 kV and 30 kV are shown in Fig. 3.5. Thus, the samples were prepared

[9] The source of gallium ions is called the liquid-metal ion source (LMIS) where the gallium-liquid is in touch with a tungsten tip. Gallium matter is wetted and consequently the ions are accelerated and traced via a column on a sample.

[10] Different technique is the focused-ion-beam-induced deposition (IBID) where the chemical vapour as a gas (precursor) is introduced in a vicinity of the specimen, it decomposes and its non-volatile components adsorb onto the specimen's surface. The chemical content (purity) of fabricated structures depends on deposited materials. For instance, platinum content of Pt deposited structures is only about 50 % [129]. For this reason, the IBID technique should be used for deposition of cobalt rather than platinum.

for etching the plasmonic antennas by the FIB.

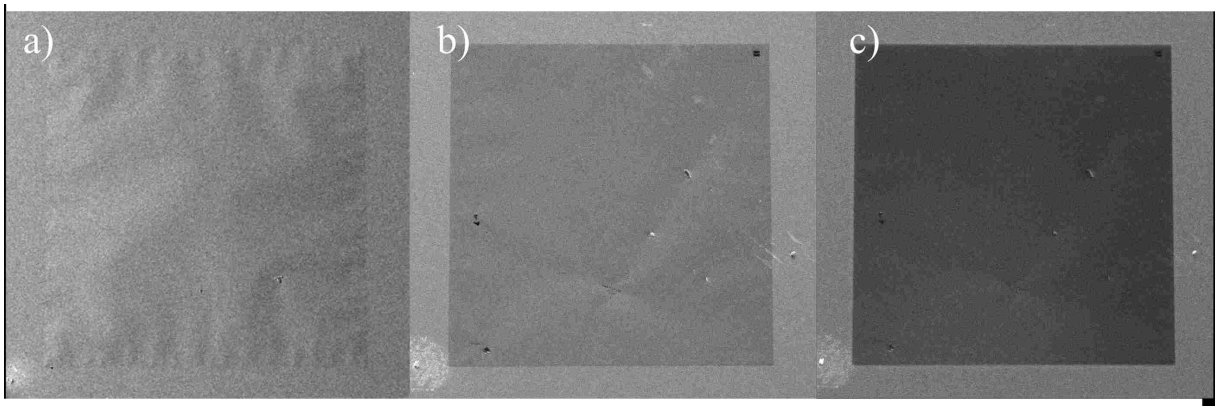

Figure 3.5: The images of the silicon nitride membrane taken by the electron microscope with beam energies of a) 5 kV, b) 10 kV and c) 30 kV.

To achieve the best resolution of prepared plasmonic structures, the probe current of the gallium beam should never exceed 1 pA. For this reason, the method becomes relatively time-consuming. On the other hand, prepared structures have not only lateral dimension well below 50 nm but also their topography is precisely shaped.

First, the ion beam is focused on chemically etched Si nanowires (see Fig. 3.6). Further steps were performed at the deposited membrane. The coincidence-alignment of the electron and ion beams are performed on contrast recognizable features of the sample.

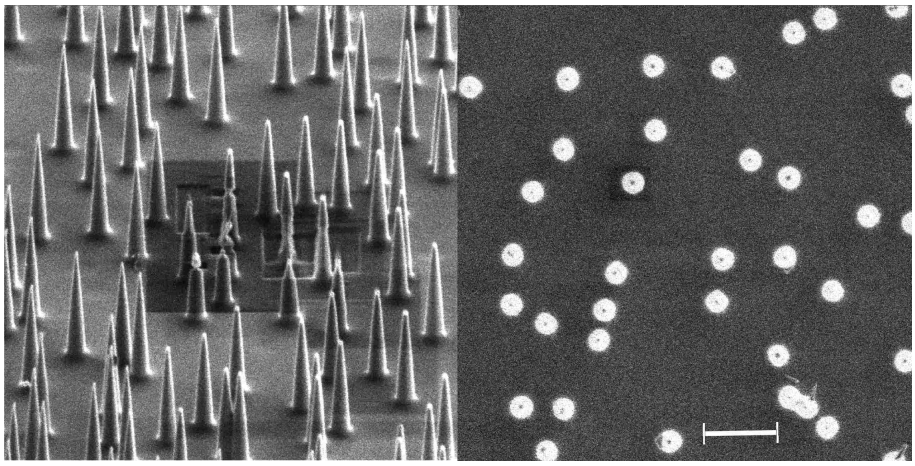

Figure 3.6: A specimen with chemically etched Si nanowires exploited for focusing the ion beam. The bar denotes 1 μm.

Afterwards, to avoid etching of the membrane (to etch only a metallic layer), the test of the etching-dose should be done. The SEM image of 11 squares etched by various doses is shown in Fig. 3.7. The appropriate dose was usually given by thickness of treated Au layers. Then, tests of etching the structures were performed via various etching-parameters as the etching depth, exposition and settle factors being usually 25 nm, 1.0 and 3.0, respectively. Finally, the geometry of prepared plasmonic structures was influenced by the grain size of given layer.

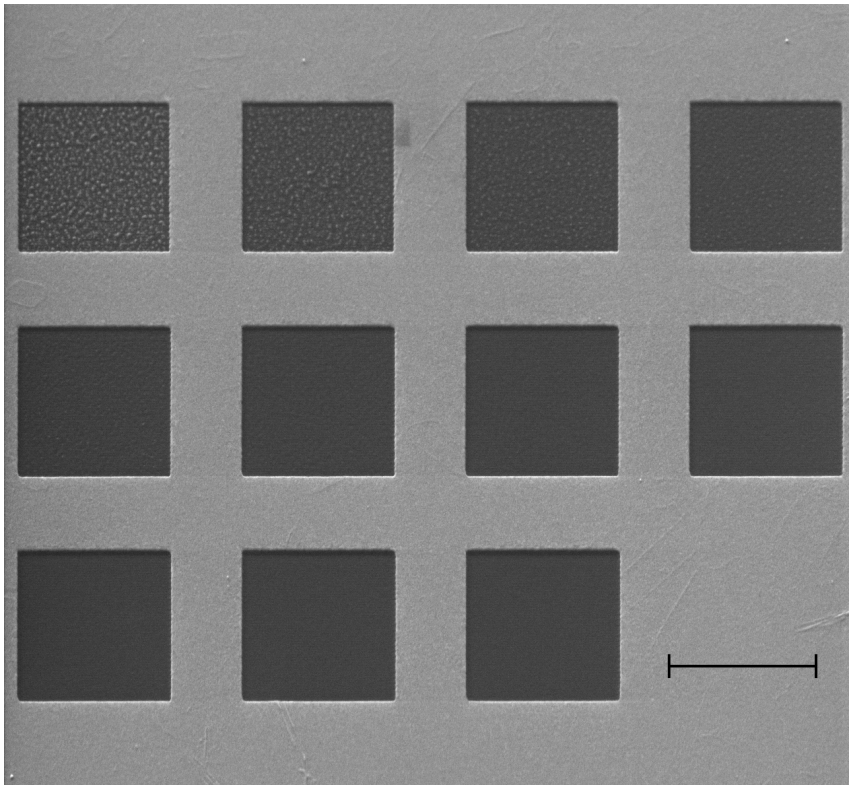

Figure 3.7: The image of squares etched during the dose-test for 30nm Au layer (with 3nm Ti adhesion layer) on Si_3N_4 membrane. The bar denotes 2 μm.

To avoid an interaction of a resonant structure with not-etched Au layer and to allow conventional optical measurements of an individual structure, a large area of layer should be etched around the structure. However, the membrane bends exceedingly as shown in Fig. 3.8. Therefore, the squares etched around plasmonic structures (for EELS measurements) had usually dimensions from 1×1 μm^2 to 2×2 μm^2.

The first plasmonic antennas were prepared to demonstrate their quality and the achievable resolution. Thus, the triangle-shaped antennas frequently studied for the strong enhancement of the electromagnetic field in hotspots at their vertexes were prepared. Also, the EELS treatment of antennas of this shape was done in literature [130]. The prepared antennas formed by triangle-dimers etched by the FIB are shown in Fig. 3.9. The length of the triangle-side of the antennas is below 75 nm. The radius of the triangle vertex goes below 20 nm and the feature in the antenna gap has a diameter below 30 nm. It is worth noting, that the resolution and dimensions of these structures are determined more by the grain-size of the metallic layer than by the resolution of the FIB.

Furthermore, plasmonic antennas of a crescent shape were extensively studied in many articles [131]. These structures were studied also at the IPE [128]. For this reason, many variants of these structures were prepared (see sketches in Fig. 3.10). As an example, dimmers of those crescents with a circle in between are shown in Fig. 3.10.

Subsequently, the cruciform-pentamer antennas were prepared. They are known for polarization-invariant strong enhancement of the near field intensity [132]. It was assigned to its high rotational symmetry. In these structures, the polarization of the incident

field cannot affect a decomposition of the scattered field into non-degenerate modes [11]. In contrast, our project has been aimed at treating those structures but missing some of their parts (see sketches in Fig. 3.11). Consequently, the field decompositions should be controlled by a disorder of the structure symmetry. This breaking of the symmetry of the electromagnetic field should be studied by EELS in detail. The structures shown in Fig. 3.12 have been prepared and are waiting for EELS measurements.

Finally, one should show a pair of complementary structures i.e. the positive and the negative (hole-like) antennas (see Fig. 3.13). Etching those structures represents a remarkable technological challenge when dimensions of both antennas should be the same. In particular, the problem lies in preparation of negative antennas where the holes should by separated from each other by tiny domains.

3.1.3 Conclusion

Despite the Electron Beam Lithography (EBL) and Focused Ion Beam (FIB) are generally known technologies, they are described with regard to fabrication of plasmonic resonant structures here. This Section is supplemented by images of structures fabricated during the work presented in Sections 3.3 and 3.4. In particular, EBL method was shown to be efficient for fabrication of not only double antennas (of dimensions of $\sim \mu$m) with the gap reaching 20 nm but also optical dimmers with arm length of about 60 nm. Moreover, the two-step lithography allowing fabrication of antennas of different metals placed close each other provides the positioning precision better than 50 nm.

The focused ion beam was used for fabrication of optical antennas with high precision of their geometry. Thus, antennas of shapes of circles, rectangles, triangles, crescents were positioned in small distances ($\sim$ 15 nm) between each other. These structures were prepared for subsequent measurements of the cathodoluminescence (reported in Section 3.5.2) and EELS. Also, the positive-like and negative-like optical antennas of complicated shape were fabricated.

[11] The near field was shown (by s-SNOM measurements) to be highly dependent on the incident field polarization with no impact on the efficiency of any excitation.

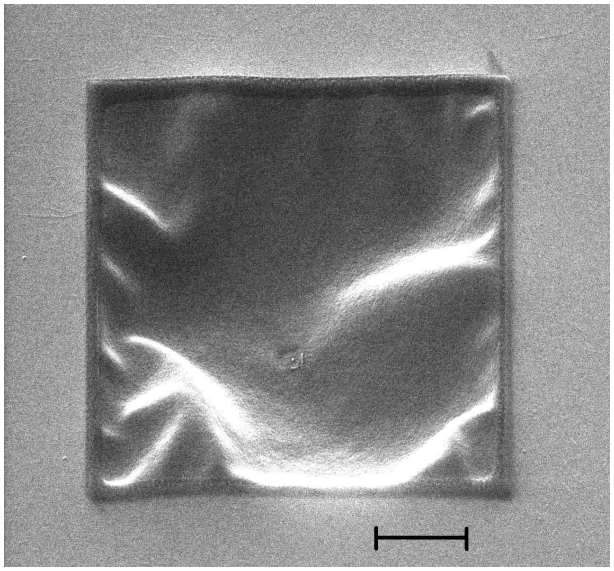

Figure 3.8: A large area of the metallic layer etched around the resonant structure leads to bending of the membrane. The layer in the close vicinity of the structure was etched by a smaller probe current (< 1 μm) than the remaining area.

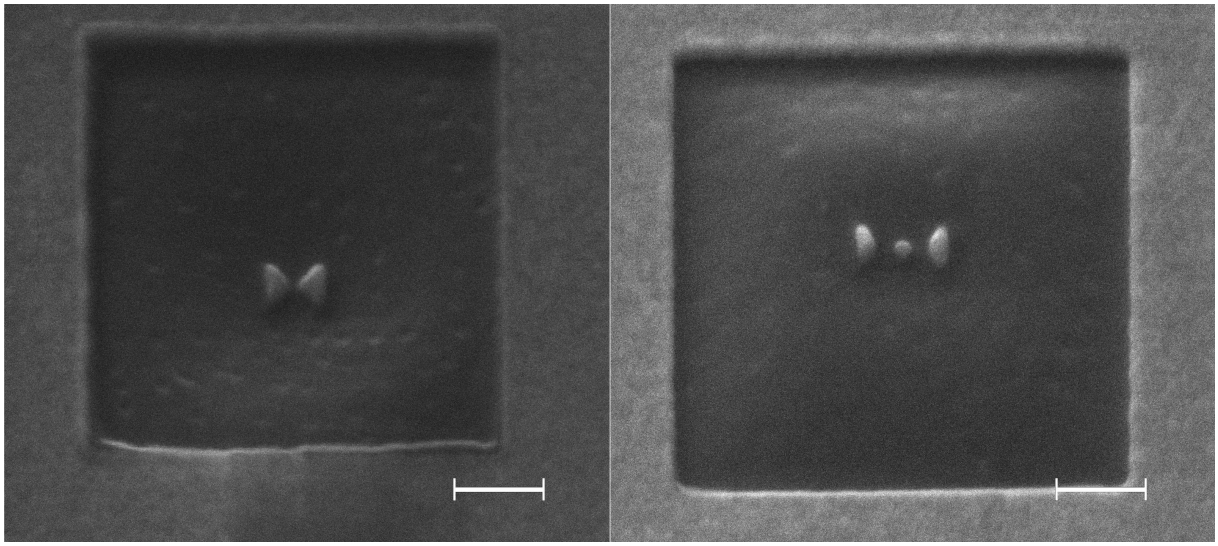

Figure 3.9: Prepared Au antennas forming triangle-dimers etched by the FIB. The length of the triangle-side of the antennas is below 75 nm. The antenna gap reaches 15 nm. The radius of the triangle vertex goes below 20 nm and the feature in the antenna gap (right image) has a diameter below 30 nm. The bar denotes 200 nm.

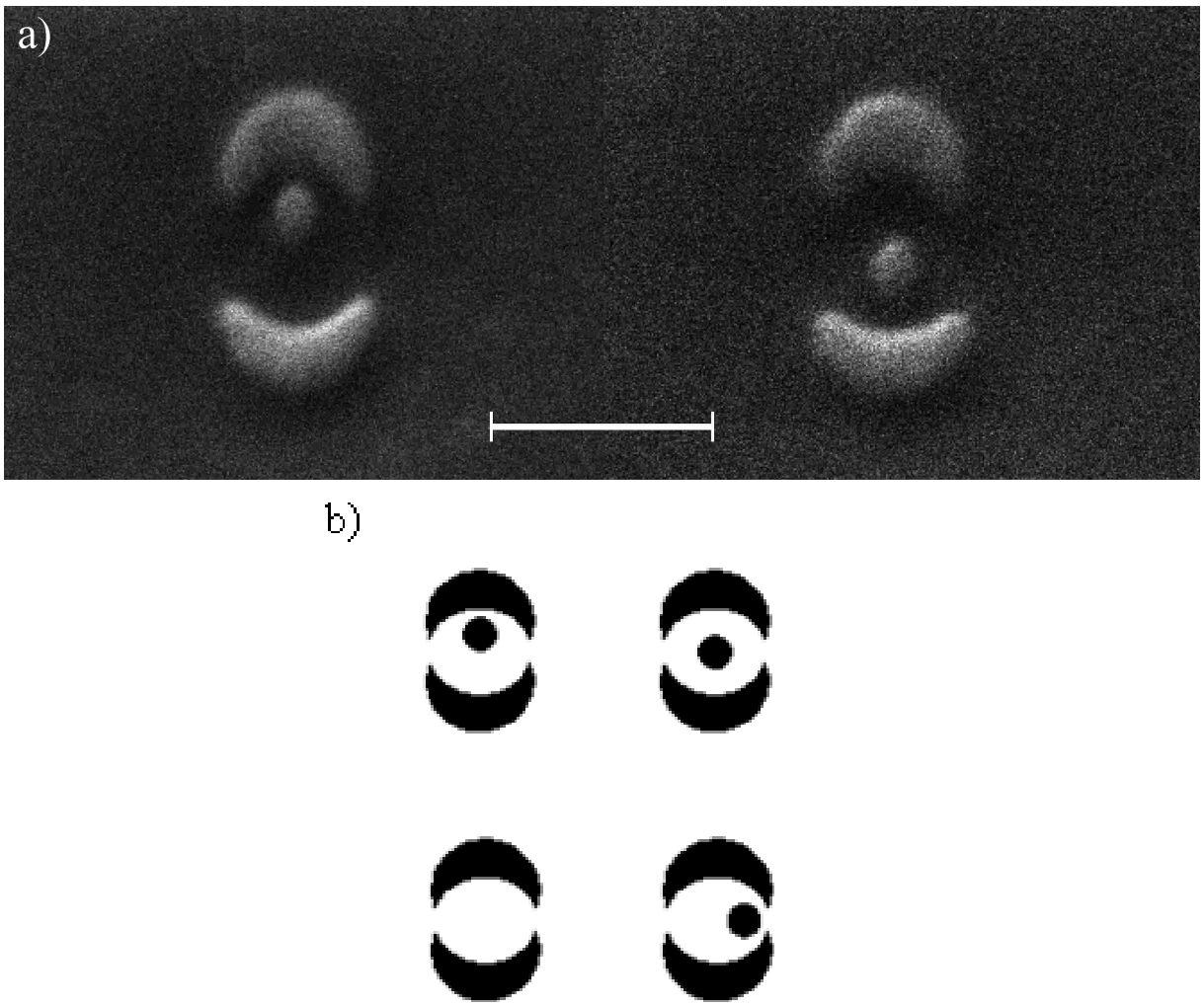

Figure 3.10: A) the dimmers of crescents with a circle in different positions. The bar denotes 200 nm. B) full series of prepared antenna in sketches.

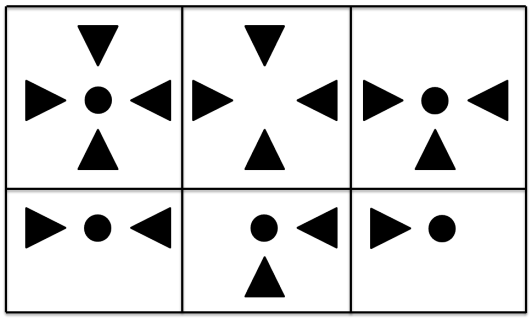

Figure 3.11: The sketches of the series of structures prepared for experiments on breaking the symmetry of the electromagnetic field. Sketches related to Fig. 3.12.

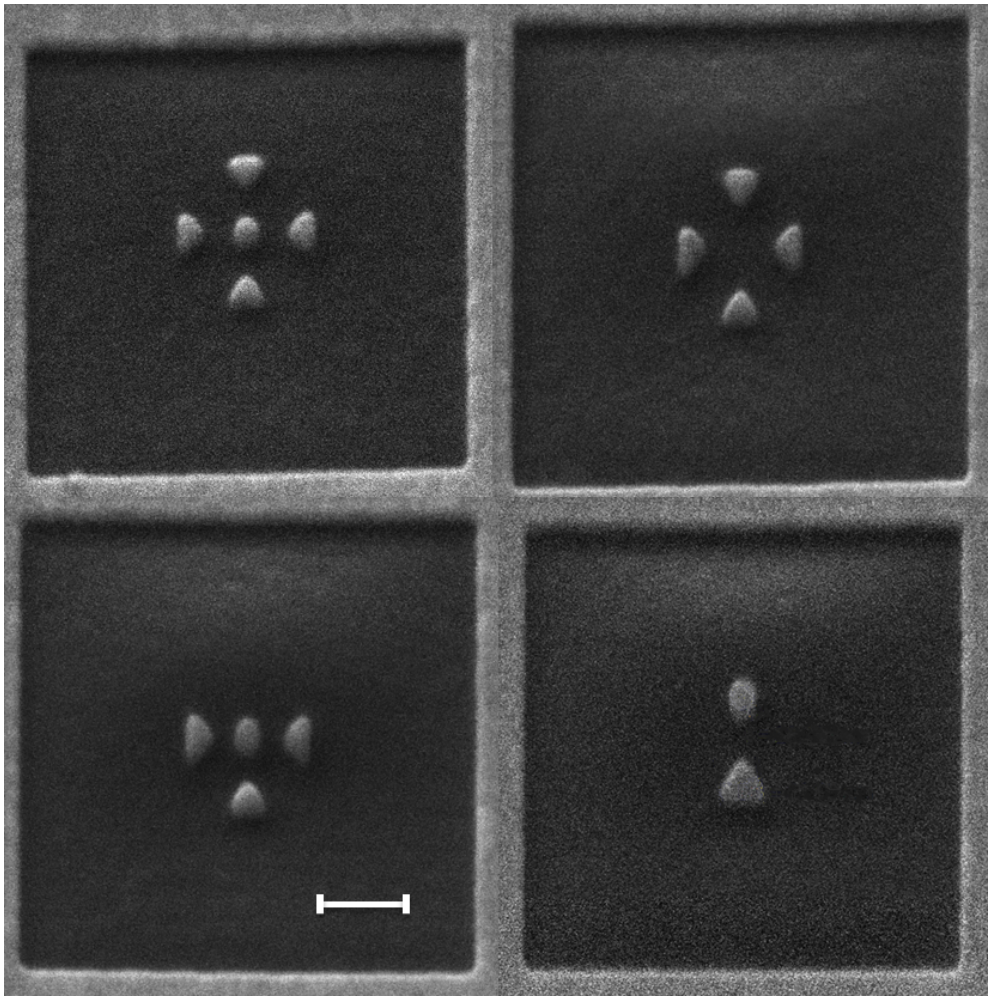

Figure 3.12: The antennas prepared for experiments on breaking the electromagnetic field symmetry. The bar denotes 200 nm.

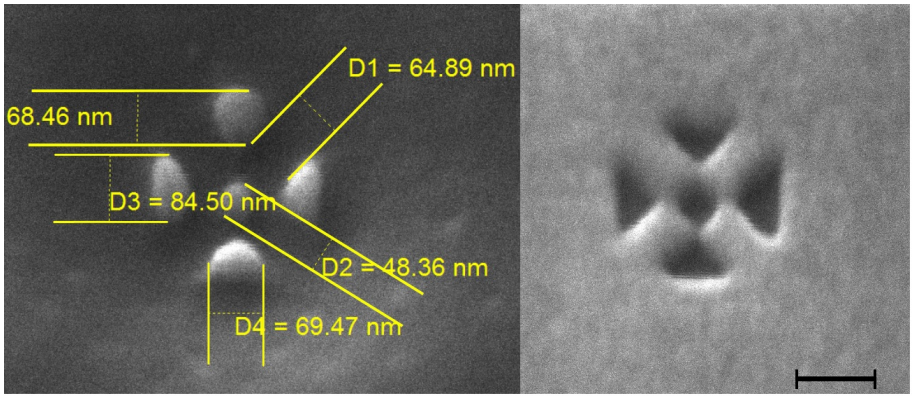

Figure 3.13: The pair of two complementary structures consisting of the positive (left) and the negative (right) antenna. The bar denotes 100 nm.

3.2 Resonances of antennas

When dealing with resonant structures the first issue is often the investigation of resonance wavelengths of plasmonic antennas. In case of antennas deposited on transparent substrates the approximative prediction is simple. In particular, the resonance wavelength λ_{res} is proportional to the antenna arm length L (dimension in the direction of polarization of the incident field) and to the effective refractive index of the of SPPs n_{eff} by the approximative relation [7], [30], [61]

$$\lambda_{\mathrm{res}} = 2n_{\mathrm{eff}}L \tag{3.1}$$

where $n_{\mathrm{eff}} = \sqrt{\frac{\varepsilon_{\mathrm{sub}}\,\varepsilon_{\mathrm{m}}}{\varepsilon_{\mathrm{sub}}+\varepsilon_{\mathrm{m}}}}$ with $\varepsilon_{\mathrm{sub}}$ and ε_{m} being dielectric functions of a substrate and a metal, respectively. In particular, $\mathtt{Re}\,[\varepsilon_{\mathrm{m}}] \ll -1$ holds for the dielectric function of a metal in infrared (see Fig. (2.5)), whereas the dielectric function of the transparent substrate is constant. Consequently, the resonance wavelength is proportional to the refractive index of a substrate [61].

It has been demonstrated that interesting phenomena occur if the antennas interact through their near fields with dielectrics possessing absorption peaks or bands at specific wavelengths. When the substrate an antenna is deposited on is non-transparent, a nonlinear dependence between resonance wavelengths and antenna arm lengths occurs. Such a situation is studied in following Section 3.3 where the antennas are deposited on a thin absorbing layer (on transparent silicon substrate, see Fig. 3.14) possessing the dispersion of its refractive index in MID-IR (particularly $\lambda \approx 8 - 12\ \mu$m). This Section is based on [62] that belongs to the first articles dealing with this behaviour [109], [110], [111], [112]. This work was motivated by an effort to exploit electromagnetic energy enhancement via platinum plasmonic antenna resonances for the phase transformation of the silicon-rich oxinitride into the nanocrystalline silicon. Afterwards, this work was extended on the sensing application in Sections 3.4 and 3.4.1.

The interaction of the resonant antenna with the absorbing material is known from a series of works dealing with intuitive models based on coupled molecular and plasmonic resonators predicting new effects such as a transition between Electromagnetically Induced Transparency (EIT) and enhanced absorption [141], or with Surface Enhanced Infrared Absorption (SEIRA) [133], Surface Enhanced Infrared Spectroscopy (SEIRS) [134], Fano-type signals in the IR extinction spectrum [110], [111], etc.

3.3 IR antennas on an absorbing substrate

This Chapter is aimed at plasmonic antennas deposited on an absorbing substrate with emphasis on resonance properties (in the far-field) and on electromagnetic field enhancement and consequent absorption increase in the near field [12].

If the metallic antennas are in a vicinity of dielectric materials having a pronounced dispersion of their dielectric function or the antennas are fabricated on substrates made out of them, the electromagnetic energy is absorbed. Consequently, the heat produces not

[12] This Chapter is based on author's publications[62], [63].

Table 3.1: Parameters of oscillators in the Lorentz model where a wavenumber reads $\nu = 1/\lambda$ [62].

$G_m\Omega_m^2$ [10^5cm^{-2}]	ω_{0m} [cm^{-1}]	λ_{0m} (μm)	γ_m [cm^{-1}]
5.35	1009	9.9	152
2.68	857	11.7	116
0.91	698	14.3	191
3.84	427	23.4	207

only in metallic antennas, but also in these materials [135], [136]. As the highest electric field enhancement generally occurs in the gaps of antennas, the maximal absorption (heat generation) in the dielectrics caused by this field is spatially localized to small volumes of these absorbing materials underneath the gaps. On the other hand, in this case the plasmonic antenna resonances themselves become significantly influenced by their coupling to absorption resonance processes in the material. The knowledge learned from the behaviour of plasmon resonance peaks in the vicinity of the absorption peaks is then utilized in optimization of a spatially localized absorption of IR radiation/heat generation in such a substrate.

In the presented work, the silicon-rich oxinitride (SRON) with the significant absorption in the mid-infrared (see Fig. (3.15)) is used as the non-transparent 110 nm thin film deposited on Si substrate (resistivity 6–9 Ωcm). The SRON film was prepared by PECVD technique at the deposition temperature of 350° C, pressure = 650 mTorr, rf power 40 W at the frequency = 13.5 MHz and the ($N_2O : SiH_4$) flow ratio equals to 6.7 $N_2O : SiH_4$.

Its refractive index was experimentally obtained by fitting the reflection by 4 Lorentz oscillators (described by parameters in Table 3.1) and $\varepsilon_\infty = 2.44$ [62]. The first oscillator (at 1009 cm^{-1}) is related to Si-O stretching mode. The second oscillator (at 857 cm^{-1}) is related to Si-N stretching mode [137], [138] [13]. The third oscillator (at 698 cm^{-1}) was assigned to neutral oxygen vacancies (described as ≡Si-Si≡) [139]. The fourth oscillator (at 427 cm^{-1}) is related to Si-O rocking mode. It is worth noting, the dielectric functions of SRON and SiO_2 were compared in Fig. 2.6.

Golden plasmonic antennas (height: 60 nm of Au on a 3nm Ti buffer layer, width: 400 nm, length: 0.8 – 6 μm) were fabricated via electron beam lithography (see Section 3.1.1, equipment: FIB/SEM Lyra3 XMH Tescan) on the SRON layer. The antennas consist of two rectangular arms (dimmer antennas) separated by a gap of 100 nm to achieve the pronounced electromagnetic field there while fabrication of a smaller gap was difficult for longer antennas. The antenna geometry is depicted in Fig. 3.14. The rectangular shape of the antenna arms was chosen to enhance energy absorption inside a larger volume beneath the gap in SRON compared to bow-tie antennas, although its radiation efficiency is smaller [90]. The antennas of the same dimensions and shape were arranged into an array of the area of 50×50 μm^2 in order to increase the reflection signal-to-noise ratio. To find a configuration with a minimized coupling between the individual resonant antennas, a series of arrays with different spacing between the antennas were designed

[13] The Si-N stretching mode may vary within range of 835-890 cm^{-1}, on the other hand, it reaches the frequency of 835 cm^{-1} known for bulk Si_3N_4 films.

and tested for the same antenna geometry.

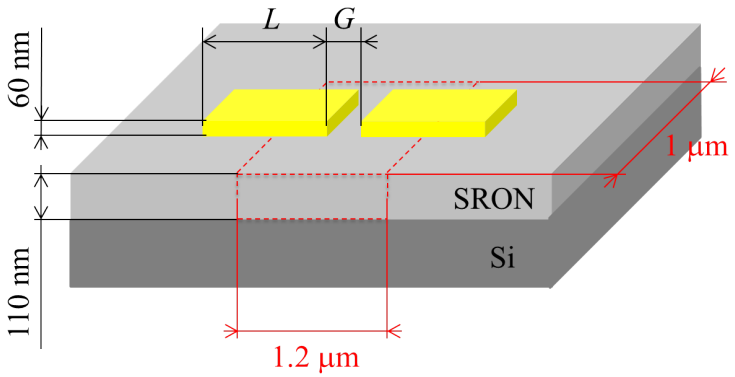

Figure 3.14: Au dimmer antenna placed on the SRON layer (110 nm thick) deposited on the Si substrate. The antenna height is 60 nm, its width is 400 nm and its length L varies from 1 μm to 6 μm. The distance between antenna arms (gap size G) is about 100 nm. The absorption enhancement is expected in the space below the antenna gap. Dimensions of the integration domain (depicted by red lines) are 1.2 μm along the main axis of antenna, 1 μm in the direction of the antenna width, and its height is 110 nm.

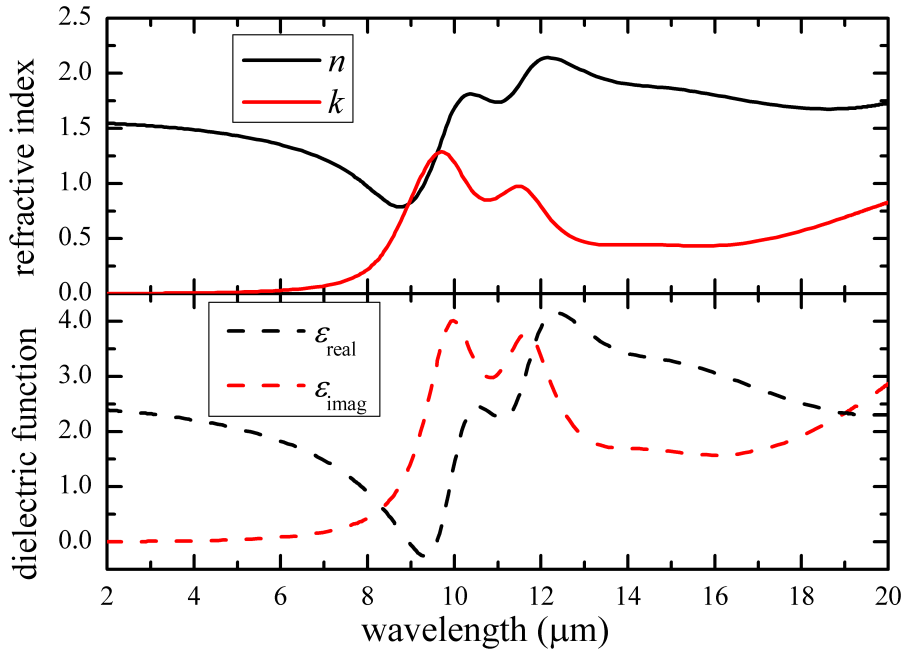

Figure 3.15: Refractive index and the dielectric function of silicon-rich oxinitride [62].

Unpolarized reflection spectra were obtained by a Fourier Transform IR microscope (FT-IR Bruker Vertex 80v + Hyperion 3000) working in the spectral range of 2 – 16.5 μm. The spectra taken from the antenna arrays were normalized to the reference ones related to the bare SRON surface nearby the antenna structures. The spectra for antennas of

various arm lengths (with the same filling by metal in every array) are plotted in Fig. 3.16. Almost each spectrum in this figure possesses two resonant peaks separated by a deep valley caused by a strong coupling of plasmonic oscillations with absorption resonances in the SRON material in the corresponding wavelength range (see Fig. 3.15), leading to overdamping of these oscillations [141]. The presence of two resonance peaks for the antenna of a specific arm length is a direct consequence of a non-monotonic character of the real part of refractive index in the range of significant absorption (resulting from the Kramers-Kronig relations) and the related increase of its values for longer wavelengths. This is obvious from an approximation Equation 3.1 [61], where n_{SRON} is the real part of the SRON index of refraction. Because of the pronounced dispersion of the SRON dielectric function around the region of enhanced absorption (Fig. 3.15) a non-linear scaling between the resonance wavelength λ_{res} and the antenna arm length L should be expected [62], citebrineknn. Indeed, looking at Fig. 3.17, where the peak positions are plotted, one can see that once the left resonance peak approaches the wavelength at which the absorption in SRON becomes substantial, it almost stops moving with increasing the antenna arm length and does not exceed the value $\lambda = 8.6$ μm. This is in agreement with the dependence depicted by the lower branch of the solid red curve in Fig. 3.17 obtained from the mentioned approximation formula. In addition, the intensity of the peak goes down and practically vanishes for the longest antenna lengths.

Accordingly, the right resonance peak is almost not moving with the small antenna arm lengths as the corresponding resonance wavelengths (12.5 μm) are too close to the area of enhanced absorption in SRON. However, this peak starts to move when the arms become bigger ($L \geq 2\mu$m) and thus the resonance wavelengths shift beyond this area.

As a consequence of the behaviour of these two peaks, two separated localized-surface-plasmon-resonance branches appear in the plot in Fig. 3.17. Similar effect has also been already observed in dispersion relation curves (reciprocal space) of SPP on a sub-wavelength hole array covered with organic molecules having an absorption peak in the visible range [140].

One can notice from Fig. 3.16 that the spectra possess a shallow drop in their intensity around $\lambda \approx 11.5$ μm which is caused by a minor increase of the absorption in SRON around this wavelength. The resonances observed for the longer wavelengths shift qualitatively with the upper branch of the red curve in Fig. 3.17 obtained from the approximation formula 3.1, where $n_{\mathrm{eff}} = n_{\mathrm{SRON}}$ [62].

The reflection spectra of the antennas were simulated by the FDTD method (Lumerical) [87] as well and the corresponding peak positions are plotted by blue line in Fig. 3.17. The good agreement between the experiment and the simulation up to $L = 4.5$ μm is obvious. For the antennas with $L > 4.5$ μm the experimental data are already weak as the quality of the peaks was very poor at the corresponding resonance wavelengths close to the upper end of the spectrometer measuring range. Contrary to the red analytical curve the numerical values of the resonance wavelength do not keep growing so intensively at the biggest arm lengths which is most likely caused by an increasing absorption in SRON at these wavelengths (see Fig. 3.15). In the inset of Fig. 3.16, the qualitatively same simulated and measured reflection spectra are shown for the antenna of $L = 3.2$ μm.

To get the information about the heat volumetric density generated by the spatially localized absorption in SRON beneath the antenna gap (upon antenna resonances), the

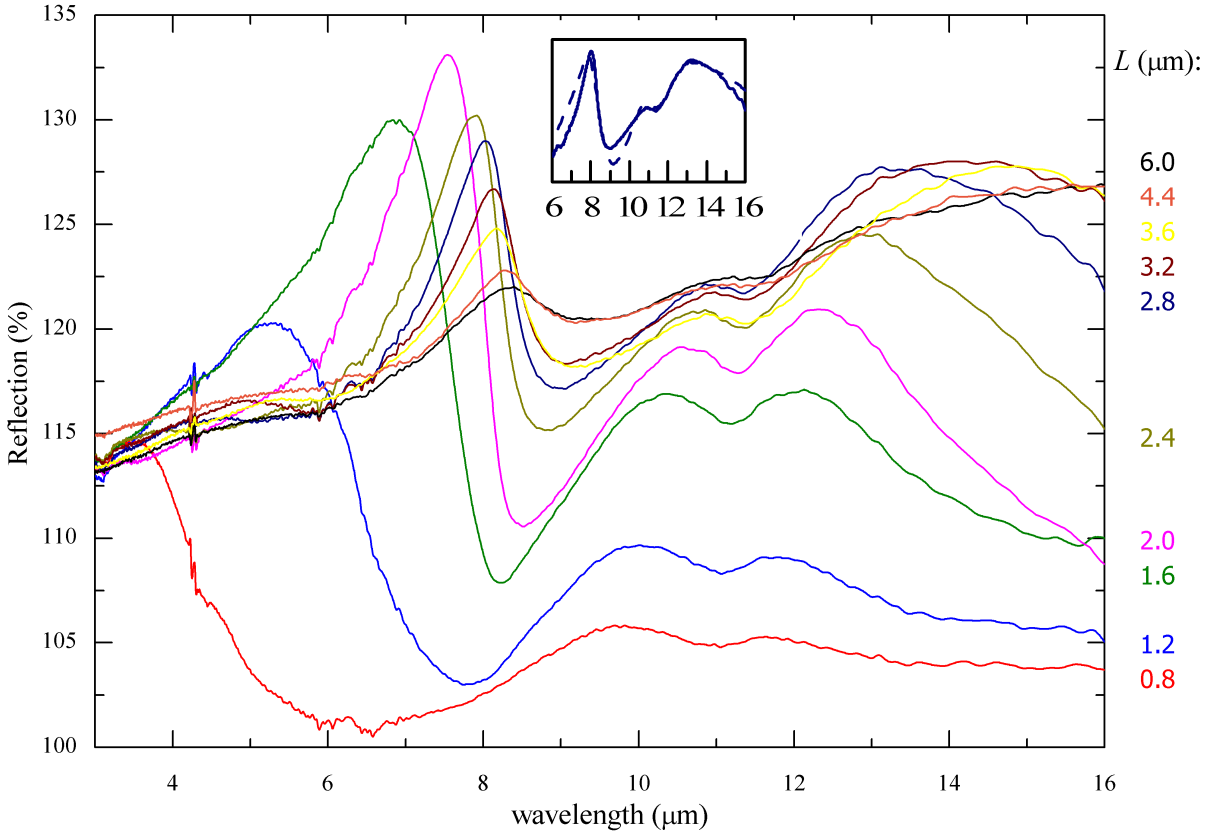

Figure 3.16: Measured IR unpolarized reflection spectra of dimmer Au antenna arrays of specified arm lengths with the gap 100 nm fabricated on a SRON/Si substrate. The coefficient of filling (by metal area) is the same for all antenna arrays. The particular lengths of antenna arms are denoted on the right side.

electric field in this volume was simulated. The heat density is determined by the formula

$$q(\mathbf{r}) = \frac{1}{2}\varepsilon_0 \omega \mathrm{Im}[\varepsilon(\mathbf{r})]|\mathbf{E}(\mathbf{r})|^2 \ , \tag{3.2}$$

where $\mathrm{Im}\,[\varepsilon(\mathbf{r})]$ is the imaginary part of the dielectric function of SRON. Supposing the constant dielectric function over the SRON film section, the heat generated in a domain of SRON beneath the antenna gap (in the domain 1.2 μm $\times$ 1 μm $\times$ 110 nm) is proportional to the square of electric field intensity ($|\mathbf{E}|^2$) integrated over this volume. Consequently, the calculated spectra of $|\mathbf{E}|^2$ values averaged over the domain are plotted in Fig. 3.18 for different arm lengths. In this 3D plot the upper and lower resonance branches are clearly visible. In the lower branch the maximal magnitude of the resonant peaks grows up and the maximum is achieved for the antenna arm length of about 2.4 μm and $\lambda = 7.8$ μm, and equals with the maximum value $|\mathbf{E}_{\mathrm{aver}}|^2 = 45$ V^{2}m^{-2}. In the upper branch the maximum reaches $|\mathbf{E}_{\mathrm{aver}}|^2 = 38$ V^{2}m^{-2} and appears for $L = 3.6$ μm and $\lambda = 17$ μm.

It is obvious that the positions of maxima are achieved as a result of a trade-off between the size of the antenna (increasing average electric intensity in the gap with the arm length for small antennas) and the material absorption in SRON (decreasing intensity). The slightly smaller maximum intensity in the upper branch compared to the

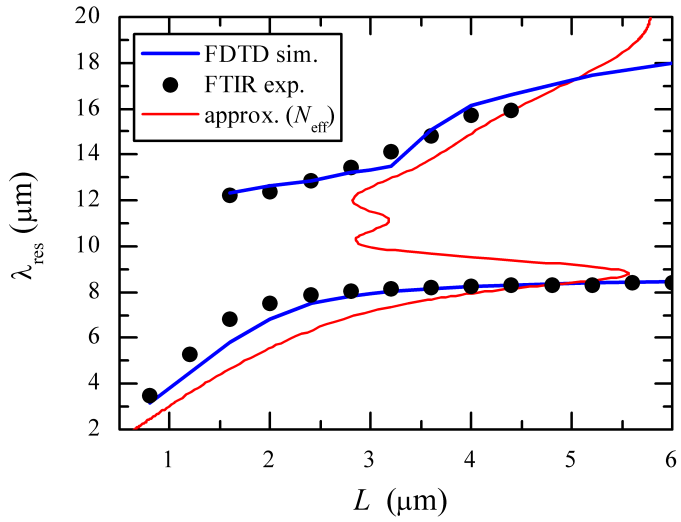

Figure 3.17: Resonance wavelengths vs. antenna arm lengths L. The resonances obtained from the reflection FTIR spectra (Fig. 3.16) are depicted by black points. The resonances obtained from FDTD numerical simulations of the reflection spectra are depicted by blue curves. The red curve is yielded by the analytical formula (3.1).

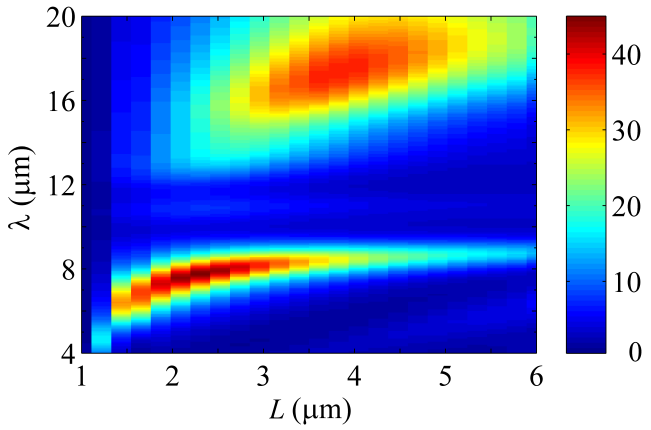

Figure 3.18: The simulated spectra of the square of the electric field ($|\mathbf{E}|^2$) averaged over a domain (with dimensions 1.2 μm $\times$ 1 μm $\times$ 110 nm) in SRON beneath the antenna gap for different antenna arm lengths specified in Fig. 3.16 and 3.17.

lower one is caused by a higher absorption of IR radiation in SRON at $\lambda = 17.3$ μm with respect to that one at $\lambda = 3.8$ μm.

In addition to the frequency, the heat generation depends on the product of the square of electric field intensity and the imaginary part of the dielectric function of SRON. Therefore, the highest spatially localized enhancement of the absorption in the SRON domain caused by plasmonic resonant effects will occur for the wavelengths already providing an increased absorption of IR radiation in SRON and still reasonable plasmonic resonances in the antennas. Hence, the maximal enhancement of the absorption in the

SRON domain caused by plasmonic resonant effects is expected in the wavelength intervals 7.8 μm $< \lambda <$ 8.5 μm and $\lambda >$ 12.5 μm where an increased absorption of IR radiation in SRON occurs together with the reasonable resonant peaks of the electric field intensity in the gap.

To find the maximal influence of antennas on enhancement of the absorption in SRON, the spectra of the relative power absorbed in the SRON domain beneath the antenna gap with respect to that one absorbed in the identical domain without the antenna (on top) was evaluated for antennas of different arm lengths (see Fig. 3.19). For the lower branch of resonances, the maximum of this relative value reached almost 60 and was achieved for the antenna of the arm length $L = 2.4$ μm and corresponding wavelength $\lambda = 7.8$ μm. For the upper branch this value was 68 and was obtained for the antenna with the arm length $L = 4$ μm and $\lambda = 17.7$ μm.

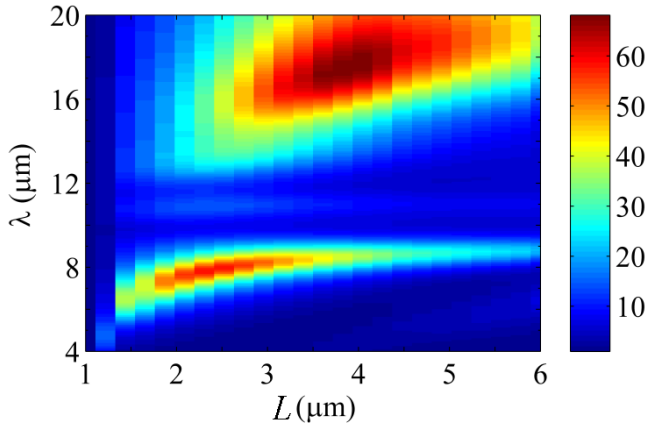

Figure 3.19: Spectra of the relative power absorbed in the SRON domain beneath the antenna gap with respect to that one absorbed in the identical domain of the sample without the antenna for different arm lengths of dimmer antennas specified in Fig. 3.16 and 3.17.

Simultaneously, the absorption efficiency defined as the ratio of the power absorbed in the SRON domain to the energy flux of IR radiation incident on the domain area was evaluated for the antennas of different lengths (see Fig. 3.20). In the lower branch of resonances, the maximal absorption efficiency reaches a value of 0.86 and occurs for the antenna arm length of 3.2 μm ($\lambda = 8.6$ μm). The maximal absorption calculated in the same SRON domain of the sample without the antenna (bare substrate) was 0.068 and occurred for $\lambda = 9.9$ μm. Hence, the absorption efficiency was enhanced by the plasmonic antennas almost by the factor of 12.6. In the upper branch of resonances, the absorption efficiency of the domain beneath the gap reached the value 1.28 for the antenna arm length of 4.4 μm (about $\lambda = 20$ μm) which represents the enhancement by the factor 19 with respect to the bare SRON.

The relation between the absorption efficiency (see Fig. 3.20) and the square of electric field intensity (see Fig. 3.18) averaged over a domain beneath the antenna gap in SRON layer is depicted in Fig. 3.21. The horizontal axis represent the wavelengths of maximal absorption efficiency or maximal averaged electric field intensity for different antenna arm lengths. The figure shows the interplay between the pronounced dispersion of the

SRON dielectric function and the electromagnetic resonances of the metallic antenna arms resulting in the red shift between wavelengths for the absorption efficiency related to the maximal averaged electric field intensity.

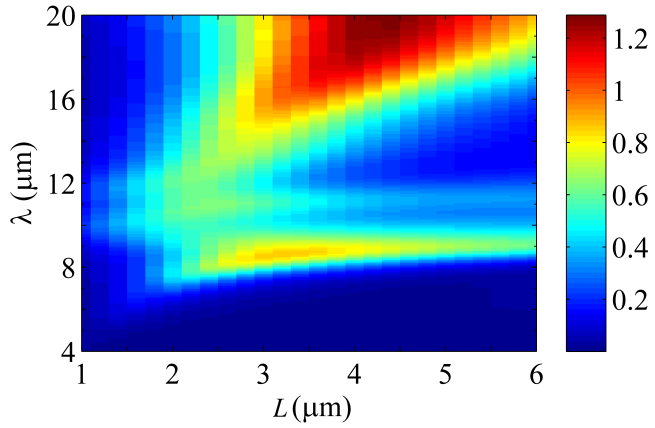

Figure 3.20: Absorption efficiency of the SRON domain beneath the antenna gap for different arm lengths of dimmer antennas specified in Fig. 3.16 and 3.17.

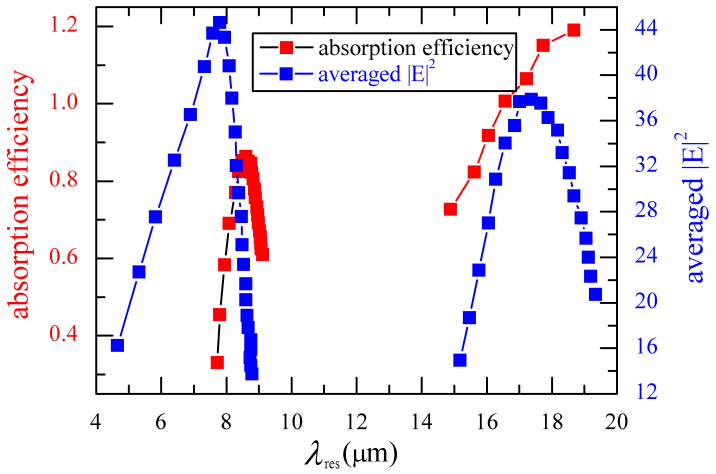

Figure 3.21: Calculated absorption efficiency and averaged electric field intensity ($|\mathbf{E}^2|$) at resonance wavelengths of different antenna arm lengths.

Finally, to get an overall idea about heat generation by plasmonic processes in the antenna set-up, the FDTD numerical simulations of the heat formed in the metallic antenna arms has been carried out as well. It was found that the heat power developed in the antenna arm increases with its length until it reaches its maximum for $L = 2.4$ μm ($\lambda = 7.43$ μm). After that, it starts to decrease steeply. On the other hand, the absorption efficiency (defined as the ratio of the heat power developed in the antenna arm to the energy flux of IR radiation incident on the arm) continuously decreases (from a maximum value of 1.4 for $L = 1$ μm) with the antenna arm length as shown in Fig. 3.22.

Consequently, taking into account the results presented above, there is a chance that at longer wavelengths corresponding to the maximum absorption in SRON beneath the

antenna gap the heat developed in this part might be significantly higher than in the antenna arms. Hence, the heating of SRON by the arms would be less significant when the heat in SRON just beneath the antenna gap becomes maximal. The results in Fig. 3.23 indicate such a spatially localized heat development. In particular, the heat power density distribution (horizontally) across the arms $L = 1$ μm and $L = 4.4$ μm and over SRON beneath the antenna gap is depicted for wavelengths $\lambda = 4$ μm and $\lambda = 20$ μm, respectively.

Although the fabricated SRON layer possesses the thickness about 110 nm, supplement calculations of the absorption in the SRON film of different thickness have been done and they are plotted in Fig. 3.24. The resonance wavelengths of structures with thinner layers shift towards longer wavelengths because Si substrate has greater refractive index than the SRON layer.

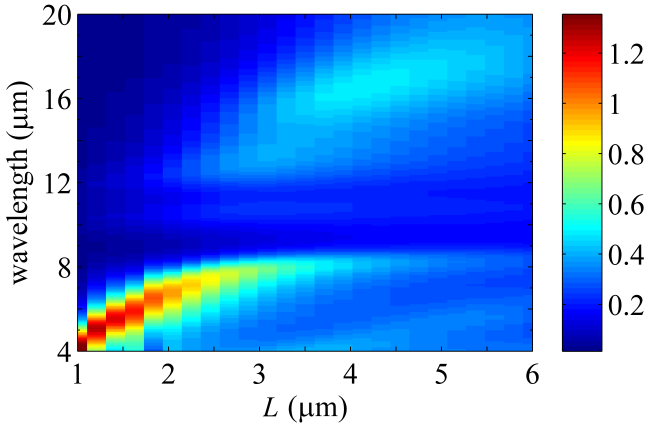

Figure 3.22: Absorption efficiency of the antenna arm for the antennas of different arm lengths specified in Fig. 3.16 and 3.17.

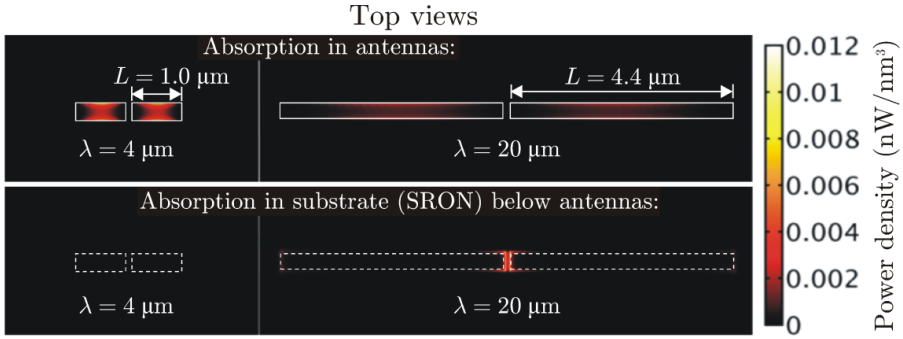

Figure 3.23: Computed heat power density distribution [nW/nm^3] across the horizontal cross sections in the middle of height of the arms (upper picture) and in the SRON layer 5 nm below the surface (lower picture). The antennas of the length $L = 1$ μm (left) and $L = 4.4$ μm (right) were illuminated by the radiation with the intensity 480 W/cm^2 and wavelengths $\lambda = 4$ μm and $\lambda = 20$ μm, respectively.

The discussions on the behaviour of plasmonic resonances of antennas fabricated on the

absorbing substrate and their utilization for spatially localized absorption enhancement of electromagnetic radiation (especially heat generation) in this substrate have been carried out for the mid-IR. However, the conclusions are also applicable for other spectral regions where the materials exhibit a strong absorption resonances (for instance in the visible). The absorption enhancement and efficiency in this region should be even more profound due to correspondingly higher frequencies.

In the following section, the attention will be paid to the interplay between the antenna resonances and the material absorption of various strengths (see Equation 2.49).

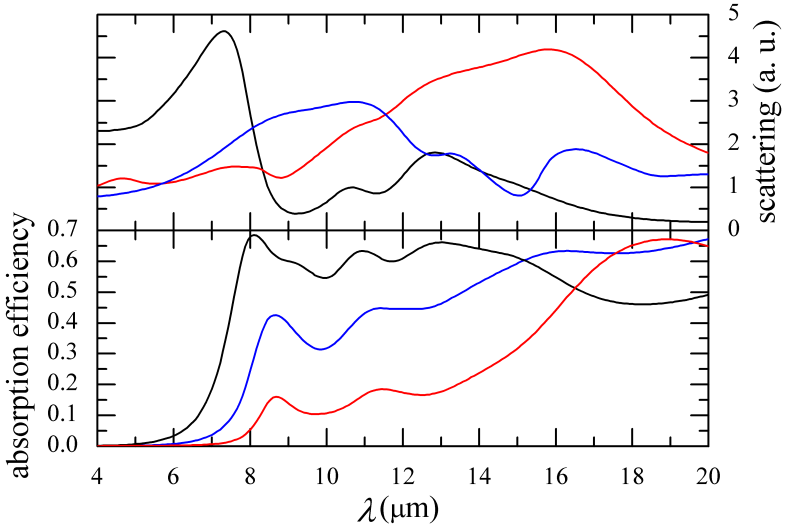

Figure 3.24: The mutual relation between simulated total scattering of the electromagnetic field (on left) and the absorption efficiency (on right) of the domain below the gap of the antenna with $L = 2.4$ μm placed on the SRON layer. Spectra for the layer thicknesses of 10 nm, 50 nm, 100 nm were denoted by red, blue and black curves, respectively.

Conclusions

Resonance properties of the plasmonic infrared antennas deposited on the SRON layer with a significant absorption of radiation in the mid-infrared were studied. Almost each far-field reflection spectrum obtained for an antenna of a specific length generally possesses two resonant plasmonic peaks being separated by a valley resulting from a strong coupling of plasmonic oscillations with absorption resonances in the SRON material. Because of the pronounced dispersion of the SRON dielectric function caused by the enhanced absorption of IR radiation in this material, a nonlinear scaling between the resonance wavelength and the antenna arm length was observed for these peaks, both experimentally and theoretically. Therefore, both the lower and upper plasmonic resonance branches reveal significant deviations from linear behaviour. The heat generation primarily depends on the product of the square of electric field intensity and the imaginary part of the dielectric function of SRON. Hence, the highest plasmonic enhancement of spatially localized absorption in this material will occur for the wavelengths already providing an increased absorption of IR radiation in SRON and still having reasonable plasmonic resonances in the antennas. Therefore, for each plasmonic resonant branch the maximum relative values of the

absorption enhancement and absorption efficiency (both related to bare SRON without antennas) in the domain below the gap occur at a wavelength in the interval between the wavelength corresponding to the maximal electric field intensity and that one where the plasmonic oscillations start to be strongly damped. For the lower branch these maxima worth 60 and 13 were found by numerical simulations at the wavelengths $\lambda = 7.9$ μm and $\lambda = 8.6$ μm, respectively. For the upper branch these values were 68 and 19 and the corresponding wavelengths $\lambda = 17.8$ μm and $\lambda = 20$ μm, respectively.

3.4 IR antennas on an annealed substrate

In the previous Section 3.3, it was shown that an antenna resonance wavelength is modified remarkably when it approaches a region of the absorption of a surrounding material. The resonance properties of antennas on the absorbing substrate (SRON) discussed in Section 3.3 are studied in more detail here. Namely, the resonance properties of antennas deposited on SRON annealed at different temperatures (and thus having different absorption peak strengths) are investigated. This investigation of the interplay between plasmonic resonances and (adjustable) resonances in surrounding material can provide supplementary information for sensing application [141], [142].

First, the material changes of SRON during annealing itself are discussed in Section 3.4, and subsequently the resonance properties of antennas deposited on annealed SRON layers are presented in Section 3.4.

Annealed SRON

SRON can be considered as a multi-phase material composed of a mixture of stoichiometric silicon dioxide (SiO_2), off-stoichiometric oxide (SiO_x, with $x < 2$), elemental silicon, nitrogen and hydrogen [143], [144]. Consequently, SRON shows a pronounced dispersion of its refractive index (and absorption peaks) in infrared [14]. Mutual ratios of bond contents in SRON and the corresponding Lorentz oscillator strengths are tunable by annealing temperatures [143], [144], [145]. Off-stoichiometric oxide and silicon excess are separated into Si nanoclusters (crystalline or amorphous depending on their size), defects (oxidation states) and SiO_2 after the thermal treatment above temperatures of 1000 °C [146], [147], [148].

From the point of view of material changes, this Section 3.4 is focused on plasmonic sensing of material transformation/modification in SRON occurred by annealing [15]. Furthermore, SRON represents a good material for investigation of the plasmonic enhancement of vibrational modes of surrounding material called Surface-Enhanced Infrared Spectroscopy (SEIRS) studied in the following Section 3.4.1.

The specimens identical to the ones studied in Section 3.3 were annealed at temperatures of 1150 °C and 1200 °C. Their dielectric functions were obtained by J. Humlíček via fitting the reflection by 3 Lorentz oscillators with $\varepsilon_0 = 2.1$ (see Section 2.4.2) [16]. In par-

[14] The structures in the dielectric function of SRON can be tuned by preparation procedures [144].

[15] The results are discussed with respect to photoluminescence measurements performed on bare specimens (without the antennas).

[16] The results were confirmed by measurements of the ellipsometry performed by A. Dubroka.

Table 3.2: Parameters of Lorentz oscillators of fitted reflection of SRON annealed at 1150 °C, where the wavenumber reads $\nu = 1/\lambda$.

$G_m\Omega_m^2$ [10^5cm^{-2}]	ω_{0m} [cm^{-1}]	$\lambda_{0m}(\mu$m)	γ_m [cm^{-1}]
4.70	1066	9.4	88
8.62	939	10.6	222
4.06	442	22.6	131

Table 3.3: Parameters of Lorentz oscillators of fitted reflection of SRON annealed at 1200 °C, where the wavenumber reads $\nu = 1/\lambda$.

$G_m\Omega_m^2$ [10^5cm^{-2}]	ω_{0m} [cm^{-1}]	$\lambda_{0m}(\mu$m)	γ_m [cm^{-1}]
11.1	1078	9.3	71
9.04	919	10.9	252
4.88	452	22.1	88

ticular, the oscillators of specimens annealed at temperatures of 1150 °C and 1200 °C are described by parameters in Tables 3.2 and 3.3, respectively.

The oscillators in Tables 3.1, 3.2 and 3.3 can be associated with particular bonds in SRON although it is difficult for its amorphous nature. The first oscillator (at 1066 cm^{-1} and 1078 cm^{-1} for T_{anneal} = 1150 °C and T_{anneal} = 1200 °C) is associated with the stretching mode of Si-O bond. Its frequency moves towards higher energies by annealing and approaches the frequency of 1074 cm^{-1} of a bulk SiO_2 [139]. The second oscillator (at 939 cm^{-1} and 919 cm^{-1} for $T_{\text{anneal}} = 1150$ °C and $T_{\text{anneal}} = 1200$ °C) is associated with Si-O bond [149]. The third oscillator (at 442 cm^{-1} and 452 cm^{-1} for $T_{\text{anneal}} = 1150$ °C and $T_{\text{anneal}} = 1200$ °C) is associated with rocking mode of Si-O bond [150].

The material (and its material phase) changes with annealing that can be observed by a disappearance of the second and third oscillator present in not-annealed SRON. The second oscillator (at 857 cm^{-1}) associated with the stretching mode of Si-N bond [150] disappears as SRON changes from Si_3N_4-like to SiO_2 nature by annealing. Similarly, its third oscillator (at 698 cm^{-1}) associated with neutral oxygen vacancies [139] disappears because its content reduces during annealing resulting in a greater signal from Si-nanoclusters in photoluminescence (see Fig. 3.25).

The dielectric functions of not-annealed and annealed SRON are plotted together in Fig. 3.26. Within the wavelength range of about 8–12.5 μm dielectric functions possess dispersion that is more remarkable for higher annealing temperatures. In particular, SRON has the Reststrahlen band (with possible excitation of surface phonon polaritons) as it obtains properties of SiO_2 by annealing. The quality factors of the first Lorentz oscillators for annealed SRON are two times higher than that one of not-annealed SRON. Moreover, the oscillator strength for the substrate annealed at 1200 °C is two times higher than for the others (compare Tab. 3.1, 3.2 with Tab. 3.3). Moreover, the dispersion in the wavelength range of about 20–26 μm increases from not-annealed to annealed substrate. The vibration signal in infrared can be enhanced via plasmonic antenna resonance that represents the aim of the next part of this Section 3.4.

Apart from features in IR spectra [144], annealed SRON exhibits also the photoluminescence (PL) activity [151]. The PL peak intensity and its wavelength provide the

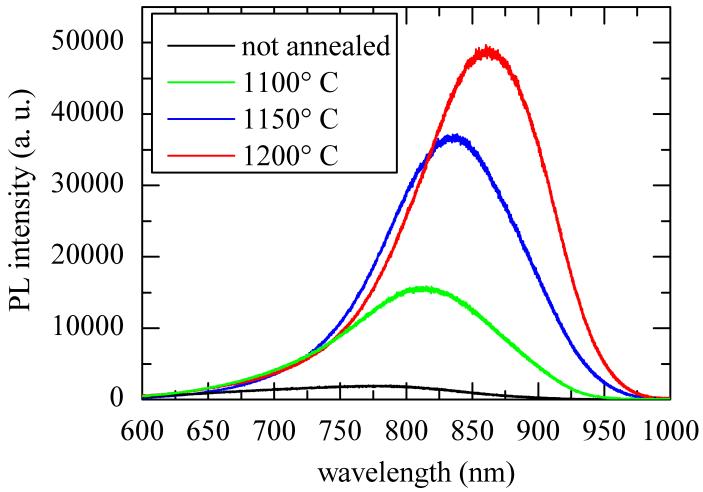

Figure 3.25: PL spectra of not annealed and annealed SRON specimen. The photoluminescence spectra were provided by Zoltán Édes.

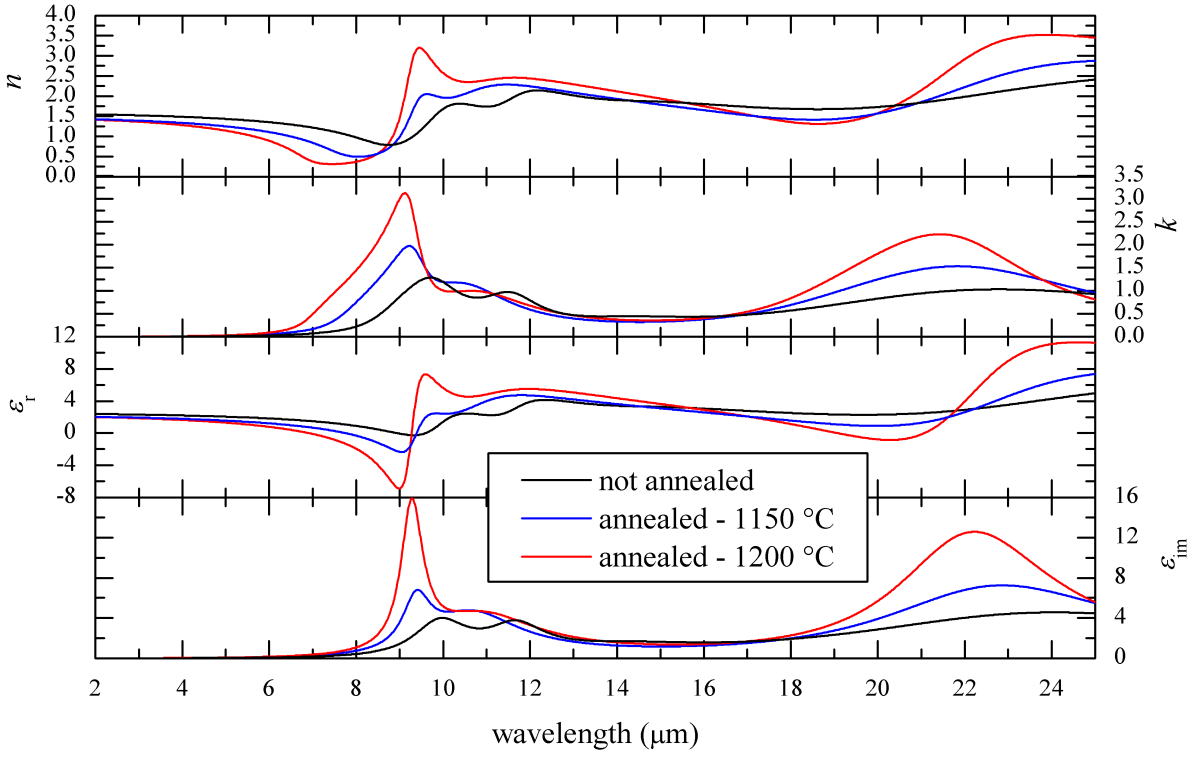

Figure 3.26: Refractive index and dielectric function of SRON layers not-annealed and annealed at temperatures 1150 °C and 1200 °C depicted by black, blue and red curves, respectively.

information about the presence of Si nanocrystals in a specimen and thus the degree of annealing. The photoluminescence measurements were performed by Zoltán Édes. The photoluminescence spectra of not-annealed specimen and ones annealed at different temperatures are plotted in Fig. 3.25. The photoluminescence spectra of annealed

SRON (at temperatures of 1100° C, 1150° C, 1200° C) possess peaks (at about 810 nm, 835 nm, 860 nm) associated with the luminescence of Si-nanocrystals [152], [153]. The peak positions are red-shifted as the Si-nanocrystals increase in size with the annealing temperature.

Antenna resonances

The motivation behind is to compare responses of the plasmonic antenna to materials (in its vicinity) having different strengths of absorption peaks. This knowledge can be demanded in sensing applications like SEIRS [112], etc.

This work lies in a comparison of resonances of antennas deposited on SRON layers annealed at different temperatures and thus having different absorption strengths. To perform this properly, identical arrays of Au antennas have been fabricated by EBL (see Section 3.1.1) on these specimens. It is worth mentioning fabricated antennas on different specimens should possess almost same dimensions (and geometry). This was managed by a spacer-layer (see Section 3.1.1) coated on annealed samples below the resist compensating its different adhesion on annealed samples.

Unpolarized reflection spectra were measured by FTIR method on antenna arrays consisted of the same number of antennas [17]. The particular spectra taken from samples not-annealed and annealed at temperatures of 1150 °C and 1200 °C are shown in Fig. 3.27 a), b) and c), respectively.

The stronger dispersion of dielectric functions (see Fig. 3.26) of annealed layers results in a deeper dip in reflection spectra (compare Fig. 3.27 a) with b) and c)) for wavelengths between 7.8–12.5 μm as SRON obtains optical properties similar to SiO_2. The most remarkable dip is observed for the substrate annealed at 1200 °C that may be related to the overdamping of the system [141] associated with higher quality factor and strength of the first Lorentz oscillator of SRON (see Tab. 3.3). Also, spectra of specimens annealed at 1200 °C possess peaks remarkably sharp and close to ω_{LO} of SiO_2 (see Fig. 2.6). This behaviour is in agreement with results measured in transmission in [112].

Moreover, one can pay attention to features within the wavelength range of 7.8 μm $< \lambda <$ 9.9 μm corresponding to the Reststrahlen band of annealed SRON (see Fig. 3.27 b), c)). These features are enhanced only weakly by short antennas possessing plasmonic resonances far below this region. In contrast, they are remarkably enhanced by longer antennas with resonances in this region.

Summarizing, a peak in the region of 7.8 μm $< \lambda <$ 9.9 μm and a dip at $\lambda \sim 12.5$ μm becomes more remarkable on annealed specimens. Therefore, it results in a step in the dependence between resonance wavelengths and antenna arm lengths for annealed SRON in Fig. 3.28.

Relations between resonance wavelengths and antenna arm lengths are plotted for not-annealed and annealed substrates in Fig. 3.28. Resonances on annealed layers are blue-shifted in lower and upper branches of resonances. This behaviour was confirmed also by the FDTD simulations. In particular, the lower branch of resonances is blue-shifted by presence of stretching mode of Si-O-Si bond. On the other hand, the blue-shift of the upper branch of resonances is determined by the rocking mode of Si-O bond (at about 450 cm^{-1}).

[17] Analogously to Section 3.3, the reflection spectra acquired from areas with antennas were normalized to reference (bare) spectra without antennas.

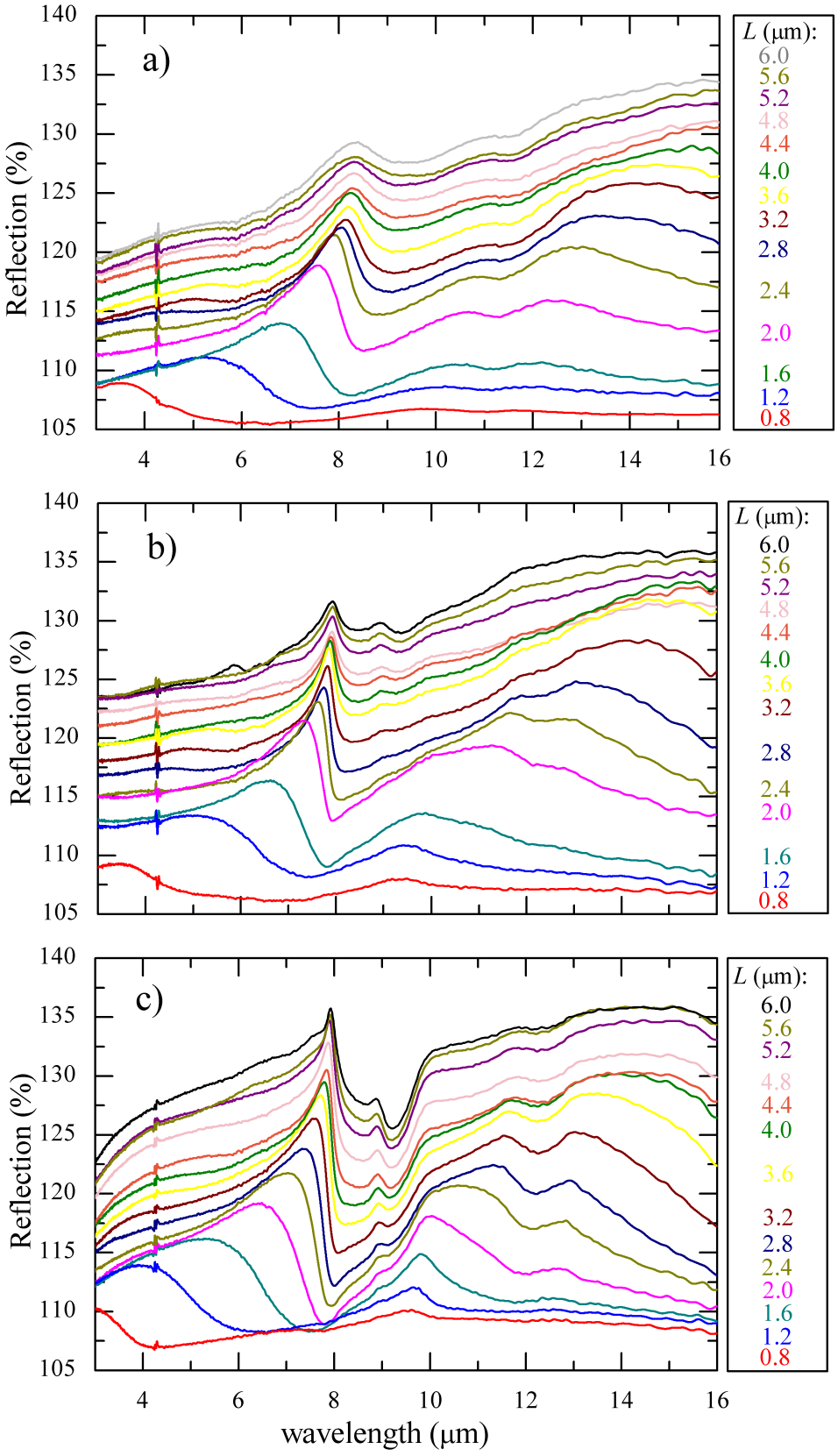

Figure 3.27: Measured IR unpolarized reflection spectra of dimmer Au antenna (of the gap size of 100 nm) arrays fabricated on a) not-annealed sample, and annealed samples at temperatures b) of 1150 °C and c) of 1200 °C. The particular lengths of antenna arms are denoted on the right side.

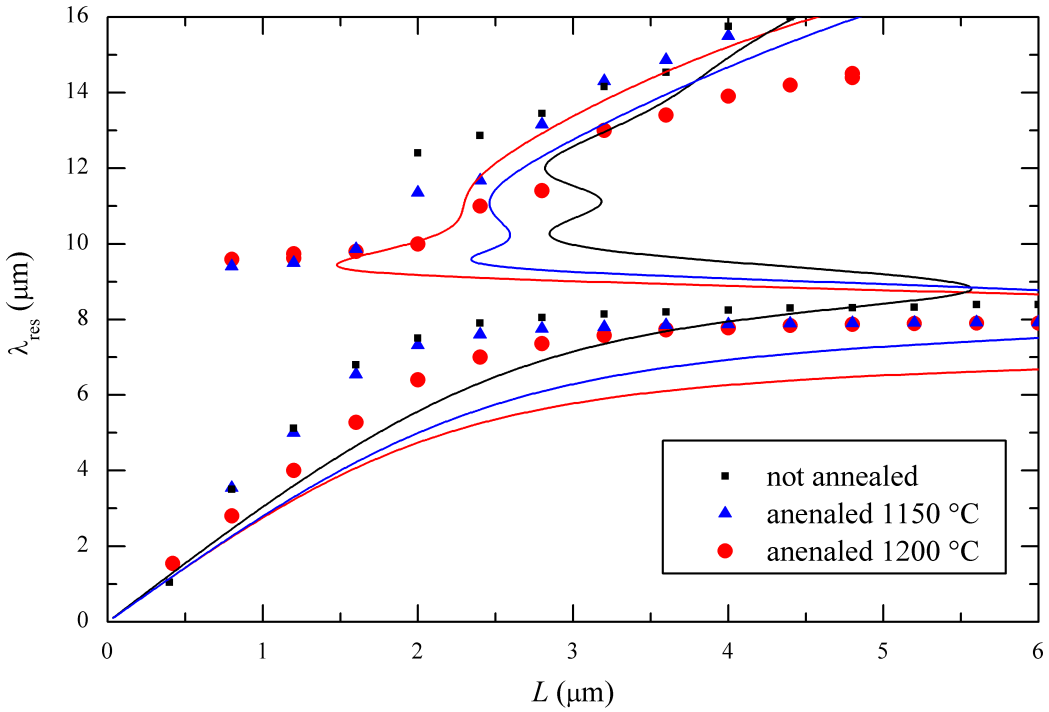

Figure 3.28: Resonance wavelengths vs. antenna arm lengths L. Experimental data and approximative relations (by Equation 3.1) depicted by dots and curves, respectively.

3.4.1 Surface-enhanced infrared spectroscopy on SRON

The plasmonic resonance of an antenna is capable to enhance the vibrational modes of a material in its vicinity. As mentioned above, it is exploited in the Surface-Enhanced Infrared Spectroscopy (SEIRS). Materials with optical properties fitted only by single oscillator were studied by SEIRS in [110], [111], [112]. The "plasmonic" enhancement of a vibrational signal has been represented by the ratio of the height to Full Width at Half Maximum (FWHM) of given spectral features [112].

The SEIRS behaviour can be found also in reflection spectra of antennas on SRON layers (Fig. 3.27). However, its investigation is more difficult because SRON dielectric function is fitted by 3 or 4 (overlapping) Lorentz oscillators. To approach SEIRS investigation of this material, spectral features enhanced in different wavelength ranges are dealt with independently.

For the lower branch of resonances, the hight-to-FWHM ratios of peaks in reflection of antennas deposited on not-annealed and annealed SRON are shown in Fig. 3.29. One should pay attention to not-annealed SRON studied in Section 3.3. There, the maximal hight-to-FWHM ratio occurs for the antenna arm length of $L = 2.8$ μm that lies between arm lengths of $L = 2.4$ μm and of $L = 3.2$ μm providing maximal electromagnetic field enhancement in metallic arms (proportional to the electric field in SRON domain denoted in Fig. 3.18) and the absorption efficiency (see Fig. 3.20) in the SRON layer, respectively. Therefore, the plasmonic antenna resonance is determined by a dielectric function of the surrounding material in its close vicinity where the near field ($\mathbf{E}^2$) is enhanced.

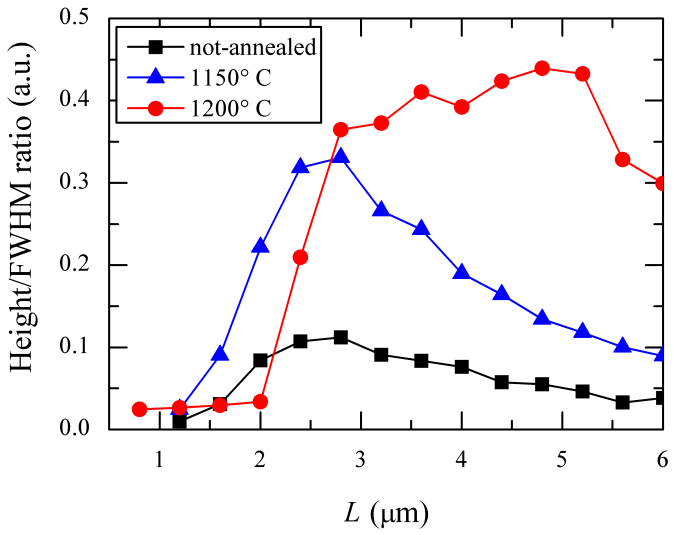

Figure 3.29: The height-to-FWHM ratios of the features in the lower branch of resonances for different arm lengths. The dependences are plotted for not annealed and annealed SRON layers at temperatures of 1150 °C and 1200 °C.

In the upper branch of resonances, the investigation of SEIRS is more difficult because the material resonances of SRON overlap noticeably. The height-to-FWHM ratios of the features are shown for different antenna arm lengths in Fig. 3.30. There are two peaks for annealed specimens and only one peak for not-annealed SRON. The vibrational peaks enhanced via antennas of about $L = 3.2$ μm correspond to resonance wavelengths

of 14.1 μm, 14.3 μm and 12.9 μm for not-annealed and annealed SRON at temperatures of 1150 °C and 1200 °C, respectively. Moreover, spectra of annealed SRON possess peaks enhanced by antennas of $L = 1.6$ μm corresponding to wavelengths of about 9.7 μm. Before concluding, one should mention a dip in spectra of SRON annealed at 1200 °C. This dip is remarkably enhanced by antennas of $L = 2.8$ μm with correspondent wavelengths of $\sim \lambda = 12.3$ μm [18].

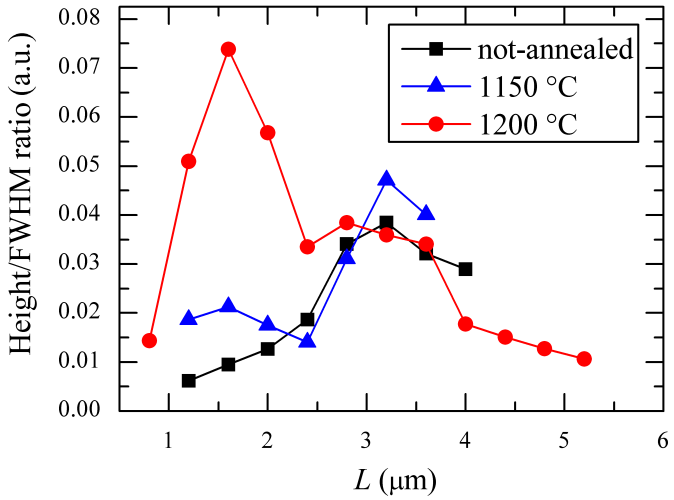

Figure 3.30: The height-to-FWHM ratios of the features in the upper branch of resonances for different arm lengths. The dependences are plotted for not annealed and annealed SRON layers at temperatures of 1150 °C and 1200 °C.

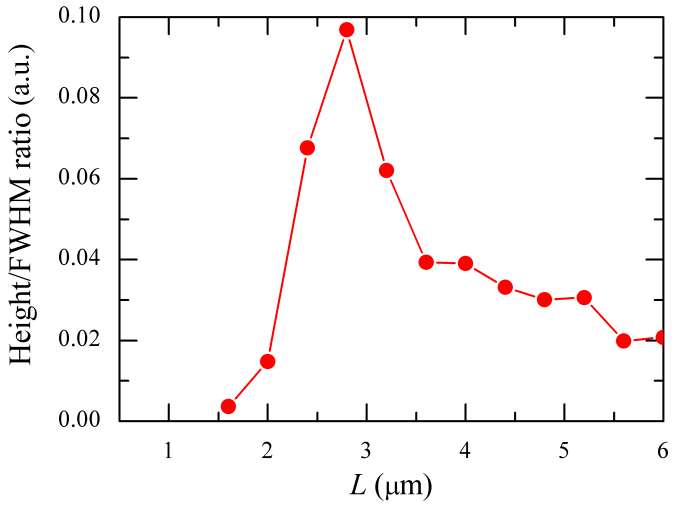

Figure 3.31: The height-to-FWHM ratios of the dip in the upper branch of resonances for different arm lengths. The dependence is plotted for SRON layer annealed at temperature of 1200 °C.

[18] The dip about wavelengths of $\sim \lambda = 12.3$ μm is also weakly observed on SRON annealed at 1150 °C.

As antennas on SRON annealed at 1200 °C exhibit the most substantial features one can compare their SEIRS spectra for the upper branch of resonances (Fig. 3.30 and 3.31). Features at wavelengths of about 9.7 μm are enhanced properly by antennas of $L = 1.6$ μm. Going to longer wavelengths, the dip at wavelengths of about $\lambda = 12.3$ μm is properly enhanced by antennas $L = 2.8$ μm while the broad peak is enhanced (only slightly) by the antenna of $L = 3.2$ μm. Summarizing, despite SRON possesses more vibrational modes/peaks, it is possible to find an antenna arm length that enhances the vibrational signal of a given mode properly. More skilful techniques as fitting the reflection spectra or dealing with quality factors of material resonances (its Lorentz oscillators) have not provided deeper insight yet.

3.4.2 Conclusions

To conclude, the ability of the plasmonic antenna to enhance a vibrational signal of its substrate (called SEIRS) was studied and confirmed for SRON possessing 3-4 material resonances. It was shown that the coupling between the plasmonic resonance and the material oscillations results in not only splitting of the plasmonic resonance (due to the increased absorption of the surrounding material referred in Section 3.3) but also a remarkable excitation of surface phonon polaritons. Moreover, it was found that despite the material possesses more material resonances (described by overlapping Lorentz oscillators), it is possible to find the antenna arm length enhancing the vibrational signal of a given material resonance.

3.5 VIS antennas excited by an electron beam

The previous Sections were aimed at resonance properties of structures excited via a conventional light source. Resonances caused by this homogeneous volumetric illumination have been discussed in review articles e.g. [23], [25], [154]. Nevertheless, sensing by plasmonic structures represents the good motivation for finding plasmonic modes possessing narrow-wavelength spectral responses [132], [155], [156] or for mapping the photonic local density of states (LDOS) [128], [157], [158]. For this purpose, different types of excitations should be used. In particular, the local excitation in the form of an electron beam impinging onto a plasmonic structure is studied intensively nowadays [157], [159], [160]. Therefore, this topic is discussed in this section.

The electron beam impinging onto plasmonic structures represents an inhomogeneous, local excitation that can excite modes different from ones excited via light sources [160]. Moreover, different modes should be excited when the electron beam impinges onto different positions of the structure [160], [161], [162]. Hence, this method represents a further supplement to the far-field optical investigation of resonant plasmonic modes [163].

Accelerated electrons are used in many applications including the observation of specimen's topography (SEM) or its chemical characterization. The interaction of electrons (accelerated to keV) with the matter produces different measurable signals as secondary electrons, backscattered electrons and photons called the cathodoluminescence. Also, the impinging electron may suffer the energy-loss that can be measured via the electron energy-loss spectroscopy (EELS) on thin specimens [164]. It is worth mentioning SPPs were observed by the energy-loss already in 1957 [9], [10].

The cathodoluminescence (CL) is a process occurring either incoherently or coherently. In the classical conception of the incoherent cathodoluminescence, the emission of the photon is a consequent effect of an electron-hole pair annihilation (especially in semiconductors) that is generated by the collision of impinging electron beam with the matter. On the other hand, the coherent cathodoluminescence involves Cherenkov radiation and transition radiations. Both radiations can be described by the Maxwell equations. The Cherenkov radiation occurs when a charged particle passes through a homogeneous medium with greater speed than the phase velocity of light in the given medium [165]. The Cherenkov radiation is marginal in metals so it is not discussed in this text. The transition radiation occurs when a probing electron passes the interface between two media of different permittivity. This phenomenon was predicted and experimentally confirmed in [166], [167], respectively. For the electron beam energy of 30 keV, the emission probability of light (in the visible) is remarkably smaller for the transition radiation than for the excitation of SPPs/LSPs [168]. The interference of the transition radiation with SPPs/LSPs was studied in SPPs interference structures in [168]. However, the impact of the transition radiation on experiments related to plasmonics is usually not taken into account.

The excitation of surface or localized plasmons by an electron beam can be fully understood within the framework of classical electrodynamics. The passing electron generates the electromagnetic field described by the Lienard-Wiechert potential [48]. When the electron beam impinges metallic structures its field excites collective oscillations of free

electrons in metal (i.e. SPPs), giving rise to an induced electromagnetic field [169]. In this concept, the energy of the impinging electrons is transferred into the energy of induced plasmons and then ultimately dissipated in the form of heat and radiation. This induced field acts back on the passing electrons, changing both their energy and momentum.

Consequently, the force exerted by the total electric field of induced SPPs acts back on the impinging electron. This electron reduces its velocity that can be expressed by the energy-loss [157]

$$\Delta E = e \int \mathbf{v} \cdot \mathbf{E}_{\mathrm{ind}}(\mathbf{r}_e(t), t)\ \mathrm{d}t \tag{3.3}$$

where $\mathbf{E}_{\mathrm{ind}}(\mathbf{r}_e(t), t)$ denotes the induced electric field on the trajectory $\mathbf{r}_e(t)$ of the impinging electron with the charge e and velocity $\mathbf{v}$. This energy-loss can be measured by the scanning transmission electron microscopes (STEM) equipped with the monochromator (EELS). Note, the EELS in STEM requires almost electron-transparent specimens. Therefore, plasmonic structures to be measured by EELS are usually fabricated on thin ($\sim$ 30 nm) membranes of silicon nitride (Si_3N_4). The fabrication of nanostructures for EELS measurements was one of the goals of this work referred in Section 3.1.2.

The EELS is able to capture both near- and far-field components. The comparison between EELS and the photonic local density of states (LDOS) has been performed in [160] where no direct connection/link between EELS and LDOS maps has been found on plasmonic antennas [19].

A part of the induced electromagnetic field in the form of radiation can be detected as the cathodoluminescence signal [170], [171]. Thus, plasmonic peaks in the cathodoluminescence represent only radiative modes of measured structures. Measurements of the cathodoluminescence can be performed on arbitrarily thick specimens, because the signal is collected from the space above the specimen.

In summary, the cathodoluminescence and EELS in a scanning mode can provide SPP spectra with deeply subwavelength spatial resolution. It was shown in literature, that these spectra are dependent both on the antenna geometry and on the position impinged by the beam onto [128]. Thus, both techniques can provide snapshots of fields of plasmonic modes supported by nanostructures. This section is aimed at simulations and measurements of the cathodoluminescence.

3.5.1 Simulations of cathodoluminescence

To investigate numerically the radiative modes excited by the impinging electron beam, the beam was modelled as a line current-density source. In the FDTD simulation approach where the movement of a passing electron cannot be simulated directly, the current density (due to a passing charge) can be modelled as a series of dipoles with temporal phase delay that is governed by electron velocity [170] [20]. The dielectric functions of gold and substrates were obtained from [50] and [72], respectively. The induced radiated power is obtained by integrating the Poynting vector over the area localized 100 nm above the antenna.

[19] They observed also a case when the EELS method was blind to hot-spots in the antenna gap.

[20] Note, this technique provides only approximative approach [160].

3.5.2 Measurements of cathodoluminescence

Experimental setup

The experimental device is basically a SEM microscope equipped with a system for detection of the weak light signal radiated from the specimen. In particular, the measurements presented in this work were performed by FEI Quanta FEG with MonoCL4 apparatus (Fig. 3.32).

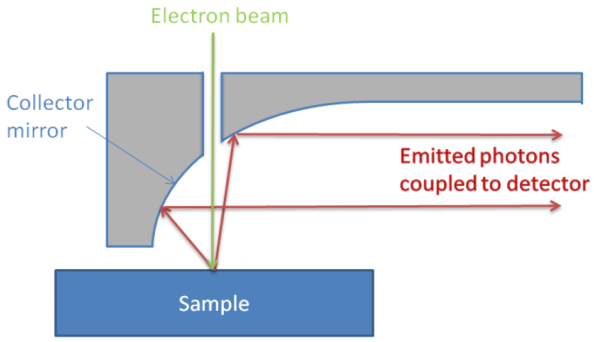

Figure 3.32: FEI Quanta FEG with MonoCL4 apparatus for measurements of cathodoluminescence.

The electron beam of the probe current 10-50 nA accelerated by 30 kV had the spot diameter of about 5 nm. The working distance (distance between the objective and the specimen) was about 11.5 mm. It is worth mentioning that due to a very poor CL signal excited by plasmonic resonance the working distance was always adjusted with precision $\sim$ 0.1 mm with respect to the maximal collected signal. The apparatus collecting the emitted (CL) light was then placed between the specimen and the SEM objective. It comprises a parabolic aluminium mirror with a small pinhole for an impinging electron beam. Then, the light was guided onto the entrance slit of a Czerny-Turner monochromator with CCD array detector. The spectral range of the detection was 400–750 nm that consequently reduced the scope of the experiments. The monochromator allowed two operating modes. In the panchromatic mode, the signal of all frequencies was collected; in contrast, the monochromatic mode was able to provide cathodoluminescence spectra.

In the first phase of experiments, some reference measurements have been performed on specimens of CL-active materials (e.g. quartz specimen, GaN) to confirm the reliability of the technique. The acquisition time was usually about 2 minutes for a whole wavelength range. The maximal cathodoluminescence signal was measured on quartz. Its spectrum consists of 60 000 counts per each 10nm wide wavelength interval. The spectra measured on reference specimens were comparable to ones from literature, thus the experiments with excitations of SPPs began.

Regarding experiments with plasmonic structures providing weak signal intensity, the obtained spectra were always normalized to the reference ones from bare substrates (including a dark-signal).

Firstly, SPPs were excited on Au layers. The SEM image and corresponding CL image

of metallic strip (40 nm heigh, width 5 μm) taken in the panchromatic mode are shown in Fig. 3.33. The CL spectrum obtained from the layer edge is shown Fig. 3.33. The spectrum possesses the peak at about 600 nm provided by the vertical resonance at the edge ([172]).

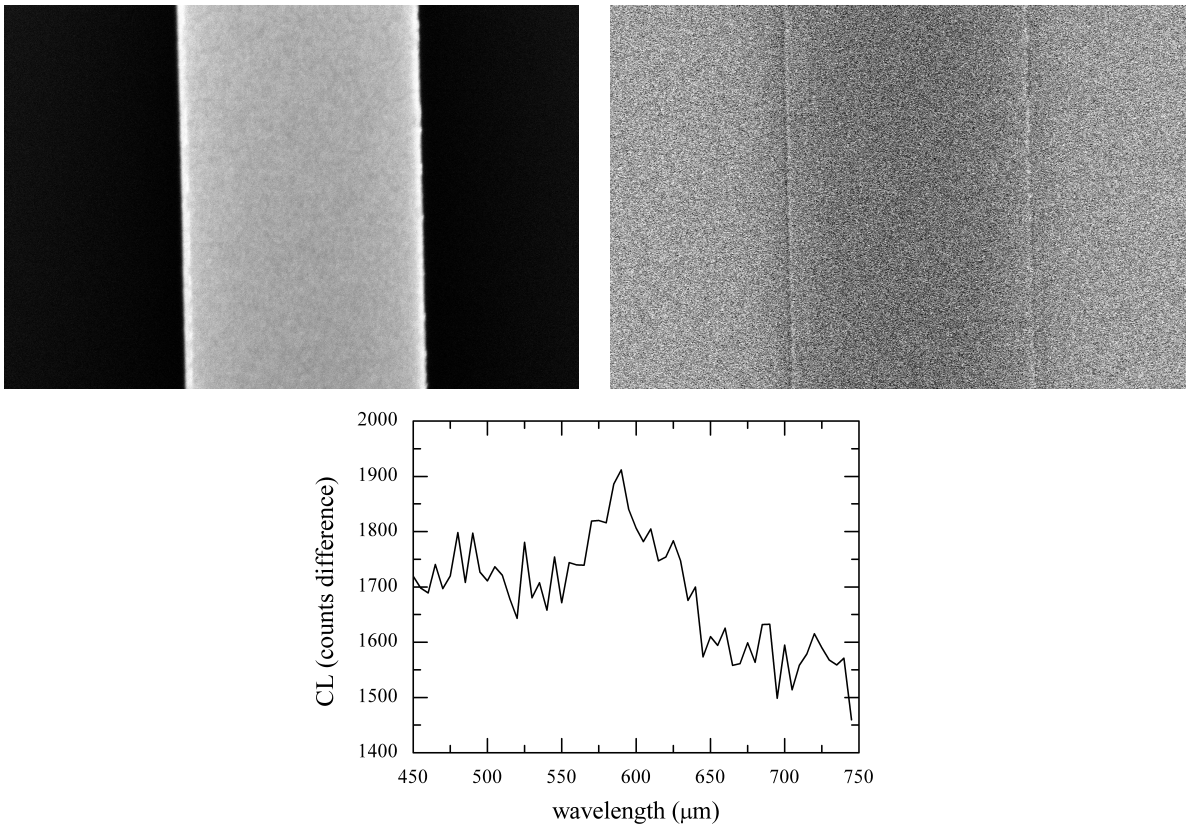

Figure 3.33: CL image excited by the electron beam of the energy of 30 kV, and current of 36 nA. The SEM and CL (panchromatic mode) images of the layer strip are shown above on left and right, respectively. The CL spectrum taken in the monochromatic mode from the layer-edge is shown below.

Consequently, SEM and CL images of the array of plasmonic antennas are shown in Fig 3.34. The CL image shows four circle-like features (bottom right) caused by the contamination of the specimen during CL measurement with big electron beam current. The contamination of the specimen represents the reason for only a short duration of collection (a few minutes) of CL signal excited by beam currents above 40 nA.

Then, the CL was measured on cylindrical antennas of different diameters. The SEM and CL (panchromatic mode) images of antennas are shown in Fig. 3.35. The CL spectra acquired from the edge of antennas (acquired in mono-chromatic mode) of diameter of 55 nm, 60 nm, 80 nm are depicted in Fig. 3.36. The peak positions are red-shifted with the increasing antenna diameter.

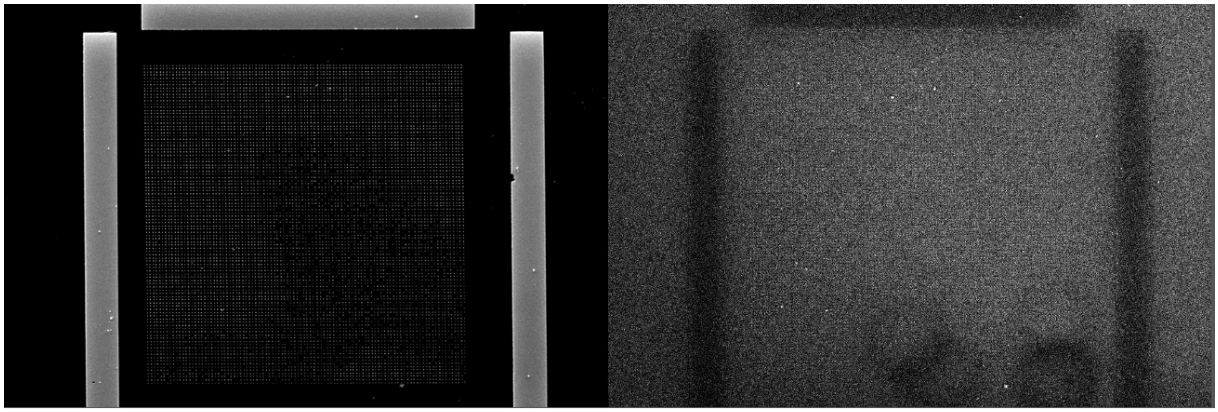

Figure 3.34: The antenna array depicted by SEM (left) and CL (right) signals. The horizontal field of view is 100 μm.

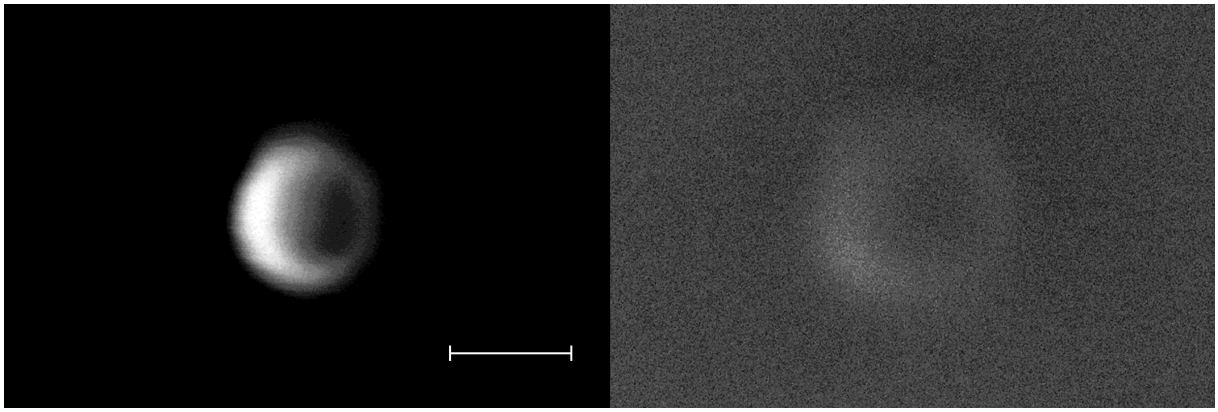

Figure 3.35: The comparison of the ETD signal of secondary electrons and cathodoluminescence signal acquired from MonoCL4 apparatus. The bar denotes 100 nm.

3.5.3 Conclusions

Concluding, the cathodoluminescence spectra of plasmonic structures (in visible range) were measured. CL spectrum of the (Au) layer edge possessed the peak at about 600 nm. The CL spectra of cylindrical Au antennas show resonance wavelength shift with respect to an antenna diameter (55 nm, 60 nm, 80 nm).

This Chapter was motivated by an effort to demonstrate the capability to perform the cathodoluminescence measurements. The intention was to compare CL spectra with EELS ones and thus to show the difference between radiated and non-radiated modes by both techniques. Nevertheless, the CL signal was too small and the contamination during the signal acquisition was very fast.

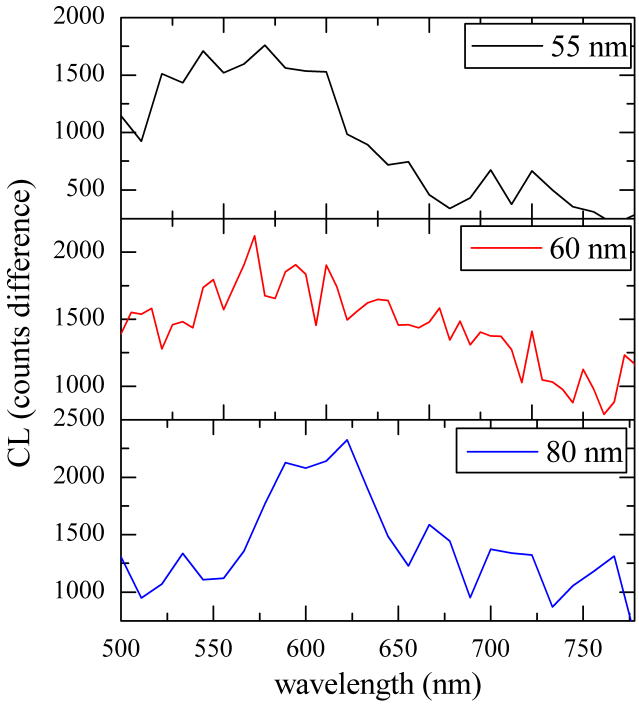

Figure 3.36: CL spectra acquired from circular antennas (see Fig. 3.35) of different diameters (in legend). The spectra are taken from positions/impinged points in close vicinity ($\sim$ 5 nm) of the antenna.

4. Conclusions

The presented work deals with the infrared and visible plasmonic antennas for absorption- (Section 3.3) and sensing-related applications (Section 3.4). It involves both experimental and theoretical study of plasmonic antennas; the antennas were fabricated, their optical properties were measured and modelled by electromagnetic field simulations [68].

The fabrication of plasmonic antennas by the Electron Beam Lithography (EBL) and the Focused Ion Beam are described in Section 3.1. Moreover, to prove the applicant is able to use these techniques, this Section includes images of fabricated structures. In particular, EBL method shows its efficiency to fabricate not only $\sim \mu$m double antennas with the gap reaching 20 nm but also optical dimmers with arm length of about 60 nm. In contrast, the Focused Ion Beam (FIB) was used for fabrication of optical antennas with high precision of geometry (circles, rectangles, triangles, crescents) and their positioning in small distances (of $\sim$ 15 nm) between each other. These structures were consequently used for measurements of the cathodoluminescence (reported in Section 3.5.2) and the Electron Energy Loss Spectroscopy (EELS).

Plasmonic infrared antennas deposited on the SRON layer with a significant absorption in the mid-infrared were studied both for their resonant and absorption properties in Section 3.3 based on author's publications [62], [63]. Almost each reflection spectrum of specific antenna arm length possesses two resonant plasmonic peaks being separated by a dip resulting from a strong coupling of plasmonic oscillations with material absorption resonances in SRON. Consequently, this coupling results in a non-linear scaling between the resonance wavelength and the antenna arm length. Subsequently, the relation between the electric field intensity enhanced by the antenna resonance and the absorption in the SRON layer below antenna were found for different antenna arm lengths. The increased absorption in SRON below the antenna requires both substantial plasmonic resonances and high material absorption of SRON at the same wavelength. The absorption efficiency related to a reference SRON layer reaches its maximal values of 13 at $\lambda = 8.6$ μm ($L = 3.2$ μm), and of 19 at $\lambda = 20$ μm ($L = 4.4$ μm) for lower and upper branches, respectively.

In Section 3.4, the ability of a plasmonic antenna resonance to enhance a given vibrational mode of its substrate (called SEIRS) was studied and confirmed for SRON possessing 3-4 material resonances. It was shown, that the coupling between the plasmonic resonance and the material oscillations results in not only splitting of the plasmonic-antenna resonance (due to the increased absorption of the surrounding material) but also a remarkable excitation of surface phonon polaritons. Moreover, it was found (in Section 3.4.1) that despite the material possesses more material resonances (described by overlapping Lorentz oscillators), it is possible to find the antenna arm length enhancing the vibrational mode of a given material resonance.

The measured cathodoluminescence spectra of antennas (in visible) were presented in Section 3.5 to show different type of antenna excitation. In particular, CL spectra of cylindrical Au antennas show resonance wavelength shift with respect to an antenna size (55 nm, 60 nm, 80 nm).

So far, the work was focused mainly on resonances of plasmonic antennas on the substrate (SRON) possessing vibrational modes (material resonances) and thus having pronounced dispersion of its refractive index. It has been shown, that the antenna resonance is able to enhance both the absorption in the substrate (with possible temperature increase) and vibrational modes (demanded in sensing applications) in the near- and far-field, respectively. Furthermore, it has been found that despite the presence of more material resonances (described by overlapping Lorentz oscillators), it is still possible to find the antenna arm length enhancing the vibrational mode of a given material resonance. This behaviour is promising in sensing-related applications such as SEIRS. It represents a potential challenge for further study because there are publications aimed at materials with the only one material resonance.

Acknowledgement
Práce vznikla za podpory projektu CEITEC (CZ.1.05/1.1.00/02.006) a projektu AMISPEC (TAČR TE01020233).

Bibliography

[1] Zenneck J.: Über die fortpflanzung ebener elektromagnetischer wellen längs einer ebenen leiterfläche und ihre beziehung zur drahtlosen telegraphie, *Ann. d. Phys.* **23**, p. 846-866, 1907.

[2] Sommerfeld A.: Jahrbuch d. drahtl. Telegraphie, *Ann. Physik* **28**, p. 665, 1909.

[3] Economou E. N.: Surface Plasmons in Thin Films. *Physical Review* **182** (2), p. 539-554, 1969. DOI: 10.1103/PhysRev.182.539.

[4] Zayats A. V., Smolyaninov I. I., Maradudin A. A.: Nano-optics of surface plasmon polaritons. *Physics Reports* **408** (3-4), p. 131–314, 2005. DOI: 10.1016/j.physrep.2004.11.001.

[5] Raether H.: Surface Plasmons on Smooth and Rough Surfaces and on Gratings. *Springer Tracts in Modern Physics* **111**, p. 1-133. Springer-Verlag, New York 1988. ISBN 0-387-17363-3.

[6] Berini P.: Plasmon–polariton modes guided by a metal film of finite width. *Optics Letters* **24** (15), p. 1011-1013, 1999. DOI: 10.1364/OL.24.001011.

[7] Maier S. A.: *Plasmonics: Fundamental and Applications*. Springer, Bath-UK, 2007. ISBN-10: 0387331506.

[8] Wood R. W.: On a remarkable case of uneven distribution of light in a diffraction grating spectrum. *Phil. Mag.* **4**, p. 396-402, 1902.

[9] Powell C. J., Swan J. B.: Origin of the Characteristic Electron Energy Losses in Aluminum. *Phys. Rev.* **115**, p. 869-875, 1959.

[10] Ritchie, R. H.: Plasma losses by fast electrons in thin films. *Physical Review* **106** (5), p. 874–881, 1957. DOI: 10.1103/PhysRev.106.874.

[11] Kretschmann E., Reather H.: Radiative decay of non radiative plasmons excited by light. *Zeitschrift für Naturforschung* **23A**, p. 2135-2136, 1968.

[12] Otto A.: Excitation of nonradiative surface plasma waves in silver by the method of frustrated total reflection. *Zeitschrift für Physik* **216**, p. 398-410, 1968.

[13] Zia R., Schuller J. A., Chandran A., Brongersma M. L.: Plasmonics: the next chip-scale technology. *Materials Today* **9** (7-8), 2006. DOI: 10.1016/S1369-7021(06)71572-3

[14] Stockman M. I.: Nanoplasmonics: The physics behind the applications. *Physics Today* **64** (2), p. 39-44, 2011. doi.org/10.1063/1.3554315

[15] Krenn J.: Perspective on plasmonics. *Nature Photonics* **6**, p. 714–715, 2012. doi:10.1038/nphoton.2012.275

[16] Dionne J. A., Diest K., Sweatlock L. A., Atwater H. A.: PlasMOStor: A Metal-Oxide-Si Field Effect Plasmonic Modulator. *Nano Letters* **9** (2), p. 897–902, 2009. DOI: 10.1021/nl803868k

[17] Stockman M. I.: An easier route to high harmony. *Nature* **453**, 2008.

[18] Neutens P., Van Dorpe P., De Vlaminck I., Lagae L., Borghs G.: Electrical detection of connected gap plasmons in metal–insulator–metal waveguides. *Nature Photonics* **3**, p.283, 2009.

[19] Dionne J. A., Diest K., Sweatlock L. A., Atwater H. A.: *NanoLetters* **9**, p. 897, 2009.

[20] Lal S., Link S., Halas N. J.: Nano-optics from sensing to waveguiding. *Nature Nanophotonics* **1**, p. 641-648, 2007. doi:10.1038/nphoton.2007.223

[21] Homola J., Yeea S. S., Gauglitzb G.: Surface plasmon resonance sensors: review. *Sensors and Actuators B: Chemical* **54** (1-2), p. 3-15, 1999. DOI: 10.1016/S0925-4005(98)00321-9.

[22] Lal S., Clare S. E., Halas N. J.: Nanoshell-Enabled Photothermal Cancer Therapy: Impending Clinical Impact. *Acc. Chem. Res.* **41** 12, p. 1842-1851, 2008. DOI: 10.1021/ar800150g

[23] Bharadwaj P., Deutsch B., Novotny L.: Optical antennas. *Advances in Optics and Photonics* **1**, p. 438–483, 2009. DOI:10.1364/AOP.1.000438.

[24] Biagioni P., Huang J.-S., Hecht B.: Nanoantennas for visible and infrared radiation. *Report Progress Physics* **75** (2), 024402, 2012. DOI: 10.1088/0034-4885/75/2/024402.

[25] Novotny L., van Hulst N.: Antennas for light. *Nature Photonics* **5** (2), p. 83-90, 2011. DOI: 10.1038/NPHOTON.2010.237.

[26] Novotny L.: From near-field optics to optical antennas. *Physics Today* **64** (7), p. 47-52, 2011.

[27] Berkovitch N., Ginzburg P., Orenstein M.: Nano-plasmonic antennas in the near infrared regime. *Journal of Physics: Condensed Matter* **24** (7), 073202, 2012.

[28] Mayer K. M., Hafner J. H.: Localized Surface Plasmon Resonance Sensors. *Chemical Reviews ACS* **111**, p. 3828–3857, 2011.

[29] Taubner T., Keilmann F., Hillenbrand R.: Nanoscale-resolved subsurface imaging by scattering-type near-field optical microscopy. *Optics Express* **13** (22), 2005.

[30] Grober R. D., Schoelkopf R. J., Prober D. E.: Optical antenna: Towards a unity efficiency near-field optical probe. *Applied Physics Letters* **70** (11), p. 1354-1356, 1997. DOI: 10.1063/1.118577.

[31] Stockle R. M., Suh Y. D., Deckert V., Zenobi R.: Nanoscale chemical analysis by tip-enhanced Raman spectroscop. *Chemical Physics Letters* **318**, p. 131–136, 2000.

[32] Atwater H. A., Polman A.: Plasmonics for improved photovoltaic devices. *Nature Materials* **9**, p. 205-213, 2010. doi: 10.1038/nmat2629

[33] Ferry V. E., Munday J. N., Atwater H. A.: Design Considerations for Plasmonic Photovoltaics. *Advanced Materials* **22**, p. 4794-4808, 2010. DOI: 10.1002/adma.201000488

[34] Pillai S., Catchpole K. R., Trupke T., Green M. A.: Surface plasmon enhanced silicon solar cells. *Journal of Applied Physics* **101**, 093105, 2007.

[35] Biteen J. S., Sweatlock L. A., Mertens H., Lewis N. S., Polman A., Atwater H. A.: Plasmon-Enhanced Photoluminescence of Silicon Quantum Dots: Simulation and Experiment. *Journal of Physical Chemistry C* **111** (36), 13372-13377, 2007.

[36] Mertens H., Koenderink A. F., Polman A.: Plasmon-enhanced luminescence near noble-metal nanospheres: Comparison of exact theory and an improved Gersten and Nitzan model. *Physical Review B* **76**, 115123, 2007.

[37] Novotny, L., Bian, R. X., Xie, X. S.: Theory of nanometric optical tweezers. *Phys. Rev. Lett.* **79**, p. 645–648, 1997.

[38] Righini, M., Zelenina, A. S., Girard, C., Quidant R.: Parallel and selective trapping in a patterned plasmonic landscape. *Nature Phys.* **3**, p. 477–480, 2007.

[39] Righini, M., Volpe, G., Girard, C., Petrov, D., Quidant, R.: Surface plasmon optical tweezers: tunable optical manipulation in the femtonewton range. *Physical Review Letters* **100**, 183604, 2008.

[40] Baffou G., Quidant R., Girard C.: Heat generation in plasmonic nanostructures: Influence of morphology. *Applied Physics Letters* **94** (15), 153109, 2009. DOI: 10.1063/1.3116645.

[41] Baffou G., Quidant R., Girard Ch.: Thermoplasmonics modeling: A Green's function approach. *Physical Review B* **82** (16), 165424, 2010. DOI: 10.1103/PhysRevB.82.165424.

[42] Baffou G., Kreuzer M. P., Kulzer F., Quidant R.: Temperature mapping near plasmonic nanostructures using fluorescence polarization anisotropy. *Optics Express* **17** (5), 2009.

[43] Huang X., Qian W., El-Sayed I. H., El-Sayed M. A.: The potencial use of the enhanced nonlinear properties of gold nanosphere in photothermal cancer therapy. *Lasers Surg. Med.* **39** (9), 747-753, 2007.

[44] Maxwell, J. C.: *A Treatise on Electricity and Magnetism. Clarendon Press Series*, Macmillan, London, **1-3**, 1873.

[45] Maxwell, J. C.: *A Dynamical Theory of the Electromagnetic Field*. Phil. Trans. R. Soc. Lond. **155**, p. 459-512, 1865.

[46] Hertz H.: *Untersuchungen über die Ausbreitung der elektrischen Kraft*, J. A. Barth, Leipzig, 1894.

[47] Stratton J. A.: *Electromagnetic Theory*, McGraw - Hill Book Company, New York a London, 1941.

[48] Griffiths D. J.: *Introduction to Electrodynamics*, Prentice Hall, New Jersey, 1999.

[49] Born M., Wolf E.: *Principles of Optics*. Pergamon Press Ltd. Hill Hall, Oxford-England, 1980. ISBN 0-08-026482-4.

[50] Johnson P. B., Christy R. W. *Phys. Rev. B* **6**, 4370, 1972.

[51] Barnes V. L.: Surface plasmon–polariton length scales: a route to sub-wavelength optics. *Journal of Optics A* **8** (4), 2006. doi:10.1088/1464-4258/8/4/S06

[52] Stegeman G. I., Maradudin A. A., Shen T. P., Wallis R. F.: Refraction of surface polaritons by a semi-infinite film on a metal. *Physical Review B* **29**, 12, 1984.

[53] Barnes W. L., Dereux A., Ebbesen T. W.: Surface plasmon subwavelength optics. *Nature* **424** (6950), p. 824 - 830, 2003. DOI: 10.1038/nature01937.

[54] Zia R.; Brongersma M. L.: Surface plasmon polariton analogue to Young's double-slit experiment. *Nature Nanotechnology* **2**, p. 426-429, 2007.

[55] Gan Q., Gao Y., Bartoli F. J.: Vertical Plasmonic Mach-Zehnder Interferometer for ultra-sensitive optical sensing. *Optics Express* **17**, 20747-20755, 2009.

[56] Temnov V. V., Armelles G., Woggon U., Guzatov D., Cebollada A., Garcia-Martin A., Garcia-Martin J.-M., Thomay T., Leitenstorfer A., Bratschitsch R.: Active magneto-plasmonics in hybrid metal–ferromagnet structures. *Nature Photonics* **4**, p. 107-111, 2010.

[57] Škoda D., Kalousek R., Tomanec O., Bartošík M., Břínek L., Šustr L., Šikola T.: Studium optických vlastností nanostruktur pomocí mikroskopie blízkého pole. *Jemná mechanika a optika*, **54** (7-8), p. 219-222, 2009. ISSN: 0447- 6441.

[58] Břínek L., Dvořák P., Neuman T., Dub P., Kalousek R., Šikola T.: Aplikace rastrovací optické mikroskopie v blízkém poli pro plasmoniku. *Jemná mechanika a optika*, **58** (6), p. 169-171, 2013, ISSN: 0447- 6441.

[59] Dvořák P., Neuman T., Břínek L., Šamořil T., Kalousek R., Dub P., Varga P., Šikola T.: Control and Near-Field Detection of Surface Plasmon Interference Patterns. *NanoLetters* **13**, 2558-2563, 2013.

[60] Břínek L., Édes, Z., Dvořák P., Neuman T., Šamořil T., Kalousek R., Dub P., Šikola T.: Interference povrchových plazmonů v blízkém poli. *Československý časopis pro fyziku*, **63** (4), p. 234-236, 2013. ISSN: 0009- 0700.

[61] Crozier K. B., Sundaramurthy A., Kino G. S., and Quate C. F.: Optical antennas: Resonators for local field enhancement. *Journal of Applied Physics* **94** (7), p. 4632-4642, 2003. DOI: 10.1063/1.1602956.

[62] Šikola T., Kekatpure R. D., Barnard E. S., White J. S., Dorpe P. Van, Břínek L., Tomanec O., Zlámal J., Lei D., Sonnefraud Y., Maier S. A., Humlíček J., Brongersma M. L.: Mid - IR plasmonic antennas on silicon-rich oxinitride absorbing substrates: nonlinear scaling of resonance wavelengths with antenna length. *Applied Physics Letters* **95** (25), 253109, 2009. doi:10.1063/1.3278593

[63] Břínek L., Šamořil T., Tomanec O., Hrton M., Kalousek R., Spousta J., Dub P., Varga P., Šikola T.: Plasmon Resonances of Mid-IR Antennas on an Absorbing Substrate: Optimization of Localized Absorption Enhancement. To be submitted, 2015.

[64] Mie G. *Annalen der Physik* **25** (4), p. 377, 1908.

[65] Bohren C. F., Huffman D.R.: *Absorbtion and Scattering of Light by Small Particles.* Wiley-VCH Verlag GmbH Co. KGaA, Weinheim-Germany, 2004. ISBN-13: 978-0-471-29340-8.

[66] Novotny L.: Effective Wavelength Scaling for Optical Antennas. *Physical Review Letters* **98** (26), 266802, 2007. DOI: 10.1103/PhysRevLett.98.266802.

[67] Barnard E. S., White J. S., Chandran A., Brongersma M. L.: Spectral properties of plasmonic resonator antennas. *Optics Express* **16** (21), 16529, 2008.

[68] Kalousek R., Dub P., Břínek L., Šikola T.: Response of plasmonic resonant nanorods: an analytical approach to optical antennas. *Optics Express* **20** (16), p.17916-17927, 2012.

[69] Gonzalez A. L., Noguez C., Beranek J., Barnard A. S.: Size, Shape, Stability, and Color of Plasmonic Silver Nanoparticles. J. *Physical Chemistry C* **118**, 9128-9136, 2014.

[70] Aubry A., Lei D. Y., Fernández-Domínguez A. I., Sonnefraud Y., Maier S. A., Pendry J. B.: Plasmonic Light-Hartvesting Devices over the Whole Visible Spectrum. *Nano Letters* **10** (7), p. 2574-2579, 2010. DOI: 10.1021/nl101235d.

[71] Fernández-Domínguez A. I., Maier S. A., Pendry J. B.: Collection and Concentration of Light by Touching Spheres: A Transformation Optics Approach. *Physical Review Letters* **105** (26), 266807, 2010. DOI: 10.1103/PhysRevLett.105.266807.

[72] Palik E. D.: *Handbook of Optical Constants of Solids.* Academic Press inc. (London) Ltd., London, 1985.

[73] Maradudin A. A., Wallis R. F., Stegeman G. I.: The Optics of Surface and Guided Waves Polaritons. *Progress in Surface Science* **33**, p. 171-258, 1990.

[74] Sanchez-Gil J. A., Maradudin A. A.: Dynamic near-field calculations of surface-plasmon polariton pulses resonantly scattered at sub-micron metal defects. *Optics Express* **12** (5), p. 833-894, 2004.

[75] Barnard E. S., White J. S., Chandran A., Brongersma M. L.: Spectral properties of plasmonic resonator antennas. *Optics Express* **16** (21), 16529, 2008.

[76] Taflove A., Hagness S. C.: *Computational Electrodynamics: The Finite-Difference Time-Domain Method*, 2nd ed. Artech House, Inc., Boston and London, 2000.

[77] Ward D. W., Nelson K. A.: *Finite-Difference Time-Domain (FDTD) Simulations of Electromagnetic Wave Propagation Using a Spreadsheet*. Wiley Periodicals, Inc. Comput Appl. Eng. Educ. **13**, p. 213-221, 2005.

[78] Taflove A.: *Application of the finite-difference time-domain method to sinusoidal steady state electromagnetic penetration problems*. IEEE Transactions on Electromagnetic Compatibility **22** (3), p. 191–202, 1980. DOI: 10.1109/TEMC.1980.303879.

[79] Yee K. S.: Numerical solution of initial boundary value problems involving Maxwell's equations in isotropic media. *IEEE Trans. Antennas Propagat.* **14** (3), p. 302-307, 1966.

[80] Schneider J. B.: Understanding the finite-difference time-domain method. *Scholl of electrical engineering and computer science*. Washington State University. 2010. http://www. eecs. wsu. edu/ schneidj/ufdtd/

[81] Dey S., Mittra R.: A locally conformal finite-difference time-domain (FDTD) algorithm for modelling three-dimensional perfectly conducting objects. *IEEE Microw. and Guided Wave Lett.* **7** (9), p. 273-275, 1997.

[82] Hwang K.-P., Cangellaris A. C.: Effective permittivities for second-order accurate FDTD equations at dielectric interfaces. *IEEE Microw. Wireless Components Lett.* **11**, p. 158-160, 2000.

[83] Mohammadi A., Nadgaran H., Agio M.: Contour-path effective permittivities for the two-dimensional finite-difference time-domain method. *Optics Express* **13**, p. 10367-10381, 2005.

[84] Makinen R. M., Juntunen J. S., Kivikovski M. A.: An improved thin-wire model for FDTD. *IEEE Trans. Microw. Theory Tech.* **50**, p. 1245-1255, 2002.

[85] Railton C. J., Boon P. K., Craddock I. J.: The treatment of thin wires in the FDTD method using a weighted residuals approach. *IEEE Trans. Antennas Propagat.* **52** (11), p. 2941-2949, 2004.

[86] Schneider J. B., Abdijalilov K.: Analytic Field Propagation TFSF Boundary for FDTD Problems Involving Planar Interfaces: PECs, TE, and TM. *IEEE Transactions on Antennas and Propagation* **54**, 9, 2006.

[87] F. D. T. D. Solutions (version 7.5.5), from Lumerical Solutions, Inc., http://www.lumerical.com.

[88] Muhlschlegel P., Eisler H.-J., Martin O. J. F., Hecht B.: Resonant Optical Antennas. *Science* **308**, 2005.

[89] Sládková L., Képeš E.; Břínek L., Prochazka D., Novotný J., Kaiser J.: Detekcia stopových prvkov metódou spektroskopie laserom indukovanej mikroplazmy (LIBS) pomocou aplikácie nanočastíc. *Jemná mechanika a optika*, **59** (6-7), p. 201-203, 2014. ISSN: 0447- 6441.

[90] Gonzalez F. J., Boreman G.D.: Comparison of dipole, bowtie, spiral and log-periodic IR antennas. *Infrared Physics Technology* **46** (5), p. 418-428, 2005. DOI: 10.1016/j.infrared.2004.09.002.

[91] Govorov A. O., Richardson H. H.: Generating heat with metal nanoparticles. *Nanotoday* **2** (1), p. 30-38, 2007. DOI: 10.1016/S1748-0132(07)70017-8.

[92] Baffou G., Girard Ch., Quidant R.: Mapping Heat Origin in Plasmonic Structures. *Physical Review Letters* **104**, 136805, 2010.

[93] Schmuttenmaer Ch. A.: Exploring Dynamics in the Far-Infrared with Terahertz Spectroscopy. *Chem. Rev.* **104**, 1759-1779, 2004.

[94] Richards P. L.: Bolometers for infrared and millimeter waves. *J. App. Phys.* **76** (1), 1994.

[95] Gonzalez F. J., Ashley C. S., Clem P. G., Boreman G.D.: Antenna-coupled microbolometer arrays with aerogel thermal isolation. *Infrared Physics & Technology* **45**, 47–51, 2004.

[96] Krenz P., Alda J., Boreman G.: Orthogonal infrared dipole antenna. *Infrared Physics & Technology* **51**, p. 340-343, 2008.

[97] Cao L., Barsic D. N., Guichard A. R., Brongersma M. L.: Plasmon-Assisted Local Temperature Control to Pattern Individual Semiconductor Nanowires and Carbon Nanotubes. *NanoLetters* **7** (11), 3523-3527, 2007.

[98] Richardson H. H., Hickman Z. N., Govorov A. O., Thomas A. C., Zhang W., Kordesch M. E.: Thermooptical Properties of Gold Nanoparticles Embedded in Ice: Characterization of Heat Generation and Melting. *NanoLetters* **6** (4), 783-788, 2006.

[99] Le F., Brandl D. W., Urzhumov,Y. A., Wang H., Kundu J., Halas N. J., Aizpurua J., Nordlander P.: Metallic Nanoparticle Arrays: A Common Substrate for Both Surface-Enhanced Raman Scattering and Surface-Enhanced Infrared Absorption. *ACS Nano* **2** (4), p. 707–718, 2008.

[100] Kneipp K., Wang Y., Kneipp H., Perelman L. T., Itzkan I., Dasari R. R., Feld M. S.: Single Molecule Detection Using Surface-Enhanced Raman Scattering (SERS). *Physical Review Letters* **78** (9), p. 1667-1670, 1997.

[101] Nie S., Emory S. R.: Probing Single Molecules and Single Nanoparticles by Surface-Enhanced Raman Scattering. *Science* **275**, 1997.

[102] Novotny L., Hecht B.: *Principles of Nano-Optics.* Cambridge University Press. ISBN 9780521539883, 2006.

[103] Li J. F., Huang Y. F., Ding Y., Yang Z. L., Li S. B., Zhou X. S., Fan F. R., Zhang W., Zhou Z. Y., Wu D. Y., Ren B., Wang Z. L., Tian Z. Q.: Shell-isolated nanoparticle-enhanced Raman spectroscopy. *Nature* **464**, p. 392-395, 2010. DOI:10.1038/nature08907

[104] Lombardi J. R., Birke R. L.: A Unified Approach to Surface-Enhanced Raman Spectroscopy. *J. Phys. Chem. C* **112** (14), p. 5605-5617, 2008.

[105] Xu H., Aizpurua J., Kall M., Apell P.: Electromagnetic contributions to single-molecule sensitivity in surface-enhanced Raman scattering. *Physical Review E* **62** (3), 2000.

[106] Pettinger B., Ren B., Picardi G., Schuster R., Ertl G.: Nanoscale Probing of Adsorbed Species by Tip-Enhanced Raman Spectroscopy. *Physical Review Letters* **92** (9), 2004.

[107] Cancado L. G., Hartschuh A., Novotny L.: Tip-enhanced Raman spectroscopy of carbon nanotubes. *J. Raman Spectrosc.* **40**, p. 1420–1426, 2009.

[108] Adato R., Altug H.: In-situ ultra-sensitive infrared absorption spectroscopy of biomolecule interactions in real time with plasmonic nanoantennas. *Nature Communications* **4**, p. 2154, 2013. DOI: 10.1038/ncomms3154

[109] Hillenbrand R., Taubner T., Keilmann F.: Phonon-enhanced light–matter interaction at the nanometre scale. Nature **418**, p. 159-162, 2002.

[110] Neubrech F., Pucci A., Cornelius T.W., Karim S., García-Etxarri A., Aizpurua J.: Resonant Plasmonic and Vibrational Coupling in a Tailored Nanoantenna for Infrared Detection. *Physical Review Letters* **101**, 157403, 2008.

[111] Neubrech F., Weber D., Enders D., Nagao T., Pucci A.: Antenna Sensing of Surface Phonon Polaritons. *J. Phys. Chem. C*, **114**, p. 7299–7301, 2010.

[112] Neubrech F., Pucci A.: Plasmonic Enhancement of Vibrational Excitations in the Infrared. *IEEE Journal of selected topics in quantum electronics* **19**, 3, 2013.

[113] Gigler A. M., Huber A. J., Bauer M., Ziegler A., Hillenbrand R., Stark R. W.: Nanoscale residual stress-field mapping around nanoindents in SiC by IR s-SNOM and confocal Raman microscopy. *Optics Express* **17** (25), 2009.

[114] Brehm M., Taubner T., Hillenbrand R., Keilmann F.: Infrared Spectroscopic Mapping of Single Nanoparticles and Viruses at Nanoscale Resolution. *NanoLetters* **6** (7), 2006.

[115] Schnell M., García-Etxarri A., Huber A. J., Crozier K., Aizpurua J., Hillenbrand R.: Controlling the near-field oscillations of loaded plasmonic nanoantennas. *Nature Photonics* **3**, p. 287-291, 2009. doi:10.1038/nphoton.2009.46

[116] Huang J.-S., Kern J., Geisler P., Weinmann P., Kamp M., Forchel A., Biagioni P., Hecht B.: Mode Imaging and Selection in Strongly Coupled Nanoantennas. *NanoLetters* **10** (6), p. 2105–2110, 2010.

[117] Prodan E., Radloff C., Halas N. J., Nordlander P.: A Hybridization Model for the Plasmon Response of Complex Nanostructures. *Science* **302** (5644), p. 419-422, 2003. DOI: 10.1126/science.1089171

[118] Bryant G. W., de Abajo F. J. G., Aizpurua J.: Mapping the Plasmon Resonances of Metallic Nanoantennas. *NanoLetters* **8** (2), p. 631–636, 2008. DOI: 10.1021/nl073042v

[119] Ai Leen Koh, Bao K., Khan I., Smith W. E., Kothleitner G., Nordlander P., Maier S. A., and McComb D. W.: Electron Energy-Loss Spectroscopy (EELS) of Surface Plasmons in Single Silver Nanoparticles and Dimers: Influence of Beam Damage and Mapping of Dark Modes. *ACS Nano* **3** (10), p. 3015–3022, 2009. DOI: 10.1021/nn900922z.

[120] Spinelli P., van Lare C., Verhagen E., Polman A.: Controlling Fano lineshapes in plasmon-mediated light coupling into a substrate. *Optics Express* **19**, S3, 2011.

[121] Verellen N., Sonnefraud Y., Sobhani H., Hao F., Moshchalkov V. V., Van Dorpe P., Nordlander P., Maier S. A.: Fano Resonances in Individual Coherent Plasmonic Nanocavities. *NanoLetters* **9** (4), p. 1663-1667, 2009. DOI: 10.1021/nl9001876.

[122] Giannini V., Fernandéz-Domínigues A. I., Sonnefraud I., Roschuk T., Fernández-García R., Maier S. A.: Controlling Light Localization and Light-Matter Interactions with Nanoplasmonics. *Small* **6** (22), p. 2498-2507, 2010. DOI: 10.1002/smll.201001044.

[123] Weber D.: *Nanogaps for Nanoantenna-Assisted Infrared Spectroscopy.* Dissertation, Ruperto-Carola-University of Heidelberg, Germany, 2011.

[124] Tomanec O., Hrnčíř T., Lovicar L., Šustr L., Břínek L., Kalousek R., Chmelík R., Spousta J., Šikola T.: Studium vlastností mikro- a nanostruktur v oblasti plazmoniky na Ústavu fyzikálního inženýrství FSI VUT v Brně. *Jemná mechanika a optika*, **52** (6), p. 187-189, 2008. ISSN: 0447- 6441.

[125] http://web.princeton.edu/sites/ehs/labsafetymanual/cheminfo/piranha.htm

[126] Wenchuang Hu: *Ultrahigh resolution electron beam lithography for molecular electronics*. Dissertation, University of Notre Dame, Indiana, USA.

[127] Dregely D., Neubrech F., Duan H., Vogelgesang R., Giessen H.: Vibrational near-field mapping of planar and buried three-dimensional plasmonic nanostructures. *Nature Communications* **4**, 2237, 2013. doi:10.1038/ncomms3237

[128] Křápek V., Koh A., Břínek L., Hrtoň M., Tomanec O., Kalousek R., Maier S., Šikola T.: Spatially resolved electron energy loss spectroscopy of crescent- shaped plasmonic antennas. *Optics Express* **23** (9), 11855-11867, 2015. ISSN: 1094-4087

[129] Botman A., Mulders J. J. L., Weemaes R., Mentink S.: Purification of platinum and gold structures after electron-beam-induced deposition. *Nanotechnology* **17**, p. 3779–3785, 2006. doi:10.1088/0957-4484/17/15/028

[130] Nelayah J., Kociak M, Stéphan O., de Abajo F. J. G., Tencé M., Henrard L., Taverna D., Pastoriza-Santos I., Liz-Marzán L. M., Colliex Ch.: Mapping surface plasmons on a single metallic nanoparticle. *Nature Physics* **3**, p. 348-353, 2007. doi:10.1038/nphys575

[131] Boudarham G., Feth N., Myroshnychenko V., Linden S., de Abajo J. G., Wegener M., Kociak M.: Spectral Imaging of Individual Split-Ring Resonators. *Physical Review Letters* **105**, 255501, 2010. DOI: 10.1103/PhysRevLett.105.255501

[132] Rahmani M., Yoxall E., Hopkins B., Sonnefraud Y., Kivshar Y., Hong M., Phillips C., Maier S.A., Miroshnichenko A.E.: Plasmonic nanoclusters with rotational symmetry: polarization-invariant far-field response vs changing near-field distribution. *ACS Nano* **7** (12), p. 11138–11146, 2013. DOI: 10.1021/nn404869c

[133] Brown L.V., Zhao Ke, King N., Sobhani H., Nordlander P., Halas N. J.: Surface-Enhanced Infrared Absorption Using Individual Cross Antennas Tailored to Chemical Moieties. *J. Am. Chem. Soc.* **135**, p. 3688-3695, 2013.

[134] Alonso-González P., Albella P., Neubrech F., Huck C., Chen J., Golmar F., Casanova F., Hueso L. E., Pucci A., Aizpurua J., Hillenbrand R.: Experimental Verification of the Spectral Shift between Near- and Far-field Peak Intensities of Plasmonic Infrared Nanoantennas. *Physical Review Letters* **110**, 203902, 2013.

[135] Hägglund C., Kasemo B.: Nanoparticle Plasmonics for 2D-Photovoltaics: Mechanisms, Optimization, and Limits. *Optics Express* **17** (14), p. 11944-11957, 2009.

[136] Codreanu I., Boreman G. D.: Infrared Microstrip Dipole Antennas - FDTD Predictions versus Experiment. *Microwave and Optical Technology Letters* **29** (6), 2001.

[137] Tsu D. V., Lucovsky G., Mantini M. J.: Local atomic structure in thin films of silicon nitride and silicon diimide produced by remote plasma-enhanced chemical-vapor deposition. Physical Review B **33** (10), 1986.

[138] Ribeiro M., Pereyra I., Alayo M.I.: Silicon rich silicon oxynitride films for photoluminescence applications. *Thin Solid Films* **426**, p. 200–204, 2003.

[139] Luna-López J. A., Carrillo-López J., Aceves-Mijares M., Morales-Sánchez A., Falcony C.: FTIR and photoluminescence of annealed silicon rich oxide films. *Superficies y Vacío* **22** (1), p. 11-14, 2009.

[140] Dintinger J., Klein S., Bustos F., Barnes W. L., and Ebbesen T. W.: Strong coupling between surface plasmon-polaritons and organic molecules in subwavelength hole arrays. *Phys. Rev. B* **71**, 035424, 2005.

[141] Adato R. Artar A., Erramilli A., Altug H.: Engineered absorption enhancement and induced transparency in coupled molecular and plasmonic resonator systems. *NanoLetters* **13**, p. 2584-2591, 2013.

[142] Azarova N., Ferguson A. J., van de Lagemaat J., Rengnath E., Park W., Johnson J. C.: Coupling between a Molecular Charge-Transfer Exciton and Surface Plasmons in a Nanostructured Metal Grating. *J. Phys. Chem. Lett.* **4**, p. 2658-2663, 2013.

[143] Kohli S. at all.: Nanocrystal formation in annealed a-SiO0.17 N0.07:H films. *Nanotechnology* **15**, p. 1831–1836, 2004.

[144] Habraken F. H. P. M.: Characterization of LPCVD and PECVD silicon oxinitride. *Applied Surface Science* **30**, p. 186-196, 1987.

[145] Wong C. K. at all.: Fabrication of Optical Waveguide using Silicon Oxynitride Prepared by Thermal Oxidation of Silicon Rich Silicon Nitride. *IEEE, 0-7803-9339-2/05*, 2005.

[146] Hussein M. G., Worhoff K., Sengo G., Driessen A.: Optimization of plasma-enhanced chemical vapor deposition silicon oxynitride layers for integrated optics applications. *Thin Solid Films* **515**, p. 3779-3786, 2007.

[147] Kohli S., Theil J. A., Dippo P. C., Jones K. M., Al-Jassim M. M., Ahrenkiel R. K., Rithner Ch. D., Dorhout P. K.: Nanocrystal formation in annealed a-SiO0.17N0.07:H films. *Nanotechnology* **15**, p. 1831–1836, 2004.

[148] Lee J. H., Jeong Ch. H., Lim J. T., Zavaleyev V. A., Min K. S., Kyung S. J., Yeom G. Y.: Characteristics of SiOxNy Films Deposited by PECVD at Low-Temperature Using BTBAS-NH3-O2. *Journal of the Korean Physical Society* **48** (1), 2006.

[149] Zhu M., Han Y., Wehrspohn R. B., Godet C., Etemadi R., Ballutaud D.: The origin of visible photoluminescence from silicon oxide thin films prepared by dual-plasma chemical vapor deposition. *Journal of Applied Physics* **83** (10), 1998.

[150] Tsu D. V., Lucovsky G., Davidson B. N.: Effects of the nearest neighbors and the alloy matrix on SiH stretching vibrations in the amorphous SiOr:H (0¡r¡2) alloy system. *Phys. Rev. B* **40**, p. 1795, 1989.

[151] Tewary A., Kekatpure R. D., Brongersma M. L.: Controlling defect and Si nanoparticle luminescence from silicon oxynitride films with CO2 laser annealing. *Applied Physics Letters* **88**, 093114, 2006.

[152] Pavesi L., Dal Negro L., Mazzoleni C., Franz G., Priolo F.: Optical gain in silicon nanocrystals. *Nature* **408** (6811), 440–444, 2000.

[153] Zewen Lin, Rui Huang, Yanqing Guo, Chao Song, Zhenxu Lin, Yi Zhang, Xiang Wang, Jie Song, Hongliang Li, Xintang Huang: Near-infrared light emission from Si-rich oxynitride nanostructures. *Optical Materials Express* **4** (4), 2014. DOI:10.1364/OME.4.000816

[154] Raether, H.: Excitation of Plasmons and Interband Transitions by Electrons. *Springer Tracks in Modern Physics* **88**, Springer-Verlag, Berlin, 1980.

[155] Hao F., Sonnefraud Y., Van Dorpe P., Maier S. A., Halas N. J., Nordlander P.: Symmetry Breaking in Plasmonic Nanocavities: Subradiant LSPR Sensing and a Tunable Fano Resonance. *NanoLetters* **8** (11), 2008.

[156] Navarro-Cia M., Maier S. A.: Broad-Band Near-Infrared Plasmonic Nanoantennas for Higher Harmonic Generation. *ACS Nano* **6** (4), p. 3537–3544, 2012.

[157] Abajo F. J. G. de, Kociak M.: Probing the Photonic Local Density of States with Electron Energy Loss Spectroscopy. *Physical Review Letters* **100**, 106804, 2008.

[158] Ai Leen Koh, Fernandez-Domínguez A. I., McComb D. W., Maier S. A., Yang J. K. W.: High-Resolution Mapping of Electron-Beam-Excited Plasmon Modes in Lithographically Defined Gold Nanostructures. *NanoLetters* **11** (3), p. 1323–1330, 2011. DOI: 10.1021/nl104410t.

[159] de Abajo F. J. G.: Optical excitations in electron microscopy. *Reviews of Modern Physics* **82**, 2010. DOI: 10.1103/RevModPhys.82.209

[160] Hohenester U., Ditlbacher H., Krenn J. R.: Electron-Energy-Loss Spectra of Plasmonic Nanoparticles. *Physical Review Letters* **103** (10), 106801, 2009. DOI: 10.1103/PhysRevLett.103.106801.

[161] F. J. G. de Abajo, M. Kociak: Probing the Photonic Local Density of States with Electron Energy Loss Spectroscopy. *Physical Review Letters* **100** (10), 106804, 2008. DOI: 10.1103/PhysRevLett.100.106804.

[162] Schmidt F. P., Ditlbacher H., Hohenester U., Hohenau A., Hofer F., Krenn J. R.: Dark Plasmonic Breathing Modes in Silver Nanodisks. *NanoLetters* **12** (11), p. 5780-5783, 2012. DOI: 10.1021/nl3030938

[163] Myroshnychenko V., Nelayah J., Adamo G., Geuquet N., Rodríguez-Fernandez J., Pastoriza-Santos I., MacDonald K. F., Henrard L., Liz-Marzan L. M., Zheludev N. I., Kociak M., de Abajo F. J. G.: Plasmon Spectroscopy and Imaging of Individual Gold Nanodecahedra: A Combined Optical Microscopy, Cathodoluminescence, and Electron Energy-Loss Spectroscopy Study. *NanoLetters* **12** (8), p. 4172–4180, 2012. DOI: 10.1021/nl301742h

[164] Fermi E.: The Ionization Loss of Energy in Gases and in Condensed Materials. *Physical Review* **57**, p. 485-493, 1940.

[165] Julley J. V.: *Cherenkov Radiation and its Application*. Pergamon, New York, 1958.

[166] Ginzburg V. L., Frank I. M.: Radiation of a uniformly moving electron due to its transition from one medium into another. *J. Phys. USSR* **9**, 353, 1945.

[167] Goldsmith P., Jelley J. V.: Optical transition radiation from protons entering metal surfaces. *Philos. Mag.* **4**, 836, 1959.

[168] Kuttge M., Vesseur E. J. R., Koenderink A. F., Lezec H. J., Atwater H. A., de Abajo F. J. G., Polman A.: Local density of states, spectrum, and far-field interference of surface plasmon polaritons probed by cathodoluminescence. *Physical Review B* **79**, 113405, 2009.

[169] Weeber J.C., Krenn J.R., Dereux A., Lamprecht B., Lacroute Y. Goudonnet J.: Near-field observation of surface plasmon polariton propagation on thin metal stripes. *Phys. Rev. B.* **64**, 45411, 2001.

[170] Chaturvedi P., Hsu K. H., Kumar A., Fung K. H., Mabon J. C., Fang N. X.: Imaging of Plasmonic Modes of Silver Nanoparticles Using High-Resolution Cathodoluminescence Spectroscopy. *ACS Nano* **3** (10), p. 2965-2974, 2009. DOI: 10.1021/nn900571z.

[171] Medina R. G., Yamamoto N., Nakano M., de Abajo F. J. G.: Mapping plasmons in nanoantennas via cathodoluminescence. *New Journal of Physics* **10**, 105009, 2008. DOI: 10.1088/1367-2630/10/10/105009.

[172] Kuttge M.: *Cathodoluminescence plasmon microscopy*, Doctoral Thesis, Utrecht University, 2009.